

DISS. ETH NO. 25728

MATERIALS-BASED DESIGN OF AUTONOMOUS MACHINES  
USING 4D PRINTING

A dissertation submitted to attain the degree of  
DOCTOR OF SCIENCES of ETH ZURICH  
(Dr. sc. ETH Zurich)

presented by

TIAN CHEN

Master of Science, Delft University of Technology  
Bachelor of Applied Science, University of Toronto

born on December 31, 1987  
citizen of Canada

accepted on the recommendation of

Prof. Dr. Kristina Shea, examiner  
Prof. Dr. Chiara Daraio, co-examiner  
Prof. Dr. Paolo Ermanni, co-examiner

2019

Tian Chen: *Materials-based design of autonomous machines using 4D printing*, © 2019

DOI: 10.3929/ethz-b-000315958



## ABSTRACT

---

The concept of “The Material Is the Machine” as proposed by Bhattacharya and James refers to the design of tiny machines where the motors and power supplies are inherently replaced by the self-reconfiguring ability of the functional material. When these materials are used in conjunction with 3D printing in a concept known as 4D printing, there is the potential to extend the aforementioned concept to polymeric machines with significant complexity and tunability on the macro-scale.

4D printing refers to 3D printing of designs that transform over time when exposed to certain stimuli. Thus far, the concept of 4D printing has been applied primarily in shape reconfiguration. Functionalities useful to mechanical engineering systems are less explored. This thesis investigates the design of mechanical systems to achieve autonomous functional transformation using a materials-based approach. In particular, it identifies and addresses the following technical gaps between the current state-of-the-art, e.g. shape reconfigurable systems, and future material-based autonomous machines.

- Current reconfigurable systems are not in static equilibrium after shape transformation. The transformed geometries and load-bearing capacity is difficult to predict.
- In dynamic systems, rudimentary functions such as material-based propulsion has not been addressed.
- Little connection has been made between 4D printing and mechanical design, i.e. material-based analogs do not exist for components such as actuators and power supplies.
- Few computational design methods exist for the algorithmic generation of complex 4D printed systems.
- Design guidelines and proof-of-concept solutions are lacking for 4D printed machines that solve current engineering challenges.

The principle of mechanical bistability is exploited to achieve large stable shape reconfiguration as bistable mechanisms inherently possess two equilibrium states. A 3D printed Shape Memory Polymer (SMP) is characterized and used to provide power for autonomous transformation. By combining the two, autonomous deployment of structures and autonomous propulsion of robots are demonstrated. In these works, the functionalities of mechanical components such as actuators, power sources and controllers are encoded within the constituting materials. The timing and sequence of the transformations are tunable and controlled through material composition and design dimensions.

Moving beyond proof-of-concept demonstrations, scalability and modularity are studied as a necessary step towards tackling complex engineering problems. A computational method is proposed for the inverse problem of designing a flat modular surface that deploys to assume

given target shapes. As a demonstration, two doubly-curved target surfaces are achieved from a single flat 3D printed multi-stable designs. As a credible solution to an existing engineering challenge, a self-deploying solar panel is demonstrated. Fabricated entirely using a 3D printer, the solar panel is able to achieve an area expansion ratio of ten times in under 40 seconds.

The demonstrated principles are not limited to snap-through bistability or shape memory polymers. With advances in material science and fabrication technologies, it is expected that functional materials become more efficient and the printing resolution and speed increases. Similarly, advanced computational methods and deeper understanding of mechanics will enable new types of functional transformation. This is the first work towards a material-based design approach using 4D printing for the next generation of mechanical systems.

## ZUSAMMENFASSUNG

---

Das von Bhattacharya und James vorgeschlagene Konzept von "The Material Is the Machine" bezieht sich auf das Design winziger Maschinen, bei denen Motoren und Stromversorgungen von Natur aus durch die Fähigkeit zur Selbstkonfiguration des konstituierenden Materials ersetzt werden. Wenn diese Materialien in Verbindung mit dem 3D-Druck in einem als 4D-Druck bekannten Konzept verwendet werden, besteht die Möglichkeit, das vorgenannte Konzept auf polymere Maschinen mit erheblicher Komplexität im Makromaßstab auszuweiten.

4D-Drucken bezieht sich auf das 3D-Drucken von Designs, die sich im Laufe der Zeit verändern, wenn sie bestimmten Reizen ausgesetzt sind. Bisher wurde das Konzept des 4D-Drucks vor allem bei der Formkonfiguration angewendet. Funktionen, die für Maschinenbausysteme nützlich sind, werden weniger erforscht. Diese Dissertation untersucht den Entwurf mechanischer Systeme, um mithilfe eines materialbasierten Ansatzes eine autonome funktionelle Transformation zu erreichen. Insbesondere werden die folgenden technischen Lücken zwischen dem gegenwärtigen Stand der Technik, z. rekonfigurierbare Systeme und zukünftige materialbasierte Maschinen.

- Derzeit rekonfigurierbare Systeme befinden sich nach der Formtransformation nicht im statischen Gleichgewicht. Die transformierten Geometrien und die Tragfähigkeit sind schwer vorherzusagen.
- In dynamischen Systemen wurden rudimentäre Funktionen wie der Antrieb auf Materialbasis nicht angesprochen.
- Es wurde kaum Verbindung zwischen 4D-Druck und mechanischem Design hergestellt, d. H. Keine materialbasierten Analoga für Komponenten wie Aktuatoren oder Stromversorgungen.
- Für die algorithmische Erzeugung komplexer 4D-Drucksysteme gibt es nur wenige Berechnungsmethoden.
- Konstruktionsrichtlinien und Proof-of-Concept-Lösungen für gedruckte 4D-Maschinen, die die realen technischen Herausforderungen meistern, fehlen.

Das Prinzip der mechanischen Bistabilität wird genutzt, um eine stabile Rekonfiguration der Form zu erreichen, da bistabile Mechanismen von Natur aus zwei Gleichgewichtszustände besitzen. Ein 3D-gedrucktes Shape Memory Polymer (SMP) wird charakterisiert und verwendet, um Energie für die autonome Transformation bereitzustellen. Durch die Kombination dieser beiden Elemente wird der autonome Einsatz von Strukturen und der autonome Antrieb von Robotern demonstriert. In diesen Werken werden die Funktionalitäten mechanischer Komponenten wie Aktuatoren, Stromquellen und Steuerungen in den konstituierenden Materialien

codiert. Das Timing und die Reihenfolge der Transformationen werden durch Materialzusammensetzung und Abmessungen gesteuert.

Abgesehen von Proof-of-Concept-Demonstrationen werden Skalierbarkeit und Modularität als notwendiger Schritt zur Bewältigung komplexer Engineering-Probleme untersucht. Für das inverse Problem des Entwurfs einer flachen modularen Oberfläche, die sich entfaltet, um vorgegebene Zielformen anzunehmen, wird eine rechnerische Lösung vorgeschlagen. Zur Demonstration werden zwei doppelt gekrümmte Zielflächen aus einem einzigen flachen, 3D-gedruckten, multistabilen Bogen erzielt. Als glaubwürdige Lösung für eine bestehende technische Herausforderung wird ein selbstaufstellendes Solarmodul demonstriert. Das Solarpanel, das vollständig mit einem 3D-Drucker hergestellt wurde, kann in zehn Sekunden ein Flächenausdehnungsverhältnis von zehn Mal erreichen.

Die aufgezeigten Prinzipien sind nicht auf Durchschnapp-Bistabilität oder Formgedächtnispolymere beschränkt. Mit den Fortschritten in der Materialwissenschaft und den Fertigungstechnologien wird erwartet, dass Funktionsmaterialien effizienter werden und die Druckauflösung und -geschwindigkeit zunehmen. In ähnlicher Weise ermöglichen fortschrittliche Computer-Tools und ein tieferes Verständnis der Mechanik neue Arten der funktionalen Transformation. Vielmehr ist dies die erste Arbeit an einem materialbasierten Designansatz für die nächste Generation mechanischer Systeme.

## ACKNOWLEDGEMENTS

---

I would like to express my utmost gratitude to my supervisor Professor Kristina Shea. Back in 2014, I literally knocked on your door inquiring about a doctoral position at the lab. To your everlasting credit, you offered me the job. Ever since, you have given me the freedom to explore while at the same time offering your invaluable experience and knowledge at crucial moments. I have developed a lot as a researcher under your guidance and would hopefully offer the same experience to my students some day.

I would like to thank Osama Bilal and Professor Chiara Daraio for the opportunity to collaborate on the many projects, for hosting me at Caltech and for indulging many half-baked ideas. Both of your drive and optimism serves as a constant inspiration, and your advice and comments have been indispensable. I would also like to thank Professor Paolo Ermanni for his expertise and for examining my thesis.

Propers to my labmates at EDAC for putting up with me all these years. It is always refreshing to work on some of your problems when I am stuck on my own. Hope y'all feel the same, otherwise I have just wasted a whole lot of your time. To the students I have had the pleasure of supervising, more than any research output, it was rewarding to see you learn, develop independent ideas and mature as engineers and researchers.

Personally, I would like to thank Jung, Stefan and Timo for supporting me through difficult times, and for continuing to treat me as a member of your family. I would like to thank the support of my family back home and I apologize for my frequent absences. To Jade, thank you for putting up with my quirks, accommodating my erratic schedule and showing a genuine interest in what I do. You have helped me in more ways than you can imagine.

We are nothing but passing ephemerals in the grand scheme of things. It is incredibly lucky for me to meet and work with all of you, to call you my friends and for you to allow me to leave a mark, however fleeting, in your lives. Soon our trajectories may diverge. Years down the road, I hope that these moments of intersection will be remembered with fondness and laughter.



# CONTENTS

---

<b>1</b>	<b>INTRODUCTION</b>	<b>1</b>
1.1	Summary . . . . .	1
1.2	Background . . . . .	2
1.2.1	4D Printing: 3D Printing of Functional Materials . . . . .	2
1.2.2	Mechanical Instability . . . . .	4
1.2.3	Shape Memory Effect in Polymers . . . . .	6
1.2.4	Soft Autonomous Robotics . . . . .	6
1.2.5	Design of the Next Generation Mechanical Systems . . . . .	7
1.3	Scope and Outline of the Thesis . . . . .	8
<b>2</b>	<b>BISTABLE MECHANISM AND MULTI-STABLE DEPLOYABLE STRUCTURES</b>	<b>11</b>
2.1	Summary . . . . .	11
2.2	Background . . . . .	12
2.3	Method and Design . . . . .	13
2.3.1	Multi-Material Fabrication . . . . .	13
2.3.2	Bistable Unit Element . . . . .	14
2.3.3	Design of Hierarchical Structures . . . . .	17
2.4	Results and Discussion . . . . .	21
2.4.1	Characterization of the Printed Materials . . . . .	21
2.4.2	Mechanical Characterization of the Bistable Mechanism . . . . .	22
2.4.3	Hierarchical Structures . . . . .	24
2.5	Conclusion . . . . .	25
<b>3</b>	<b>SHAPE MEMORY EFFECT AND 3D PRINTING</b>	<b>29</b>
3.1	Summary . . . . .	29
3.2	Background . . . . .	30
3.3	Method and Design . . . . .	32
3.3.1	Materials and Fabrication . . . . .	32
3.3.2	Thermomechanical Characterization . . . . .	33
3.3.3	Linear Viscoelastic Constitutive Theory . . . . .	33
3.3.4	Implementation of Finite-Element Simulation . . . . .	34
3.3.5	Validation of Model Accuracy . . . . .	35
3.3.6	Design of Active Structures . . . . .	36
3.3.7	Modeling of Active SMP-based Designs . . . . .	36
3.4	Results and Discussion . . . . .	37
3.4.1	Material Characterization . . . . .	37
3.4.2	Validation of Model Accuracy . . . . .	38
3.4.3	Evaluation of Active SMP-based Designs . . . . .	38

3.4.4	Modeling of Active Auxetics . . . . .	39
3.5	Conclusion . . . . .	39
4	AUTONOMOUS DEPLOYMENT OF STRUCTURES . . . . .	43
4.1	Summary . . . . .	43
4.2	Background . . . . .	44
4.3	Method and Design . . . . .	45
4.3.1	Material Selection . . . . .	45
4.3.2	Programmable Unit Actuator . . . . .	46
4.3.3	Deployable Structures . . . . .	49
4.4	Results and Discussion . . . . .	51
4.4.1	Programmable Unit Actuator . . . . .	51
4.4.2	Deployable Structures . . . . .	52
4.5	Conclusion . . . . .	53
5	AUTONOMOUS ROBOTIC PROPULSION . . . . .	55
5.1	Summary . . . . .	55
5.2	Background . . . . .	56
5.3	Method and Design . . . . .	57
5.3.1	Propulsion Element . . . . .	57
5.3.2	Swimming robot . . . . .	59
5.3.3	Sequential and Directional Propulsion . . . . .	60
5.3.4	Cargo Delivery and Reverse Navigation . . . . .	61
5.4	Results and Discussion . . . . .	62
5.4.1	Propulsion Element . . . . .	62
5.4.2	Swimming Robot . . . . .	63
5.4.3	Sequential and Directional Propulsion . . . . .	65
5.4.4	Cargo Delivery and Reverse Navigation . . . . .	65
5.5	Conclusion . . . . .	66
6	GENERATIVE DESIGN OF MULTI-STABLE SURFACES . . . . .	69
6.1	Summary . . . . .	69
6.2	Introduction . . . . .	70
6.3	Method and Design . . . . .	72
6.3.1	Meshing of the Surfaces as Chebyshev Nets . . . . .	72
6.3.2	Design of the Reconfigurable Structure . . . . .	74
6.3.3	Design of the Quadrilateral Unit Module . . . . .	74
6.3.4	Materials and Fabrication . . . . .	76
6.3.5	Design of a Modified Bistable Mechanism . . . . .	76
6.4	Results and Discussion . . . . .	77
6.4.1	Design and Fabrication of a Multi-stable Surface . . . . .	77
6.4.2	Meshing Sensitivity . . . . .	79
6.4.3	Example of Encapsulation . . . . .	80



6.4.4	Example of Large Scale Structure . . . . .	81
6.5	Conclusion . . . . .	81
7	SELF-DEPLOYING SOLAR PANELS . . . . .	83
7.1	Summary . . . . .	83
7.2	Background . . . . .	84
7.3	Method and Design . . . . .	86
7.3.1	Hoberman Ring . . . . .	86
7.3.2	Elastic “Flasher” Origami . . . . .	89
7.3.3	Solar Panel: Fabrication and Assembly . . . . .	94
7.4	Results and Discussion . . . . .	94
7.4.1	Hoberman Ring . . . . .	94
7.4.2	Elastic “Flasher” Origami . . . . .	96
7.4.3	Solar Panel . . . . .	97
7.5	Conclusion . . . . .	98
8	DISCUSSION AND OUTLOOK . . . . .	101
8.1	Principle Findings and Contributions . . . . .	101
8.2	Outlook . . . . .	104
8.2.1	Multi-Functional Smart Polymers . . . . .	104
8.2.2	Multi-Scale Additive Manufacturing . . . . .	105
8.2.3	Multi-Dimensional Bistable Mechanisms . . . . .	105
8.3	Conclusion . . . . .	106
	BIBLIOGRAPHY . . . . .	109



## INTRODUCTION

---

### 1.1 SUMMARY

A traditional mechanical engineering design paradigm involves the design of components and the assembly of these components into a coherent system. Each component is itself a sub-assembly designed to serve a particular function. As engineering design challenges increase in their complexity, and broaden their target length scale and environments, this paradigm may increasingly be a limiting factor with issues such as component miniaturization and heavy actuation.

In this thesis, I introduce a new way of designing complex mechanical systems using a material-based approach and demonstrate this approach using a multi-material jetting 3D printer. In particular, I exploit the combination of shape memory polymers and mechanical instability to design autonomous machines. In addition to investigating the fundamentals of these two topics, two broad classes of engineering systems are used to demonstrate the underlying principles proposed in this thesis. The first focuses on functional reconfiguration and deployment of structures, the second focuses on the propulsion of locomotive robots. These are mechanical engineering design challenges that are classic, yet relevant. Their increased design complexity requires computational generative design tools and more advanced fabrication techniques. Both of these area are also addressed in this thesis.

Deployable and reconfigurable structures have seen many engineering applications at different scales in architecture, engineering, medicine, and other fields where geometric and functional transformation bring great benefits. This is stated with the valid assumptions that 1) collapsed or flat systems cost less to transport, and take less time to fabricate, and 2) autonomous deployment of these systems allows a much wider range of applications where manual deployment is not feasible. Thus far, 3D printing of reconfigurable systems in literature have demonstrated manually designed shape morphing objects without the associated functional benefits. This is due to the lack of 1) structural stability in the morphed shape, 2) simulation tools to predict autonomous shape morphing, and 3) computational generative algorithms to tackle the inverse problem of designing an object that morphs to given targeted shapes. This thesis demonstrates a solution to these challenges through increasingly complex design tasks.

Autonomous locomotive robots have traditionally been designed with an assembly of power supplies, actuators, and controls. There is an inherent lower limit that these components can still function, whereas a material-based propulsion system may circumvent this problem [1]. With a material-based design approach, analogs of these components are proposed and demonstrated. While similar work in literature has shown robotic appendage movement,

propulsion remains elusive [2]. This thesis aims to exploit the unique capabilities of 4D printing to tailor functionalities to given applications. The resulting robot is the first of its kind to achieve untethered material-based propulsion.

This chapter describes the fundamental sciences and technologies that are used in subsequent chapters. The goal and hypotheses are stated, followed by a chapter by chapter outline.

## 1.2 BACKGROUND

In the context of mechanical engineering, design often goes hand in hand with the development of novel materials and the understanding of new physics. The industrial revolution was largely driven by the studies in thermodynamics, the invention of the steam engine and the design of automated machines. The next major development was initiated by the fundamental studies on semi-conducting materials, the development of micro-fabrication of integrated circuits and the subsequent invention of computers. Fast forward to the present, we may very well be on the cusp of the next revolution.

3D printing is one of the advanced manufacturing technologies where raw materials are selectively added to form a design, hence the term additive manufacturing. This is in contrast to technologies such as milling, laser cutting or lathing, where materials are subtracted away from a bulk base material. 3D printing offers the designer the capability to fabricate almost anything.

In parallel to the advancement of fabrication technologies and development of novel materials, we are beginning to tackle increasingly difficult engineering challenges. As we explore increasingly inaccessible environments at different length scales, heavier demands are placed on the design of mechanical systems and civil structures.

In this thesis, I investigate the design of mechanical systems through autonomous functional transformation enabled by combining mechanical instability and functional materials. In this section, I summarize the state of the art in 3D and 4D printing, functional materials and mechanical instability.

### 1.2.1 4D Printing: 3D Printing of Functional Materials

Traditionally, mechanical systems are designed with a combination of active and passive components acting in concert to perform the desired functions. With the addition of a control strategy and power supplies, the active components drive the passive components that provide structural stability.

I argue that the design of a mechanical system with the component to assembly approach is inefficient, and not sufficiently utilizing the erroneous freedom offered by advanced fabrication technologies. The advances in manufacturing technologies and materials may change this design process and blur the line between active and passive. These technologies are enabling

the fabrication of materials with environment dependent properties and encoding them to functionalities as the design is printed. Here, I summarize the different technologies in the context of design of future mechanical systems.

In this work, I focus on photo-polymerization based fabrication technologies. While there are many different physical implementations of this process, e.g. Stereolithography, Material Jetting, Direct Ink Writing, Continuous Liquid Interface Production, Two-Photon Polymerization, etc, the underlying chemistry remains the same. A photopolymer is used as the build material. Initially liquid, the photopolymer consists of monomers, oligomers, and photoinitiators. From UV light exposure, the monomers and oligomers cross-link to form long polymer chains. Macroscopically, the liquid hardens to form a solid. By either filtering the UV light, or by selectively depositing the photopolymer, one is able to fabricate a design in a layer-by-layer fashion.

In the recent decade, numerous advances are made at the intersection of material science and engineering design. Engineers have traditionally designed by assuming material behavior as linear elastic, structural deformation as small and linear, and linkages as comprised of rigid bars and perfect joints. Increasingly, with the proliferation of new 3D printable materials, and polymers and other “soft” materials in particular, such assumptions are no longer valid. As polymers of varying stiffnesses can be fabricated with relative ease, one must consider the non-linear mechanical behavior of the materials. The distinction between rigidity and compliance is blurred as materials can be made at different Young’s modulus ranging from 1 to 1000 MPa. Such materials also typically exhibit an hyper-elastic behavior [3].

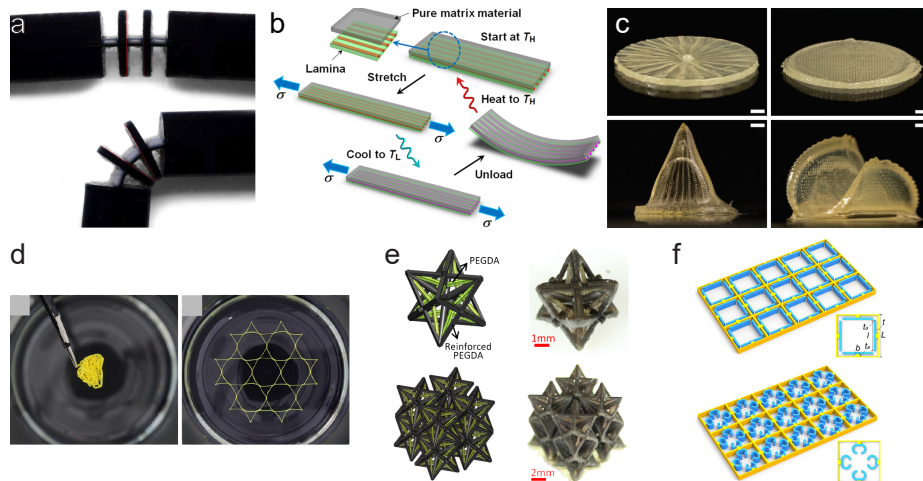


FIGURE 1.1: Different functional material showing post-fabrication behavior. a) Swelling hydrogels are printed offset from the neutral axis, allowing the joint to bend [4]. b) Shape memory polymers are printed within a compliant matrix, with a pre-tension, the strip curves [5]. c) Nematic order is created following the deposition of the nozzle, allowing for programmed deformation in liquid crystal elastomers [6]. d) A demonstration of the shape memory effect [7]. e) Negative thermal expansion using multi-material fabrication [8]. f) An application in attenuation of excitation [9].

With the Two-Photon Polymerization process (e.g. the Nanoscribe), one is able to fabricate designs with features on the nanometer to micrometer scale. This is used by engineers to design hierarchical structures that are uniquely resilient, impact resistant and lightweight [10].

In the field of meta-materials, such a fabrication process allows the fabrication of synthetic materials that are comprised of potentially millions of repeating units. These repeating units may start resembling the crystalline structure of metallic alloys both in number and in arrangement. Defects can be introduced to both the periodicity of the arrangement, or within each individual unit.

With the Material Jetting process (e.g. Stratasys Connex3 Objet500), one is able to simultaneously deposit multiple types of liquid photopolymer onto the same build plate. In the context of mechanical design, this allows the engineer to selectively assign rigid and flexible regions. This approach fits perfectly with the topology optimization algorithm, since the algorithm requires the discretization of the volume into voxels, and inherently assigns a spectrum of stiffness to the voxels [11]. Used extensively in this work, this process offers the possibility to fabricate whole systems in one print, and at the same time embed functionalities within the system through material selection.

Moving beyond using material as structural components, multi-physical behavior of polymers are exploited to provide additional functionalities to the mechanical systems (Fig. 1.1). For example, in place of a linear actuator, one can print a moisture-expanding polymer inside a flexible elastomer. When exposed to water, this design will expand and perform the same function as a linear actuator, minus the need for a power supply or a switch control. Such 3D printed designs using a functional material have been termed 4D printing. 4D printing refers to a design that is able to perform a certain desired function after fabrication, such as changing its shape when exposed to a stimulus [12]. Numerous functional materials have been developed to respond to different stimuli and to exhibit different behavior. In addition to swelling [4], light [6], chemically [2], and thermally [13] activated materials have been developed.

### 1.2.2 *Mechanical Instability*

In concert with non-linear material behavior, computational tools have enabled the analysis of geometrically non-linear deformation. In particular, once studiously avoided, mechanical instability is increasingly utilized as a mean of achieving large scale effects precisely due to its non-linearity. Mechanical instability in general describes a dynamic system whose trajectory is affected by a small perturbation. In the static sense as I employ it, it is referred to as buckling, in particular a bifurcation behavior called saddle-node bifurcations.

Nature has evolved a number of unstable mechanisms ranging from the Venus Flytrap to the pistol shrimp. They exploit rapid shape transformation in the snapping of unstable mechanisms to capture or stun prey. Mechanical instability has also been used in a number of engineering applications. In particular, engineers have utilized snap-through instability to achieve functions including the amplification of responses [14], energy absorption [17] and propagation of signals [15]. Fig. 1.2 show a selected example of man-made unstable systems, going from one to three dimensional behaviors.

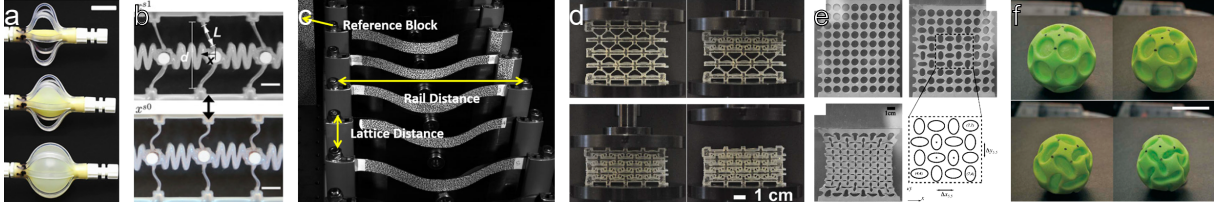


FIGURE 1.2: Man-made unstable systems. a) Amplification of displacement in a pressurized system [14], b,c) Soliton behavior shown with two types of bistable mechanisms [15, 16], d) A periodic tiling of bistable mechanisms creating an energy absorbing material [17], e) Controlled collapse behavior [18], f) Same deformation mapped to a spherical object under negative pressure [19].

Bistability is a type of instability that has two energy minimum, i.e. two distinct equilibrium states. The properties that make a bistable mechanism attractive in the context of engineering applications can be characterized by its static and dynamic behavior. Statically, a bistable mechanism can amplify the force and/or displacement of the system. The amplification of force can be seen in the context of the second equilibrium state, where a triggering force is needed to revert the bistable mechanism back to the first equilibrium state. This is in contrast to a linear elastic material where one only needs to remove the applied force to return it to its equilibrium state. In terms of displacement, one only needs to apply a small displacement to a bistable mechanism until it triggers, then it will snap to its second equilibrium state, thereby resulting in a much larger displacement than was applied. Its dynamic behavior can be characterized by the snapping motion that occurs when a bistable mechanism move from the first to the second equilibrium state. The high velocity attained during snapping can be exploited to give momentum to a mechanical systems.

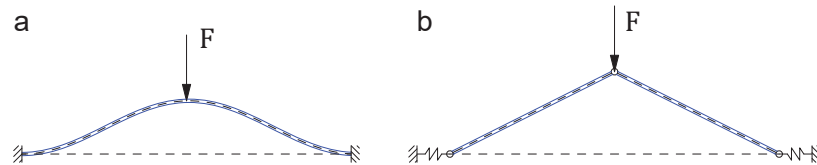


FIGURE 1.3: Two 1-dimensional bistable mechanisms. a) Beam in the shape of a buckled column. b) Von-Mises truss. These two mechanisms can be observed in series in Fig. 1.2b,c.

While these characteristics are shared among many bistable mechanisms, due to ease of analysis and fabrication, two simple mechanisms are used almost exclusively in engineering applications thus far. The first is fabricated in the shape of the first buckling mode of a doubly clamped beam (Fig. 1.3a), where it can be described by  $\cos(x)$  where  $x = [0..2\pi]$ . With a perpendicular force applied at the apex  $F$ , the shape would essentially snap to its mirrored image  $-\cos(x)$ . The second, even simpler shape, consists of two angled truss members joining at an apex (Fig. 1.3b). They are supported at the boundaries by linear springs. Rotational joints are assumed to be hinges.



### 1.2.3 Shape Memory Effect in Polymers

Most thermoset plastics are amorphous and have a glass transition temperature  $T_g$ . The stiffness of these polymers decrease by several orders of magnitude when heated above their  $T_g$ . Likewise the elastic strain increases.

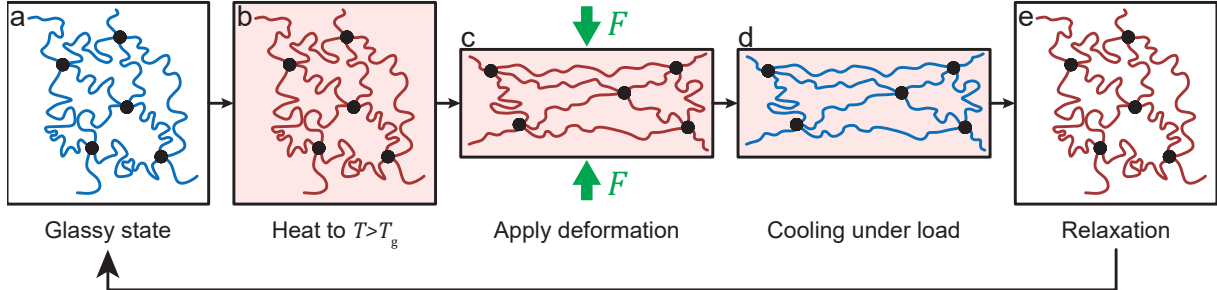


FIGURE 1.4: Stages of the shape memory cycle of 3D printed polymers. a) The polymer is fabricated in its glassy state. b) When heated, the stiffness of the polymer material decreases significantly. c) A force is applied to deform the polymer to a desired shape. d) The polymer is cooled down and its deformed shape is fixed. e) When the environmental temperature increases, the polymer recovers its permanent or fabricated shape.

The shape memory effect in polymers refers to the ability for the polymers to remember their permanent shape after being deformed. The process is two fold (Fig. 1.4). First (a) the polymer is fabricated. Then (b) it is heated past its  $T_g$  and (c) deformed to the desired secondary shape. With the force still applied, (d) the polymer is cooled to below its  $T_g$ . After cooling the force is removed and the polymer will stay in its deformed state. This is the programming phase of the process. When desired, the “programmed” polymer is reheated, (e) whereby it autonomously relaxes and transforms itself back to the permanent state. It is the last step that I exploit in conjunction with the bistable mechanism to create autonomous machines.

### 1.2.4 Soft Autonomous Robotics

Due to its ubiquity, robotic systems have been used as a classic design example. Soft and micro-robotics have received particular attention. Inspired by the physiology of living organisms, soft robots offer increased flexibility and improved robustness in uncontrolled environments. They also provide a safer working environment, allowing humans to work in the same space. Earlier designs show how each component of a rigid robot can be made compliant (Fig. 1.5a). Utilizing silicone casting, pneumatic channels can be embedded within a compliant frame, allowing for controlled actuation (Fig. 1.5b), this externalizes the control and motor components. A self-folding origami shows embedding of components within a compliant substrate (Fig. 1.5c). Most recently, an entirely soft pneumatic robot is fabricated. It is powered by the controlled release of an embedded propellant. In this thesis, I will tackle the problem of autonomous locomotion and transformation within the context of robotics.



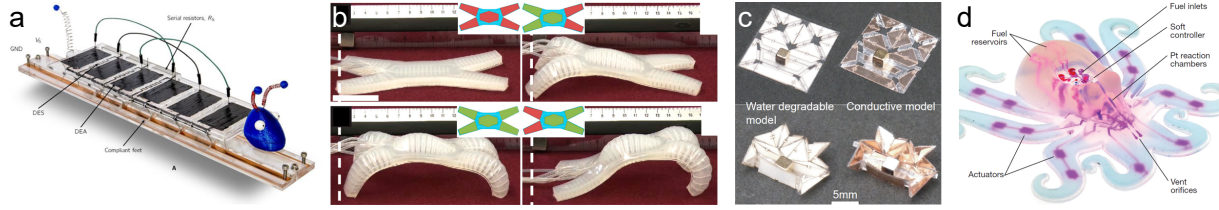


FIGURE 1.5: Next generation robotic systems. a) First demonstration of a soft robot that eliminates electronics [20], b) Pneumatic multi-gait robot [21], c) Magnetically actuated untethered robotic system [22], d) First demonstration of an untethered autonomous robot that is entirely soft [2].

### 1.2.5 Design of the Next Generation Mechanical Systems

In the past two decades, researchers have begun exploring computational design of mechanical systems in earnest. The new fabrication capabilities offer enormous design freedom that is starting to be explored. Yet limited research exist in the computational design and optimization of 3D printing of autonomous machines.

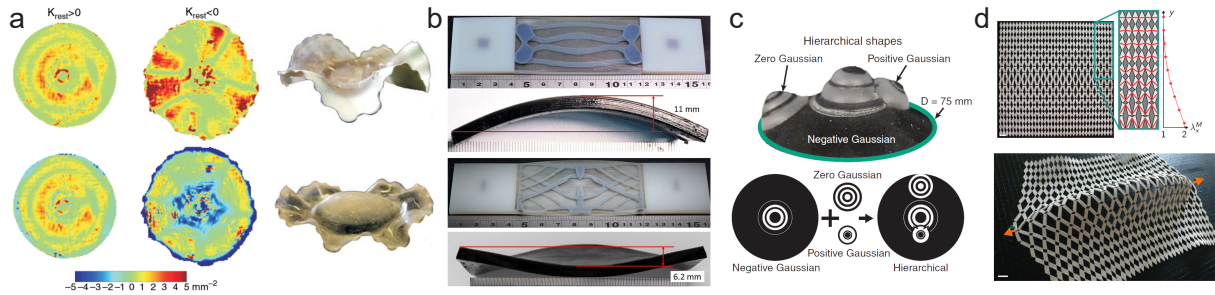


FIGURE 1.6: Solutions to the inverse problem of designing a flat object that transforms to a desired shape. a) Direct prescription of Gaussian curvature achieved through shrinkage [23]. b) Shape memory polymer placement using level set topology optimization [24]. c) Pneumatic actuation of regions with different extensibility [25]. d) Out-of-plane shape transformation resulting from in-plane deformation [26].

The first exploration this field focuses on the fabrication of a flat object that when activated, transforms itself into a desired shape. Most proposed methods (Fig. 1.6) are limited in the range of achievable shapes, difficult to fabricate, and typically returns to the flat shape when the external force or pressure is removed. As shown in Fig. 1.6, the desired shapes are typically described through their curvature. This thesis proposes a method to tackle a similar inverse design problem while addressing these limitations.

### 1.3 SCOPE AND OUTLINE OF THE THESIS

The rapid advancements in 3D printing offers tremendous technological advantages in the fabrication of new generation complex systems. It is the design of mechanical systems using 3D printing of functional materials in conjunction with bistable mechanisms that this thesis investigates. The main research question of this thesis is thus:

**Main research question** How can I design mechanical systems that achieve autonomous functional transformation using a materials-based approach?

In addition to answering the research question, the following hypotheses are stated.

- Mechanical bistability can provide different stable configurations as well as momentum when snapping between the equilibrium states.
- Shape memory polymers can power controlled autonomous transformation.
- Designs consisting of bistable mechanisms and shape memory polymers with tunable mechanical properties can uniquely be fabricated using multi-material 3D printing.
- The combination of the two offers engineers enormous design freedom, enabling the autonomous deployment of structures and dynamic propulsion of robotics.
- Computational methods must be developed to leverage this new design freedom.
- By demonstrating a credible solution to an existing engineering challenge, this thesis contributes to a new paradigm of mechanical engineering design.

The body of this thesis consists of six distinct yet connected chapters (Fig. 1.7). Each chapter begins with an in-depth background, and then tests one or more of the aforementioned hypotheses and demonstrates their validity. Chapters 2 and 3 serve as the fundamental building blocks that are used in the design of the following systems. Chapter 2 proposes a bistable mechanism uniquely designed for multi-material 3D printing. The stroke length of this bistable mechanism is maximized, while its two equilibrium configurations are characterized. To demonstrate multi-stability, multiple instances of the mechanism are embedded in a 2D lattice frame. By triggering the mechanisms, multi-stable 3D shapes are achieved. Chapter 3 investigates the shape memory properties of the printed polymers and the applicability of such polymers for autonomous transformation. The glass transition temperature of the available 3D printed polymers are measured. Then a detailed thermo-viscoelastic characterization is performed for a selected polymer. A viscoelastic constitutive model is constructed for finite element analysis.

To demonstrate autonomous mechanical systems, the shape memory polymer is used to trigger the designed bistable mechanism in the deployment of structures (Chapter 4) and in the propulsion of robots (Chapter 5). Chapter 4 demonstrates deployable structures that can be transported in its flat configuration without mechanical restraints. When exposed to heat, either from the environment or through artificial means, the structure will deploy into its functional configuration autonomously. Load bearing capability is shown both during deployment and after. This is achieved through the load amplification characteristics of the bistable mech-

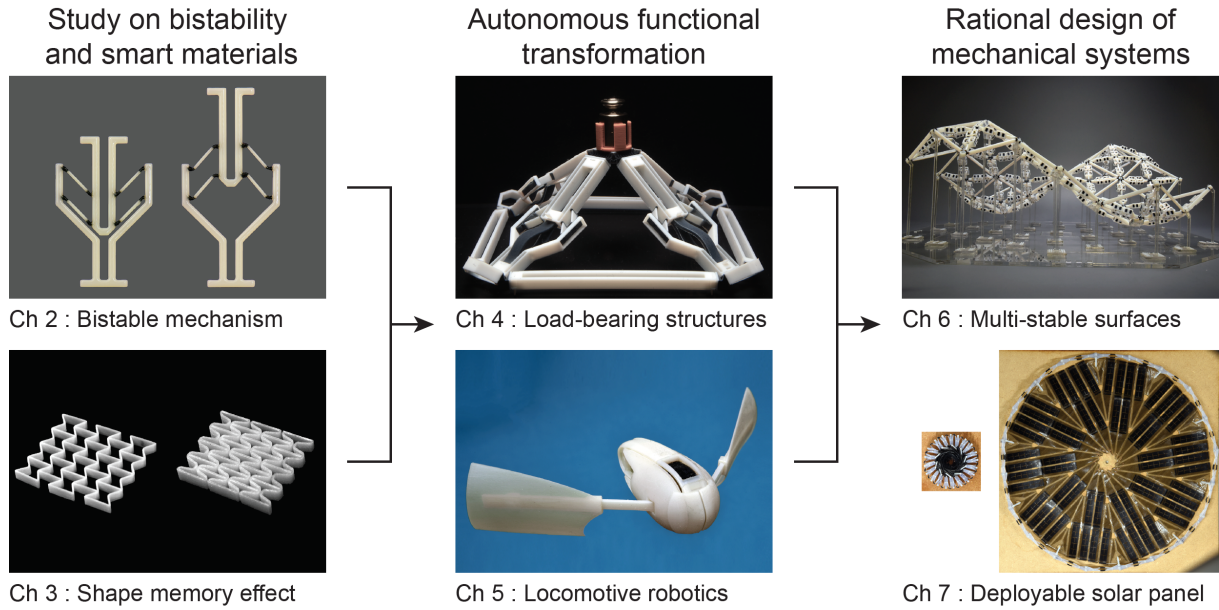


FIGURE 1.7: The body of the thesis consists of six chapters. Chapter 2 proposes a bistable mechanism fabricated using multi-material 3D printing. Chapter 3 investigates the fabricated shape memory polymers. Chapter 4 and 5 demonstrate two applications resulting from the combination of shape memory polymers and the bistable mechanism. Chapter 6 proposes a generation method for multi-stable surfaces. Chapter 7 uses a self-deploying solar panel to illustrate a real world application of multi-material functional fabrication.

anisms. Chapter 5 presents the first instance of a locomotive soft robot that is powered using inherent material properties. Through the use of a shape memory muscle as a power supply, and a bistable mechanism that acts as a motor, I demonstrate an autonomous swimming robot that reacts to the surrounding temperature. By changing the reaction time and temperature of the muscle elements, it becomes possible to sequentially activate an array of bistable motors, allowing for directional movements and reversal.

Moving beyond proof-of-concept demonstrations, I propose a computational method for the design of reconfigurable surfaces (Chapter 6). Literature mostly design shape morphing objects in a trial-and-error manner. However, for the design of more complex systems, a computational approach is needed. Following Chapter 2 on the bistable mechanism, I pose an inverse problem whereby given one or more target shapes, what is the shape of a flat structure that can deploy to assume these shapes while achieving stability.

In Chapter 7, a real world example of a material-based autonomous machine is presented from design to fabrication. For aerospace applications, the generation of power is a difficult engineering challenge. Solar panels are routinely used on satellites and other space systems. Numerous strategies have been devised for the stowage and deployment of solar panels. Often the supporting components consume a significant portion of the given volume and mass. In this chapter, I propose a self deploying solar panel expands its area by a factor of ten when exposed to higher temperature.

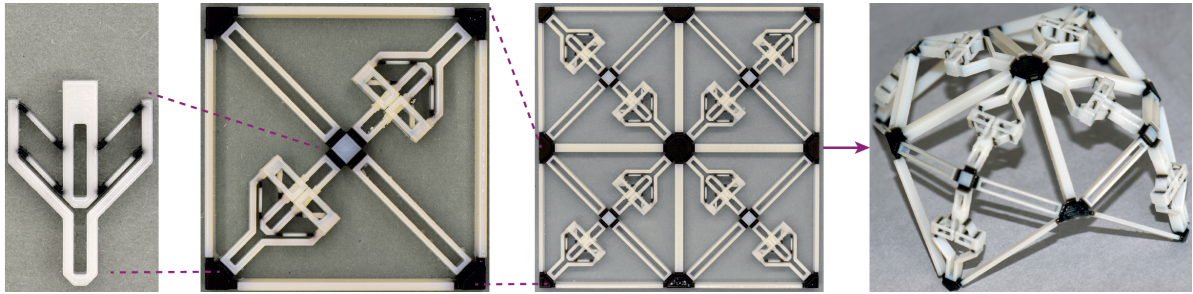
This design process also illustrates several guidelines unique to multi-material 4D printing of functional systems: 1) distributed self-actuation provides redundancy during the deploy-

ment process, 2) multi-functionality is achieved using the shape memory polymers as they provide the necessary actuating force when heated, but act as the structural elements when cooled. 3) Material failure is inherently impossible during the deployment phase. Since it is fabricated in the deployed shape and subsequently programmed into the stowed configuration, during deployment, stress within the material decreases.

With these guidelines and the principles illustrated in this thesis, a new generation of autonomous tailored machines are designed to address ever more demanding engineering challenges.

## BISTABLE MECHANISM AND MULTI-STABLE DEPLOYABLE STRUCTURES

---



The content of this chapter has been previously published in *Scientific Reports*,

Chen, T., Mueller, J. & Shea, K., (2017), Integrated Design and Simulation of Tunable, Multi-State Structures Fabricated Monolithically with Multi-Material 3D Printing, *Scientific Reports*, 7, 45671.

### 2.1 SUMMARY

Multi-material 3D printing has created new opportunities for fabricating deployable structures. We design reversible, deployable structures that are fabricated flat, have defined load bearing capacity, and multiple, predictable activated geometries. These structures are designed with a hierarchical framework where the proposed bistable actuator serves as the base building block. The actuator is designed to maximize its stroke length, with the expansion ratio approaching one when serially connected. The activation force of the actuator is parameterized through its joint material and joint length. Simulation and experimental results show that the bistability triggering force can be tuned between 0.5 and 5.0 N. Incorporating this bistable actuator, the first group of hierarchical designs demonstrate the deployment of space frame structures with a tetrahedron module consisting of three active edges, each containing four serially connected actuators. The second group shows the design of flat structures that assume either positive or negative Gaussian curvature once activated. By flipping the initial configuration of the unit actuators, structures such as a dome and an enclosure are demonstrated. A modified Dynamic Relaxation method is used to simulate all possible geometries of the hierarchical structures. Measured geometries differ by less than 5% compared to simulation results.



## 2.2 BACKGROUND

An reconfigurable structure is able to change its geometry or function after it has been constructed. Such attributes are observed both in nature and in human-made artifacts. Mechanically reconfigurable structures have seen applications that largely fall into two categories: deployment and energy absorption. Deployment involves transforming a device between desired geometrical configurations; common applications are in robotics [27] and morphing structures. [28] Energy absorption is a newly investigated field where an active structure deforms predictably under impact and absorbs kinetic energy. [29]

Bistability is one increasingly explored route towards achieving geometrical or functional changes within a structure. One can group such structures by their applications in either energy-related or motion-related fields. [30] Impact absorption [29] [31] [17] is one energy-related field that has seen increased attention. Examples of motion-related applications may include robotic manipulators, active building facades, HVAC systems, large scale space structures [28] and trapping mechanisms. [32]

Complex activation is often achieved through the tiling of multiple bistable units. With morphing, Schioler and Pellegrino [28] convert a static truss to an active one by replacing some of the members using bistable mechanisms. Utilizing 3D printing, Restrepo et al. [29] and Shan et al. [17] connected multiple bistable mechanisms respectively to form 2D energy absorbing blocks.

Han et al. [33] proposed a quad-stable mechanism and commented on the parameters influencing the structure, in particular the rigidity of the frame constraining the buckling elements. In Oh and Kota, [34] a rotational quad-stable mechanism was proposed. It shows a hierarchical structure where the outer bistable mechanism uses the inner one as a pin. Oh and Kota also stated that by designing the mechanism in a single layer, it can be manufactured in one piece.

An attractive feature of bistability is that energy input is only needed to transform the structural state but not to maintain the state. Using a bistable mechanism, as in this work, is novel compared to others who use swelling or prestressing to achieve large magnitude activation. Mao et al. [13] utilize the shape-memory effect of thermal plastics to “lock-in” prestress, and achieve shape change through temperature variation. Raviv et al. [4] achieve large state changes through swelling of strategically printed hydrogel.

Both Mao et al. [13] and Raviv et al. [4] fabricate their designs using a multi-material Inkjet 3D printer able to deposit materials with varying stiffness. These and additional works connecting 3D printing and activation were reviewed by Choi [35] who noted significant reduction in transportation volume and weight when compared with conventional assemblies. However, shortcomings are that the designs do not demonstrate predictable reversibility, the activated state cannot be precisely controlled and there is no defined load bearing capability.

In this work, the same 3D Inkjet printing technology as Mao et al. [13] and Raviv et al. [4] is used to fabricate proof-of-concept deployable structures that overcome the aforementioned

challenges. Utilizing hierarchical principles, [10] I start by designing a unit bistable mechanism based on the Von Mises Truss (VMT). [36] Then, deployable structures are created using multiple instances of the proposed mechanism. The resulting designs possess multiple equilibrium states and are fabricated flat and activated to 3D structures. This extends the state of the art in 3D printed, deployable structures and provides the foundation for novel self-assembling and active structures.

First the fabrication process and method to characterize the fabricated bulk materials are described. Then the design of the bistable mechanism as well as the design of the hierarchical structures are discussed. The experiments and simulation procedure are detailed. The results and discussion section, presents the mechanical properties of the bulk material, simulation and experimental results of the bistable mechanism and of the hierarchical structures.

## 2.3 METHOD AND DESIGN

### 2.3.1 Multi-Material Fabrication

#### 2.3.1.1 Fabrication Technology

The designs presented in the thesis are tailored to be fabricated with a multi-material 3D printer, Stratasys Objet500 Connex3. This printer achieves multi-material printing by depositing and mixing liquid photopolymers from an array of nozzles in a layer by layer additive fabrication process. UV light cures the recently printed layer before the print platform lowers and the next layer is printed. This allows different materials to be assigned to any region of a design. The printer accepts up to three base materials and one support material. Digital materials (DMs) denote the intermediate materials created at the time of printing by jetting and curing two different base materials at the same location. As uncured materials are in a liquid state, support material is needed under all overhanging geometry.

12 DMs can be printed by the mixing of two base materials, yielding 14 different material combinations for each pair. Of particular interest are the mixtures between TangoBlack-Plus(TB+), an elastomer-like material, and VeroWhitePlus(VW+), a rigid plastic. The resulting DMs have varying mechanical properties (Fig. 2.1).

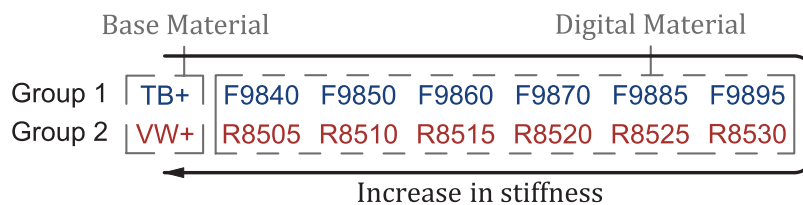


FIGURE 2.1: Available materials of the multi-material Printer. TB+ and VW+ are the base materials representing the most compliant and stiffest ends of the spectrum respectively. The 12 digital materials created at the time of printing with different mixture of TB+ and VW+ are shown. Direction of stiffness increase is indicated.

### 2.3.1.2 Bulk Material Characterization

Since the simulation of the bistable mechanism involves large deformation of the compliant joints, a complete stress-strain model for each material is constructed. The material manufacturer provides the Young's Modulus for the seven DMs on the rigid end of the spectrum but not for the flexible ones. Stanković et al [37]. presented the Young's Modulus of all 14 materials, showing large deviations from the manufacturer's specification. The deviations were attributed partly to unknown test conditions [38]. As bistability entails large deflection [39] and finite strain behavior of the elastomers, quasi-static tensile tests are conducted under constant environmental conditions to obtain complete stress-strain models for each DM.

Type V geometry of the ASTM D638-10 test standard for tensile testing of plastics is adopted for all specimens. Three identical test specimens are printed for each material under an ambient temperature of 21 °C. To eliminate the impact of uncontrolled factors on the mechanical properties [38], each is printed on a separate tray. Aside from the material combination, all other factors are held constant. Tensile tests are conducted on an Instron ElectroPuls 3000 with either a 100 N or a 5000 N load cell, depending on the material tested. Under displacement control, a testing speed of 20 mm min<sup>-1</sup> is set and the specimens are elongated until fracture.

### 2.3.2 Bistable Unit Element

#### 2.3.2.1 Bistability Principle and Geometrical Design

The goals of the bistable mechanism design are: 1) it must exhibit bistability, 2) the stroke length should be maximized and 3) the critical force should be made adjustable. In relation to the overarching goal of printing deployable structures, the bistable mechanism itself must be printable as a flat part and allow for serial and parallel connection.

A bistable mechanism exploiting the limit point buckling behavior is proposed. The Von Mises Truss (VMT) was first introduced in 1923 [36] as a structure that features two pin jointed members with a vertical load at the apex (Fig. 2.2a). A geometrically non-linear formulation of the problem offers force displacement diagrams as shown in Fig. 2.2b [40].

In Fig. 2.2, points  $U$  and  $D$  are the equilibrium states when the load  $F$  is zero.  $M_1$  is the critical point at which an infinitesimal increase in load triggers instability. With this increase in load, the structure snaps, after which the VMT mirrors itself along the horizontal axis. With a further increase in load, the members experience tension and eventually rupture. If the load is displacement controlled, past point  $M_1$ , the reaction force decreases and eventually reverses orientation past point  $N$  and reaches a minimum between point  $N$  and  $D$ . Note that the symmetric behavior above is achieved only if the stiffness of the rotational spring is zero,  $k_\theta = 0$ . The thinner curves in Fig. 2.2B show possible asymmetric behaviors [41].

Schioler et al. [28] and Shan et al. [17] have physically realized such a bistable mechanism at different length scales and using different fabrication process. Schioler stated that compared to an Euler buckling based bistable mechanism (e.g. [29], [42]), the stroke length provided by



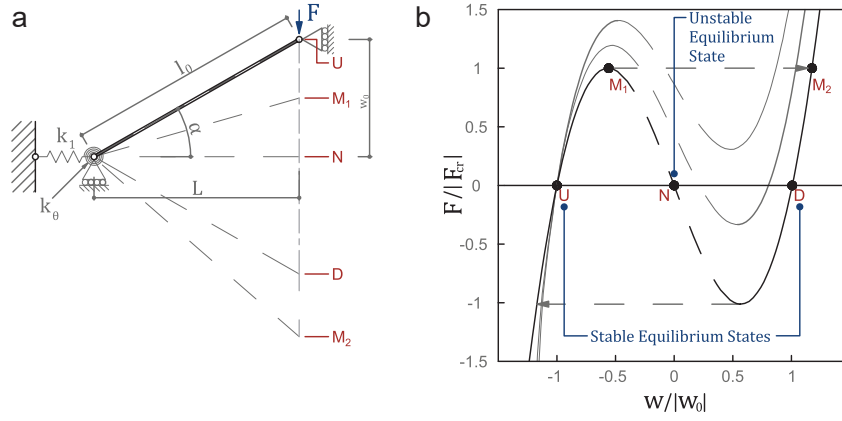


FIGURE 2.2: a) VMT consisting of a truss member with geometric variables and critical points labeled, b) Possible force displacement curves of a VMT.

VMTs is much smaller due to the large strain induced in the joints. To overcome this limitation and to accomplish the aforementioned goals, the bistable mechanism shown in Fig. 2.3 is proposed.

The design consists of a bracket, four trusses and a pin. Two vertically stacked VMTs ensure that all DOFs except in the vertical direction are restricted [28, 43]. The bracket, the pin and the center portion of the trusses are fabricated with VW+, and are much stiffer than the joints. The inclination angle of the truss members is set to  $\alpha = \tan(w_0/L) = 45^\circ$  and is below the theoretical limit [40]. With this inclination, the stroke to length ratio of serially connected mechanisms approaches 100 %. This is significantly larger than bistable designs using the Euler buckle shape, e.g. Restrepo et al. [29] at 16 %, or ones based on VMTs, e.g. Schioler and Pellegrino [28] at 29 %, Barbarino et al. [44] at 24 % and Haghpanah et al. [45] at 20 %.

$a$	$b$	$c$	$d$	$e$
6.825 mm	6.250 mm	6.675 mm	5.00 mm	1.25 mm
$f$	$g$	$h$	$w_0$	$L$
5.00 mm	2.00 mm	2.00 mm	4.50 mm	4.50 mm
$l_1$	$l$	$t$	$s$	$\alpha$
0.25 mm	1.0, 0.75, 0.50 mm	0.50 mm	0.50 mm	$45^\circ$

TABLE 2.1: Dimensions defining the mechanism shown in Fig. 2.3. Note that the trusses in the mechanism are dimensioned to be the minimum feature size that the Connex3 printer can reliably print. The remaining dimensions are sized accordingly.

### 2.3.2.2 Parametric Study of the Bistable Mechanism

With the stroke length maximized, the joint material and the joint length  $l$  are parameterized to study their effect on the overall behavior and the activation force. With such an mechanism design, it is seen that the necessary conditions for symmetric behavior is not met (Fig. 2.2b), further, the two stacked VMTs would experience different support stiffness.

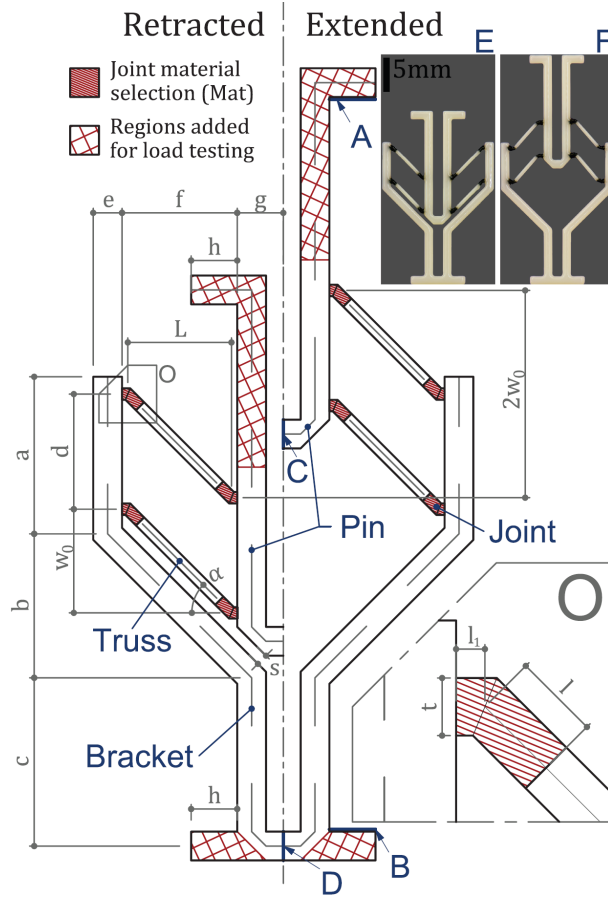


FIGURE 2.3: Drawing of the proposed bistable mechanism. The line-shaded region (zoomed in O) indicates the location of the joint and a change in material stiffness. The length of the joint  $l = 1.0, 0.75, 0.50$  mm is defined parametrically. Note that changing  $l$  does not change the overall geometry, i.e. if the joint lengthens, the truss member itself shortens. The cross-hatched regions indicate the additional structure added to facilitate load testing. These regions are removed in the designs presented in latter sections. A benchmark mechanism ( $l = 0.75$  mm, joint material F9860) is e) fabricated and f) activated. Parameter values are listed in Table 2.1.

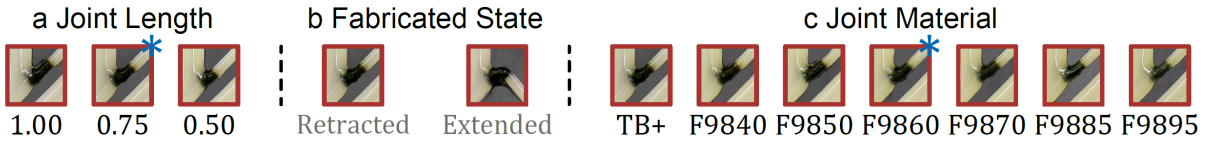


FIGURE 2.4: Joint length, initial state, and joint material are the design parameters studied. These are shown by focusing on one joint of the mechanism. \* denotes the benchmark model.

These complexities lead us to perform numerical and physical experiments. 42 models are included in the experiments, including seven different joint materials (Group one in Fig. 2.1), three length variations  $l = 1.0, 0.75, 0.50$  mm, and two initial configurations, i.e. retracted and extended (Fig. 2.4). This leads to 42 models (Table 2.2).

A physically and geometrically non-linear finite element simulation using beam elements is performed to predict the behavior of a bistable mechanism. The beam elements are placed at the center line of the real geometry. A vertical displacement of  $\pm 10$  mm is applied to line A of

	TB+	F9840	F9850	F9860	F9870	F9885	F9895
1.00 mm	1	5	9	13†	17	21	25
0.75 mm	2†	6†	10†	14†*	18†	22†	26†
0.50 mm	3	7	11	15†	19	23	27

TABLE 2.2: Specimen number, and the corresponding joint dimension and material. †denotes the specimens whose results are plotted in Fig. 2.9ABC, \* denotes the benchmark model

Fig. 2.3; line B is pin jointed. Symmetry conditions are imposed on points C and D. Material properties are obtained from the bulk material characterization.

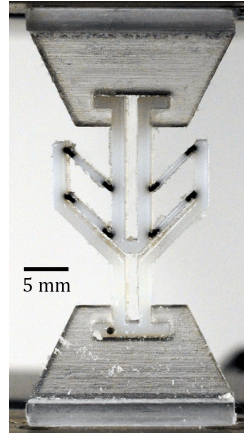


FIGURE 2.5: Load testing setup including the printed grippers to match the simulation boundary conditions.

To validate the simulation results, physical specimens are fabricated and load tested under tension or compression (Fig. 2.5). To ensure that the boundary conditions remain invariant across all models and are identical to the numerical simulations, a set of two customized grippers are printed to hold the specimens by the protrusions dimensioned  $h$  shown in Fig. 2.3. A displacement of  $\pm 10 \text{ mm min}^{-1}$  is set depending on the initial state. Both the actual displacement and the reaction force are recorded for each specimen.

### 2.3.3 Design of Hierarchical Structures

With in surveyed literature, multi-stable designs are achieved through clever stacking of bistable units. Similar to springs, one may connect bistable units in series, in parallel or both [46]. Concepts from [33] and [34] regarding frame rigidity, hierarchical design and flat printing are further developed in this work, where a bistable mechanism is used as the basic building block in the design of complex multi-stable hierarchical structures. The goals are to create load bearing structures that may be transported as flat sheets and have predictable deployed states. The first example stems from the construction of space frames. A typical space frame can be defined with the edges from a tetrahedral tessellation of a given volume. From this set of edges, one guarantees that the space frame is a load bearing truss structure. Here,

I design a tetrahedral module that is fabricated monolithically and that can be transported in 2D as a triangle and deployed.

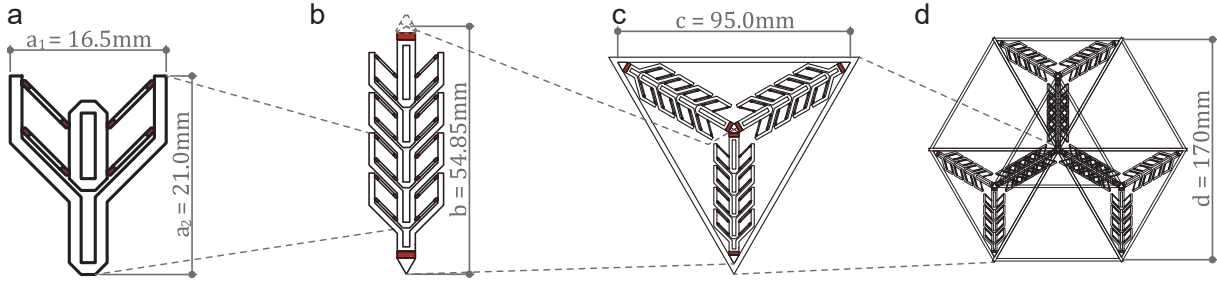


FIGURE 2.6: Designs of proof-of-concept tetrahedral structures. (A–D) Show the design of a tetrahedral space frame outlining the hierarchy from a single unit actuator (A) to a tessellation of tetrahedral modules (D).

Fig. 2.6 shows the levels of the design hierarchy from a single bistable mechanism to a tessellation of the tetrahedral modules. A regular tetrahedron with  $c$  as the length of each edge is used. The tetrahedral module consists of three edges of parallel mechanisms (Fig. 2.6b). When folded, these apex-connecting edges must retract into the base. Therefore, their length equals the radius of circumscribing circle of the base triangle  $b$ . One can create space-frame structures by tiling multiple instances of the triangle (Fig. 2.6c).

The second set of example demonstrate the versatility of the design by increasing complexity. These structures cannot be activated with a point load. There exists multiple, non-symmetrical activated states, and these states must be obtained with simulation. In particular, I demonstrate the design of 3D printed flat surfaces that can assume Gaussian curvatures in both the positive and the negative ranges with simple initial orientation and configuration changes of the bistable mechanism.

First, I design a unit module using the same bistable mechanism printed in retracted or extended configurations. The unit modules consist of two actuated and two rigid cross members in a flexible frame assuming pinned connections (Fig. 2.7a,b). Such a structure (i.e.  $\boxtimes$ ) is not statically determinate. When activating the mechanisms, internal stress develops in the rigid members in a planar analysis. However, as the joints accommodate out-of-plane rotation, the unit modules assume an activated shape in the third dimension.

Hierarchy is achieved by tiling these square unit modules in a two by two grid and restricting designs to those that are symmetric in both X and Y directions. As these structures act as proof-of-concept models, two configurations (Fig. 2.7c,d) are discussed in detail below: c) with retracted mechanisms positioned in a X shape towards the center and d) with extended mechanisms positioned in a diamond shape around the center.

### 2.3.3.1 Modified Dynamic Relaxation

Simulation of the hierarchical structures focuses on finding the activated states of structures rather than the activation forces. The simulation assumes that each mechanism is activated independently. This assumption remains valid as long as the truss network is determinant, i.e.

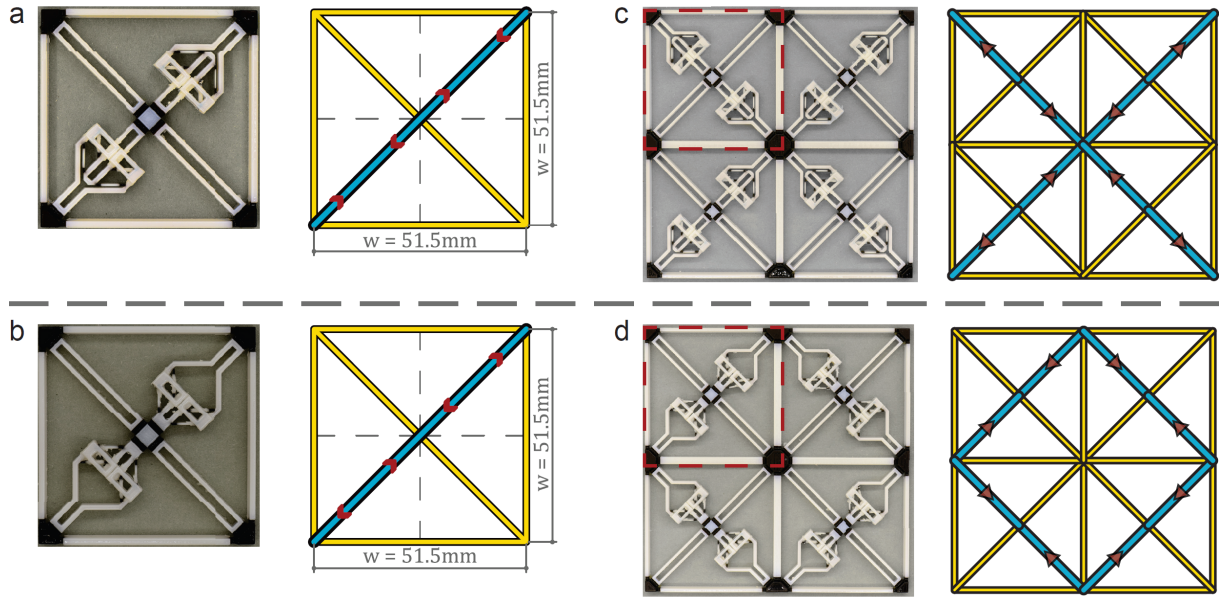


FIGURE 2.7: Hierarchical designs using square unit modules as the basis. Unit modules are shown in the retracted (a) or the extended (b) configuration. Two symmetric tiling of the unit modules are shown (c,d). The schematic shows yellow and blue members as rigid and active respectively.

there is no self-stress preventing activation, or in this case, allows movement in the third dimension. With the tetrahedral structures, the activated state is already known as each module is designed to reassemble a regular tetrahedron. A generalized simulation method is proposed to find the active form of more complex structures.

In literature, form finding of actuated structures has been done by explicitly deriving the geometric relationship between an independent variable (e.g. angle of inclination  $\alpha$  in Fig. 2.11) and the nodal coordinates. [47] Such derivation assumes that all mechanisms are activated, and attempts to converge on a solution that allows this length change while keeping the length of the static members constant. While such a process provides a parametric relationship for the geometry and thereby for further derivations such as finding the Gaussian curvature as a function of the stroke length, its practicability is limited to simple structures.

Here, a modified Dynamic Relaxation (DR) is used to find the active equilibrium configuration of the hierarchical structures. DR, often used in form finding, assumes that a grid structure can be estimated by a network of fictitious nodal masses and linear springs. [48] Introducing a fictitious time domain, the method updates the nodal coordinates based on the nodal residual forces in each DOF, and the resulting acceleration.

Four modifications on the classic formulation are introduced. One, no external force is applied. Instead, the rest length of the springs which contains bistable mechanism(s) has the stroke length added or subtracted from it. This is a form of pre-stressing that makes the 2D configurations unstable. Two, the force density matrix is updated at every iteration as a result of length change. Three, this unstable equilibrium must be perturbed to assume the 3D shapes. In physical systems, the perturbation usually takes the form of geometric imperfections. In the simulation, an upward initial velocity is added to an arbitrary node to

trigger the snapping behavior. Four, no nodal fixity is assumed, i.e. all nodal positions are updated at every iteration. Rigid body motion may occur as a consequence. Should static boundary conditions be necessary, the following derivation must be changed to account for only the free DOFs.

The algorithm summarized below is grouped into the initialization phase and the time iteration phase. To initialize the routine, step one is to construct the connectivity matrix of the structure consisting of  $n$  vertices, and  $m_e$  edges.

$$C_{k,p} = \begin{cases} \text{sign}(j - p) & \text{if } p = i; \\ \text{sign}(i - p) & \text{if } p = j; \\ 0 & \text{otherwise.} \end{cases} \quad (p = 1, 2, \dots, n) \quad (2.1)$$

where  $i$  and  $j$  are the nodes connecting the  $k$ th member.  $k$  and  $p$  iterates through every element and every node respectively. To obtain the activated length of each member, a stroke length array is defined as a modifier of the initial length. Note that to obtain all unique activated states, one must iterate through all combinations of the bistable mechanisms within a structure. The upper bound of all unique states is  $S = 2^n$  where  $n$  is the number of bistable mechanisms. Redundancy results when two or more mechanisms are connected in series, the overall stroke length is independent of which mechanism in the series is activated. The length modifier,  $l_{\text{stroke},k}$ , of the  $k$ th member is calculated as:

$$l_{\text{stroke},k} = n_{s,k} n_{a,k} s_k \quad (k = 1, 2, \dots, m_e) \quad (2.2)$$

where  $\mathbf{n}_a$  contains the number of mechanisms in each edge and  $\mathbf{s}$  is the stroke length of each mechanism. The initial state of the mechanisms is defined as follows,

$$n_{s,k} = \begin{cases} +1 & \text{retracted;} \\ -1 & \text{extended;} \\ 0 & \text{otherwise.} \end{cases} \quad (2.3)$$

Let  $\mathbf{x}^{t=0}$  be the coordinates of the initial nodes, the activated length of the structure can be calculated as follows. The array is rearranged into a diagonal matrix for later operations.

$$\mathbf{L}_a = \text{diag} \{ \|\mathbf{C}\mathbf{x}^{t=0}\| + \mathbf{l}_{\text{stroke}} \} \quad (2.4)$$

The iteration phase starts by setting  $t = 0$ . The member lengths are then calculated and collected into a diagonal matrix.

$$\mathbf{L}^t = \text{diag} \|\mathbf{C}\mathbf{x}^t\| \quad (2.5)$$

The definition of the force density matrix  $\mathbf{Q}$  is adapted from. [49]  $\mathbf{E}$  and  $\mathbf{A}$  are diagonal matrices containing the stiffness and the cross-sectional area of the members respectively. These can be identity matrices if all members are identical in mechanical properties.

$$\mathbf{Q}^t = \mathbf{E}\mathbf{A}(\mathbf{L}_a - \mathbf{L}^t)^{-1} \quad (2.6)$$



Next the residual force  $\mathbf{r}$  is calculated at every node (see Schek [50] for derivation). Note that external force is zero and omitted from the equation.

$$\mathbf{r}^t = -\mathbf{C}^T \mathbf{Q}^t \mathbf{C} \mathbf{x}^t \quad (2.7)$$

Velocity is updated by calculating nodal acceleration, and incorporating viscous and kinetic damping (see Adriaenssens et al. [48] for derivation) with  $\mathbf{A}^D$  and  $\mathbf{B}^D$ . Initial velocity perturbation is incorporated in  $\mathbf{v}^{t=0}$ . Mirrored activated states can be found by changing this perturbation.

$$\mathbf{v}^{t+\Delta t} = \mathbf{A}^D \mathbf{v}^t + \mathbf{B}^D \Delta t \frac{\mathbf{r}^t}{\mathbf{m}} \quad (2.8)$$

Where  $\mathbf{m}$  are the fictitious nodal mass. The node coordinates are updated as follows,

$$\mathbf{x}^{t+\Delta t} = \mathbf{x}^t + \mathbf{v}^{t+\Delta t} \Delta t \quad (2.9)$$

Iteration stops when the total energy of the system approaches a small number  $\xi$ , as this implies that there is no velocity in the system and that none of the springs are stressed.

$$\sum_{k=1}^{m_e} \left( \frac{m_k}{2} v_k^2 + \frac{E_{k,k} A_{k,k}}{2 L_{k,k}} (L_{0k,k} - L_{k,k})^2 \right) \leq \xi \quad (2.10)$$

## 2.4 RESULTS AND DISCUSSION

### 2.4.1 Characterization of the Printed Materials

From the exhibited behavior (Fig. 2.8), the two dominating materials of the mixing process, TB+ and VW+ can be distinguished. Qualitatively, materials printed with TB+ as the base have a large strain, whereas specimens printed with VW+ as the base exhibits necking and fail subsequently from brittle fracture. From material TB+ to VW+, the strength gradually increases, whereas the fracture strain decreases. In the first group (TB+ to F9895), the fracture strain ranges from 30 % to 174 % and ultimate strength ranges from 0.86 MPa to 10.6 MPa. In the second group (R8530 to VW+), the fracture strain ranges from 8 % to 14 % and ultimate strength ranges from 54 MPa to 69 MPa. In general, the observed properties of the DMs can be grouped around the properties of the two base materials, creating a gap in printable material properties in between.

This bi-modal distribution of the material properties validates the assumption that the mixed materials' properties depend heavily on the base material used. Attention is focused on the TB+ dominating group where the allowable strains are deemed sufficient to accommodate the large deformation induced by the snapping behavior, and the range of allowable stresses are sufficient to deliver the desired activation forces. To simplify the material behavior, each of the 7 TB+ based materials is assumed to be able to be adequately modeled by a multi-linear stress-strain relationship. The elastic Young's Modulus of each material can be calculated by

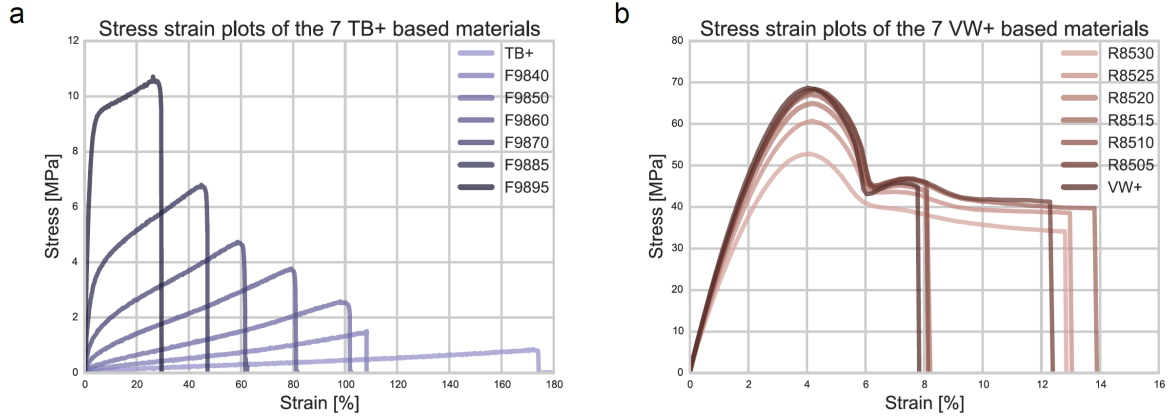


FIGURE 2.8: Experimental result from tensile tests of materials in Fig. 2.1.

dividing the first stress by the first strain of that material. The control points of each of the material are listed in Table 2.3.

Name	$E_{\text{nom}}$ MPa	$\sigma_1$ MPa	$\epsilon_1$ -	$\sigma_2$ MPa	$\epsilon_2$ -	$\sigma_3$ MPa	$\epsilon_3$ -
TB+	0.486	0.850	1.75	-	-	-	-
F9840	1.36	1.50	1.10	1.50	2.00	-	-
F9850	2.65	2.65	1.00	2.65	2.00	-	-
F9860	22.5	0.45	0.02	0.75	0.05	4.0	0.85
F9870	52.5	1.00	0.02	1.60	0.05	4.8	0.60
F9885	125	2.50	0.02	3.75	0.05	7.0	0.45
F9895	375	7.50	0.02	9.50	0.05	10.5	0.26
VW+	2500	50.0	0.02	70.0	0.04	65.0	0.05

TABLE 2.3: Constitutive model of materials TB+ to F9895 and VW+ for physically non-linear analysis

Table 2.3 shows that TB+ can be described by a linear relationship. F9840 and F9850 can be described bi-linearly; the strain value at the first control point of these materials, 200 %, are much higher than that of the stiffer materials. F9860 to F9895 are described tri-linearly, the second strain point is set at 5 % to describe the softening effect and the third strain point is set at rupture. The behavior of VW+ is distinct from the rest as it belongs to the rigid material group and follows the behavior shown in Fig. 2.8B. These values are incorporated in the non-linear Finite Element Analysis (FEA) of the mechanisms.

#### 2.4.2 Mechanical Characterization of the Bistable Mechanism

A subset of the 42 specimens are shown to assess the mechanism's overall behavior. This subset of 12 expands from the benchmark model and includes all specimens with  $l = 0.75$  mm or is fabricated with F9860. Fig. 2.9 A,B,C show that bistable snap-through behavior is observed with all specimens. Regarding the overall behavior, simulations show excellent agreement with



the experimental results with joint material F9860 at all joint lengths  $l = 1.0, 0.75, 0.50$  mm (Fig. 2.9C), differing by  $\text{RMSD} = (0.156, 0.115, 0.121)$  for the retracted configuration and  $\text{RMSD} = (0.402, 0.425, 0.249)$  for the extended. Simulation marginally overestimates the strength with stiffer joints and underestimates the strength with more flexible joints. Qualitatively, the increase in material stiffness translates to increase in mechanism stiffness.

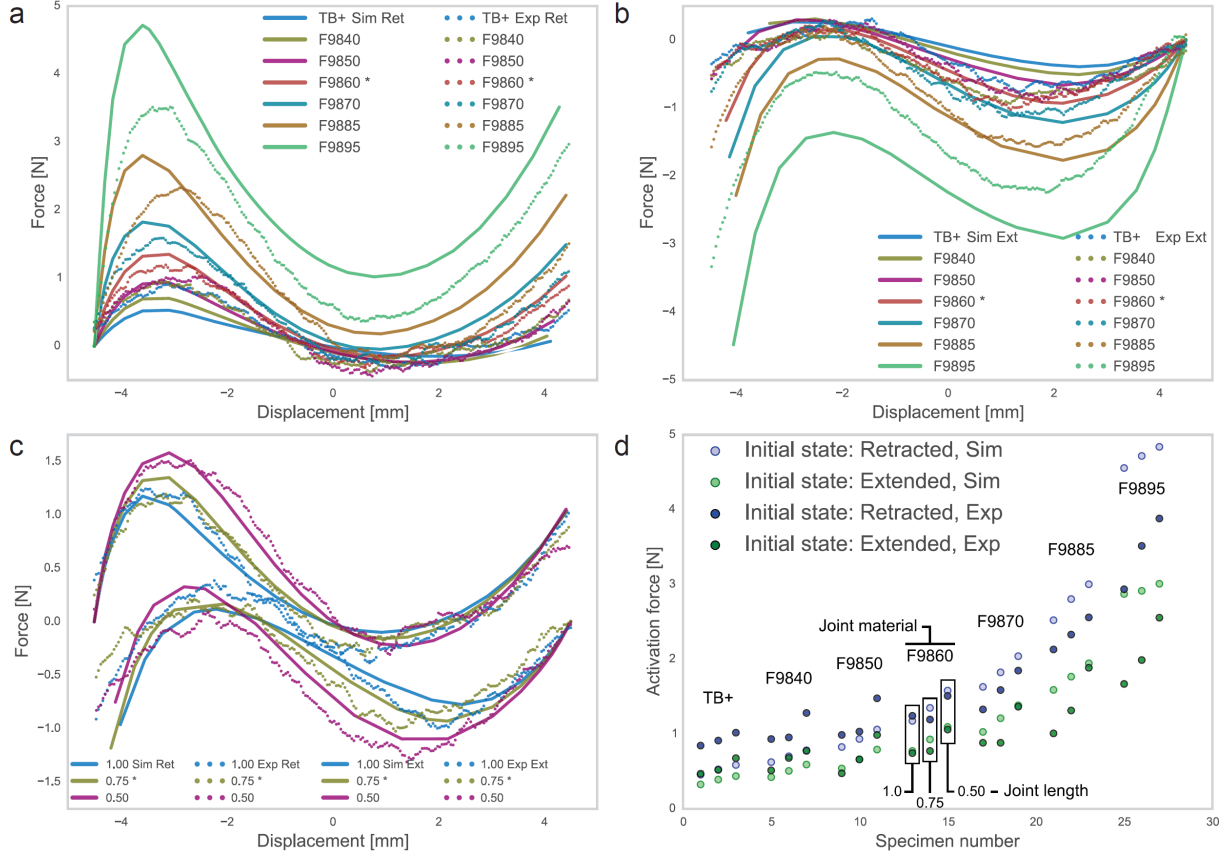


FIGURE 2.9: Simulation and experimental force-displacement graphs. (a, b) includes specimens with fixed joint length but varying material. This shows that 1) an increase in joint stiffness increases the activation force, 2) simulation shows agreement with experimental data, and 3) the extended initial configuration attains lower activation force than the retracted initial configuration. c) includes specimens with fixed joint material stiffness but varying joint length and shows that a decrease in joint length increases the activation force. d) shows the critical force attained by each specimen (see SI.Table 3 to identify the specimens). \* denotes the benchmark configuration.

Increase in activation force is observed with an increase in joint stiffness printed in both retracted and extended configurations. The activation force also increases with a decrease in joint length (Fig. 2.9 D). Both observations agree with the expected behavior. With the specimens printed in the retracted configuration, an activation force ranging from 0.50 N to 5.0 N can be achieved. With the specimens printed in the extended configuration, the activation force range is 0.25 to 3.5 N.

The resulting force-displacement behavior is not symmetrical about  $w = 0$  or path independent (i.e. differences between the retracted and extended initial configuration are observed). This shows that  $k_1$  in Fig. 2.2B is finite and  $k_\theta$  is not zero. Further  $k_1$  of the upper VMT is less than that of the lower. This is expected as the bracket is more flexible further away from the

base support. Similar behaviors are presented in literature. [28] [17] One significant outcome of asymmetry is that the deployed equilibrium state does not reach full stroke length. The same observations can be made with the remaining 24 specimens.

By showing that this bistable mechanism has two equilibrium states and assuming that it can be activated within a global structure, the resulting geometry is guaranteed to be independent of the activation force. Therefore, one can start integrating the proposed mechanism in structures geometrically first and then consider the activation aspect. Similarly, if a different stroke length is desired, one only needs to adjust the inclination angle  $\alpha$  of the truss members. To enable a serial connection between mechanisms, the bracket is designed to be identical to the pin. In this way, the “wasted-length” between the bottom of the pin and of the bracket is eliminated. Parallel connection is enabled by connecting the bracket and the pin of two or more units.

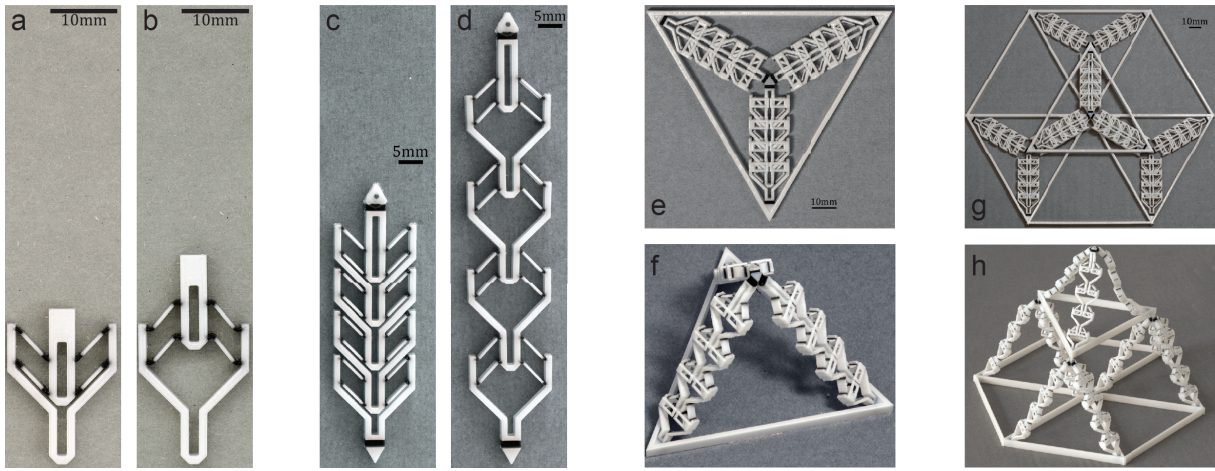


FIGURE 2.10: Results of the space frame structures showing both the fabricated and the activated configurations starting with (a,b) a single mechanism, to (c, d) serially connected mechanisms to extend stroke length, to (e, f) parallel connection to form a tetrahedron, to (g, h) spatial tiling of tetrahedrons.

#### 2.4.3 Hierarchical Structures

All specimens shown in Fig. 2.10 are fabricated flat and use minimal support material. As shown in Fig. 2.10c, the four mechanisms connected in series activate predictably with a tensile point load at the top. With zero post-processing, one is able to activate both the module and the tessellation of modules with an upward force at the apex (Fig. 2.10e,f,g,h).

As shown in Fig. 2.10d, post deployment, each actuated member lengthens from  $b = 54.85$  mm to  $c = 95.00$  mm. The measured lengths are 55 mm (Error: 0.27 %) and 90.5 mm (Error: 4.8 %) for  $b$  and  $c$  respectively. The error in  $b$  is negligible as the printer has a resolution of  $\pm 0.22$  mm in the X-Y plane. The tetrahedral module is designed to attain an apex height of  $h = c\sqrt{6}/3 = 77.57$  mm, where the measured height is 72.0 mm (E: 7.4 %). The overall height of the tetrahedron tessellation is 155.0 mm and is measured as 142.5 mm (E: 8.4 %).

## 2.5 CONCLUSION

With this simple example, the principle of 3D printed, hierarchical deployable structures is demonstrated. It is shown that serial connection extends the total stroke length without increasing the activation force, whereas parallel connection increases the activation force without changing the stroke length. As the activated geometry is an equilibrium state, its geometry is easily predictable. This is of significant importance as precise deployment is mandatory in many applications. Since the initial configuration has no theoretical thickness, deployability is quantified as an expansion ratio  $e_r$  between the activated height,  $h$ , and the side length,  $c$ . This ratio is predefined for a regular tetrahedron and is equal to  $\sqrt{6}/3 = 81.6\%$ . The error in activated geometry is due to the asymmetrical force displacement curve of the mechanism, leading the deployed equilibrium to not attain full stroke length. This error accumulates as more mechanisms are stacked in series.

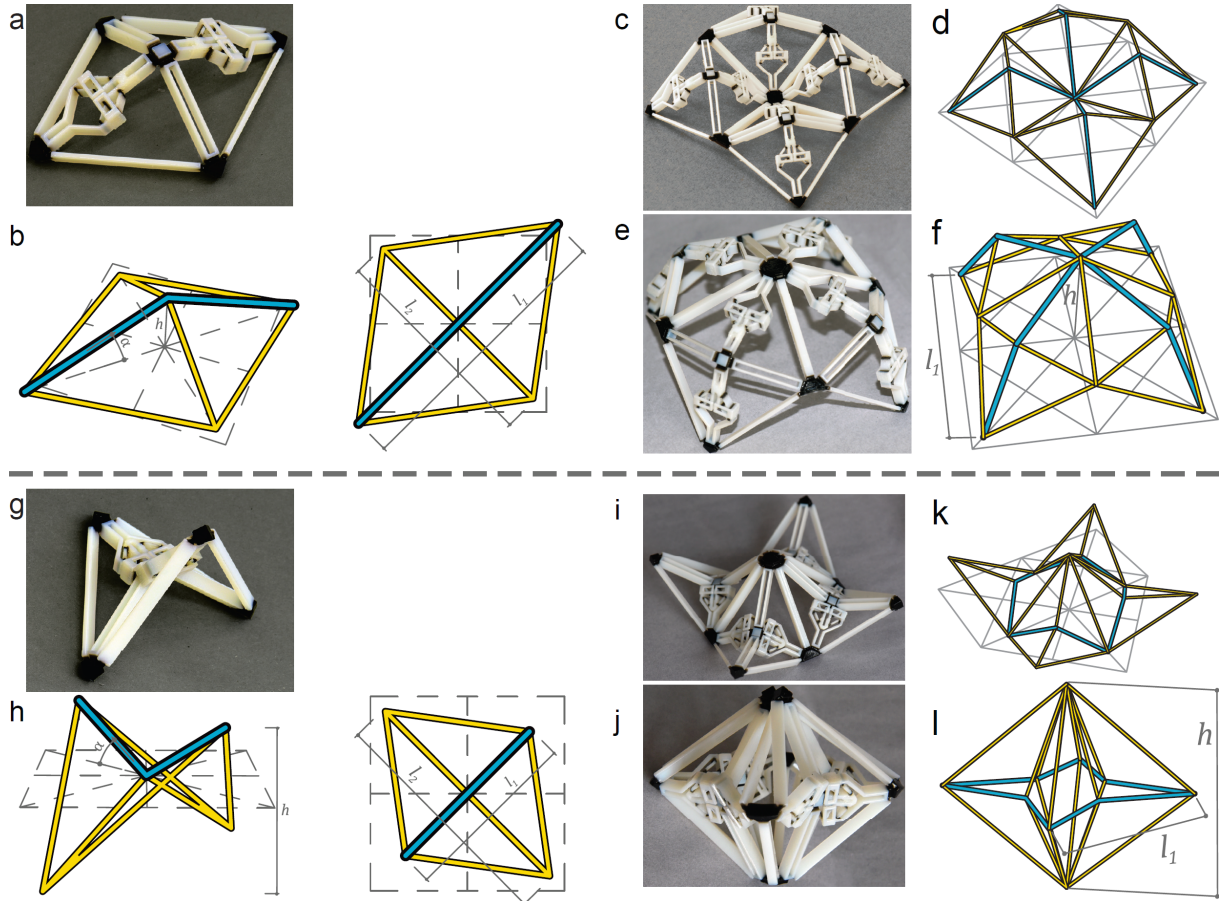


FIGURE 2.11: Results of the grid-based structures. First the activated state A unit module consisting of two mechanisms in either the a) retracted or the f) extended configuration (50 by 50 mm). b, g) shows the initial simulation configuration. c, h) is the activated state of a, f), resulting in a positively or negatively curved surface respectively. d, i, e, j) shows the simulation results in plan and isometric views, with geometrical parameters defined.

Both the unit modules and the grid structures are activated through sequential mechanical activation of the mechanisms. No self-stress is developed after each mechanism activation,

which in itself is an equilibrium state. Intermediate states are omitted and the structures are presented after all bistable mechanisms are activated.

Evaluating the physical specimens, with the square unit modules, by switching the initial configuration of the mechanisms, the activated geometry becomes either positively or negatively curved (Fig. 2.11c, h).

Tiling of the unit modules (Fig. 2.11a) results in a structure with two non-mirrored activated states (Fig. 2.7a-f). It is noted that one activated configuration (Fig. 2.7b, e) reassembles the tiling of the activated state of multiple square unit modules (Fig. 2.11c). However, in Fig. 2.7c,f, one observes the hierarchical behavior where each unit module forms a part of a larger structure which in this case reassembles a dome. Tiling of the unit modules (Fig. 2.11f) results a structure shown in Fig. 2.7g-l). The first activated configuration can also be assembled using individually activated unit modules (Fig. 2.7h,k) and the geometry is similar to large span concrete hyper roofs. Global behavior is observed in Fig. 2.7i,l. The four unit modules fold inward to form an enclosed volume.

With the mDR simulation, the equilibrium states are found when the total energy drops below  $\xi = 10^{-13}$  (Fig. 2.7d-f and j-l). This is achieved for each structure in under 1000 iterations. As shown in Table 2.4, mDR predicts the nodal coordinates within  $\pm 5\%$  of all the following physical specimens.

	Unit Module (Fig. 2.11D,I)						Grid Conf. (Fig. 2.11D,H)					
	Retracted			Extended			A			D		
	PS	mDR	%	PS	mDR	%	PS	mDR	%	PS	mDR	%
$l_1$	80.5	80.1	0.50	50.0	49.0	2.02	88.5	90.1	1.79	55.0	54.4	1.10
$l_2$	64.0	64.7	1.09	64.0	63.5	0.78	-	-	-	-	-	-
$h$	16.5	16.7	1.20	30.5	29.9	1.99	48.0	49.8	3.68	62.0	63.9	3.02

TABLE 2.4: Geometric comparison between physical specimens (PS) and modified Dynamic Relaxation (mDR) results in mm

Complex state change is achieved using simple hierarchical designs. By iterating through all  $S = 2^n$  combinations of bistable states, one is able to obtain all unique activated states using the mDR. Additional states can be found in the case of 2D to 3D deployment by changing the initial velocity based perturbation. These states result from mirroring of the unit modules.

Qualitatively, one observes that the activated states attain structural rigidity with increase in curvature, this can be seen in the SI.Movies. With the dome, by adjusting the stroke length of the bistable mechanisms, its radius can be tailored. If covered with a stretchable fabric, an enclosure is created. With the rhombus-like enclosure, adjustment in stroke length determines the degree of upward rotation, therefore how many unit modules are needed to enclose the space and consequently the interior volume.

The triangular modules in the previous example and square unit modules in this section can be printed individually and connected together post-fabrication in the varying configurations shown. In the activated state, the structure can be treated as a static one, in contrast with



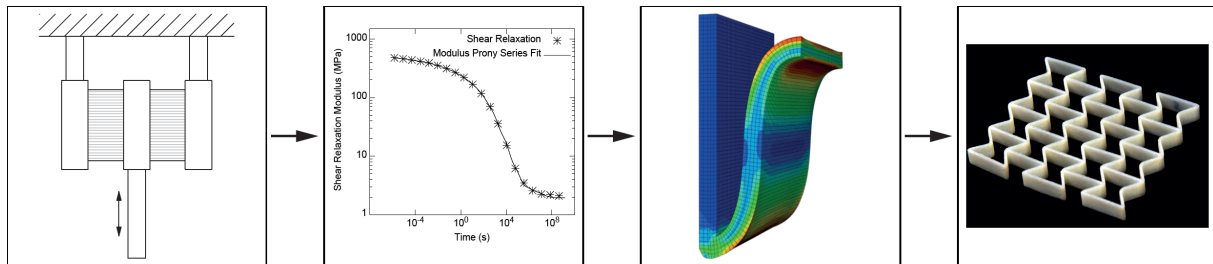
the assumed large deformation of tensegrity-like concepts. [51] They can be activated and deactivated without loss in quality, thereby making the designs reversible. Measured geometries and simulation show adequate similarity, allowing for predictable deployment. The errors are attributed to the discrepancies between the physical joints and idealized pinned connections, and the effect of self-weight.

The design and verification of 3D printed, hierarchical deployable structures is presented. Activation is achieved using hierarchical design principles where a bistable, monolithically printed Von Mises Truss based bistable mechanism acts as the basic building block. The stroke length for the bistable mechanism is maximized. Each design has a flat initial configuration and is printed with a multi-material 3D printer. By varying the joint material and length of the bistable mechanism, numerical simulation and experimentation show that the required activation force can be adjusted.

Two groups of hierarchical deployable structures are presented as proof-of-concept designs. The first is a deployable space frame structure where each tetrahedral module is activated from a flat triangle. The second shows the tiling of different square unit modules in a grid to achieve complex, 3D activated structures of varying Gaussian curvature. The deployed states are found with a modified Dynamic Relaxation method. All demonstrated structures have defined load bearing capacity and predictable activated geometry and are reversible and re-configurable. Future work includes developing computational design methods to explore the design space and optimize active structures.



## SHAPE MEMORY EFFECT AND 3D PRINTING



The content of this chapter was a result of a joint effort between a master student whom I supervised and myself. It has been previously published in *3D Printing and Additive Manufacturing*,

Wagner, M., Chen, T. & Shea, K. (2017). Large Shape Transforming 4D Auxetic Structures. *3D Printing and Additive Manufacturing*, 4(3), 133–142.

### 3.1 SUMMARY

Programmable matter is material that is able to autonomously transform its physical properties in a designed manner. The timing of transformation itself is also able to be encoded into the material, thus achieving autonomous sensing. Conventional manufacturing of programmable matter is restricted in geometric and material complexity. The recent advancement in 3D printing of such matters is a rapidly growing research area over the past decade. Numerous works have shown potential to both revolutionize the field of 3D printing and autonomous reconfiguration. The connection between programmable matter and 3D printing was first made by Tibbitts [52], where an artificial hydrogel was printed adjacent to a compliant passive sheet. When exposed to water, this hydrogel swells and consequently changes the shape of the sheet. The combination of programmable matter and 3D printing is termed 4D printing, where the fourth dimension refers to the stimuli dependent transformation.

Shape-memory polymers (SMPs) are a type of polymeric programmable matter that “remembers” its original shape. After being deformed, it is able to return to its original shape when exposed to a certain stimulus, e.g. temperature change. It was discovered that some polymers fabricated with 3D printers using the photo-polymerization technique exhibit this behavior. [53] This chapter, details the fundamentals of 3D printed SMPs by demonstrating geometric transformation of active auxetic meta-materials that are capable of achieving area changes up to 200%. Active meta-materials belong to a class of programmable matter that

is constructed through period tiling of an underlying structure that is able to undergo autonomous transformation. First, the background and theory of SMPs are described. Then, a viscoelastic model of the 3D printed SMPs is built using thermomechanical testing. Excellent correlation is found between Finite Element simulation using this material model and experimental data from a 3-point bending test. A reduced-beam model is built to simulate rectilinear tiling of the auxetic meta-materials with great accuracy. The characterization process is first performed for one material, and then repeated for some of the other materials available to the same 3D printing process for later studies.

### 3.2 BACKGROUND

Rapid advancement in 3D printing technologies has led to improvements in part quality, achievable resolution and printable materials. Recent studies present approaches in which enormous design freedom is combined with active materials for the fabrication of shape transforming systems. Active materials are capable of changing their properties or shape as a response to an external stimulus. When incorporated in mechanical systems, these materials allow controllable self-activation without external mechanical input. Fabrication of programmable matter using 3D printing technologies allows for much more complex designs than what is feasible with conventional manufacturing. 3D printing using active materials has been termed 4D printing [52] where time is the fourth dimension and structural variations are programmed to respond to external stimuli like temperature and humidity, i.e. swelling.

4D printing has large untapped potential in applications where configuration change cannot be manually achieved and where electro-mechanical actuation is not feasible, e.g. in aerospace [54] and in medical fields [55]. In these applications, 4D designs have the additional advantage of volume and support structure reduction [3]. Most studies on 3D printing of active materials use stimuli-responsive shape changing polymers. These polymers can be divided into two subclasses, the programmable Shape Memory Polymers (SMPs) [5, 13, 56–58] and the artificial hydrogels [4, 58, 59]. The mechanism of shape change for these two types of polymers differs greatly. SMPs are deformed externally at high temperatures and stay in the deformed configuration if they are cooled below the actuation temperature, which is also referred to as programming. Upon heating, actuation takes place and the original shape is recovered [60].

Ge et al. [53] proposed Printed Active Composites (PACs) fabricated from multi-material 3D printing. The PACs consist of a rubbery matrix reinforced by fibers made from SMP. They are printed flat and evolve into three-dimensional shapes upon programming. By introduction of several SMPs with multiple actuation temperatures Mao et al. [13] designed 3D printed strips that exhibit controllable sequential shape changes.

Following this approach, Wu et al. [56] developed PACs exhibiting two temperature dependent active shape changes by using two tailored polymers. Ge et al. [57] used projection micro-Stereolithography for multi-material printing of SMPs. This allows the manufacturing of parts with higher resolution and without support material. This represents an extension to



most of the other studies using Inkjet printing for manufacturing of SMP based programmable matter.

Artificial hydrogels react to fluids in their environment by swelling. The shape change of hydrogels proceeds as long as the stimulus is applied. In a dry environment, the permanent shape is slowly recovered as the absorbed fluid evaporates [60]. Raviv et al. [4] showed that 3D printing of hydrogels in combination with flexible polymers can be used to design active systems that self-deploy when submerged in water. Different actuation principles such as linear extension and bending were proposed. Gladman et al. [59] used 3D printed hydrogels reinforced by aligned cellulose fibrils to generate anisotropic swelling behavior of the printed strands. Different activated shapes were achieved by changing the strand orientation.

By combination of swelling hydrogels with SMPs, Mao et al. [13] developed novel materials that can reversibly change their shape when subjected to a hydro-thermal-cycle. The swollen hydrogel was used to program the SMPs. The SMP is fixed through cooling to the programmed shape. Upon heating to the SMP's actuation temperature, the permanent shape is recovered.

Compared to hydrogels, SMPs have the advantage that they exhibit a clearly defined shape change. In contrast, hydrogels will continue swelling as long as the stimulus is applied until saturation. Shape change occurs at a much faster rate, several seconds, with SMPs compared to several minutes up to hours for hydrogels. The major drawback of SMPs is that they require manual programming. This process is often imprecise and causes failure in designs. In addition, the achievable shape change of PACs is limited to bending. Presently, fabrication of SMP and hydrogel designs require multi-material 3D printing. This functionality is currently still limited to a few expensive machines.

These challenges are addressed by introducing SMP-based shape transforming auxetic meta-materials. The versatility of the proposed meta-materials enable the tiled sheets to be programmed into multiple shapes. These tiled sheets are programmed with greater accuracy, allowing both the relaxed and the programmed states to be precisely defined. The resulting shape exhibit much larger multi-dimensional transformation than previous publications. With the performed material characterization and resulting constitutive models, a simplified procedure is proposed to simulate the relaxation behavior with accuracy.

To simplify the fabrication process, the proposed meta-materials consist of a single material. They can be fabricated with inexpensive Inkjet printing processes using commercially available materials. This also broadens the potential for prototyping 4D designs for a variety of applications.

The proposed auxetic meta-materials exhibit a carefully designed micro-structure to enable negative Poisson's ratio and a tunable stiffness [61]. Designs with a negative Poisson's ratio have the advantage that when force or displacement is applied in one direction, the other dimensions will follow with similar deformation. This is especially useful for SMP based meta-materials since shape programming can be challenging if forces need to be applied consistently in all dimensions.

To simulate the proposed designs, first the thermomechanical behavior of the underlying SMP is characterized. The resulting data is fitted to a linear viscoelastic model. This model is implemented in a detailed finite-element simulation of the smallest component of the designs. To efficiently model systems consisting of a large number of active elements, a reduced beam element is constructed to emulate the same mechanical behavior. The computational effort is reduced while predicted forces and displacements remain accurate.

### 3.3 METHOD AND DESIGN

The goal of this study is the exploration of 3d printed active materials and the design of shape transforming meta-materials. The study is conducted following the procedure in Figure 3.1. First, the thermo-mechanical properties of the 3D printed polymer is characterized. A linear viscoelastic constitutive model is then constructed using the experimental data. The simulation model is validated by experiments with a three-point bending test. Following this, the chapter presents the design, simulation, fabrication and test of the shape transforming active meta-materials.

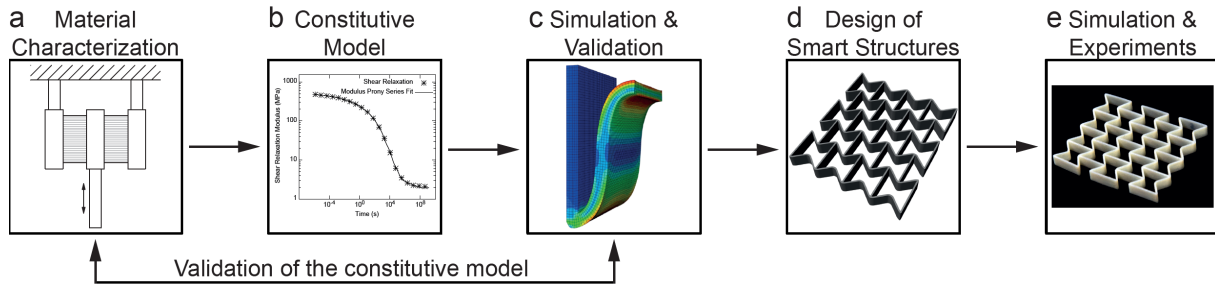


FIGURE 3.1: Method procedure. a) Experimental material characterization. b) Constitutive model. c) Finite-element simulation and validation by comparison to experiments. d) Design of active auxetics. e) Design Simulation by reduced modeling approach and testing.

The shape memory cycle of the meta-materials is modeled using finite-element simulations. With this force-displacement data from the simulation, an artificial stiffness of beam elements is fitted such that they exhibit the same mechanical behavior. The reduced beam modeling approach allows the simulation of geometrically complex shapes with low computational expense.

#### 3.3.1 Materials and Fabrication

The active meta-materials are parametrically modeled and fabricated with a multi-material Inkjet 3D printer (Objet 500 Connex3, Stratasys). In this process, liquid polymer is jetted in thin layers and cured with UV light to fabricate geometrically complex designs. A soluble support material is used which allows the manufacturing of fragile geometries. The active components of the designs are fabricated using the shape memory properties of VeroWhitePlus RGD835

(VW+), which is the same material that can be used on the most inexpensive, single material Inkjet printers.

### 3.3.2 Thermomechanical Characterization

The parameters required to model the thermomechanical behavior are obtained by experimental characterization. Four sets of material related parameters are necessary, 1) the glass transition temperature  $T_g$ , 2) the fully relaxed modulus, 3) the coefficient of thermal expansion (CTE) and 4) frequency sweeps of the storage modulus at different temperatures.

A Dynamic Mechanical Analysis (DMA) (Mettler Toledo DMA 861) is used to measure  $T_g$  of the polymer. For amorphous SMP, the  $T_g$  is the actuation temperature. In the experiment, the temperature is increased from  $-20^\circ\text{C}$  to  $120^\circ\text{C}$  with a rate of  $1^\circ\text{C min}^{-1}$ . A shear setup with cylindrical specimen ( $\varnothing = 4\text{ mm}$ ,  $h = 2\text{ mm}$ ) is used. The tests are performed by applying a sinusoidal displacement with a frequency of 3 Hz and an amplitude of  $0.5\text{ }\mu\text{m}$ .

The fully relaxed equilibrium modulus of VW+ is measured in a compression experiment using a Zwick Zo20 universal testing machine equipped with a 2 kN load cell and a temperature chamber. To obtain the relaxed modulus, the experiment is performed at  $80^\circ\text{C}$  with a rate of  $5\text{ mm min}^{-1}$ . Cylindrical specimens ( $\varnothing = 7\text{ mm}$ ,  $h = 9\text{ mm}$ ) are used.

VW+'s coefficient of thermal expansion (CTE) is measured using a Perkin Elmer DMA 7e. A cylindrical specimen ( $\varnothing = 7\text{ mm}$ ,  $h = 10\text{ mm}$ ) is heated from 0 to  $80^\circ\text{C}$  with a rate of  $1\text{ mm min}^{-1}$  and the thermal strain is measured.

The DMA is used to measure the storage modulus and  $\tan(\delta)$  vs frequency at different constant temperatures. A shear setup and cuboid specimen with the dimensions  $3.00 \times 4.30 \times 2.05\text{ mm}$  are used. Displacement frequency is swept from 100 Hz to 0.01 Hz with an amplitude of  $0.5\text{ }\mu\text{m}$ . This procedure is repeated at  $20^\circ\text{C}$ ,  $40^\circ\text{C}$ ,  $50^\circ\text{C}$ ,  $60^\circ\text{C}$ ,  $80^\circ\text{C}$  and  $100^\circ\text{C}$ .

### 3.3.3 Linear Viscoelastic Constitutive Theory

Time temperature superposition principle is applied to the measured shear storage modulus to obtain a continuous master curve using shift factors. The shift factors are approximated by the WLF equation 3.1. [62]

$$\log_{10}(a_T) = \log_{10} \frac{\tau(T)}{\tau(T_0)} = -\frac{C_1(T - T_0)}{C_2 + (T - T_0)} \quad (3.1)$$

The storage modulus master curve can be transformed into the relaxation modulus master curve by means of a Fourier transform (Eq. 3.2). [62] With  $G_\infty$  being the equilibrium modulus and  $G'$  being the storage modulus.

$$G(t) = G_{\infty} + \frac{2}{\pi} \int_0^{\infty} \left[ \frac{G' - G_{\infty}}{\omega} \right] \sin \omega t d\omega \quad (3.2)$$

In this study, the Fourier transform is approximated by Eq. 3.3 according to the approach proposed by Schwarzl. [63]

$$\begin{aligned} G(t) \cong & G'(\omega) + 0.00782[G'(8\omega) - G'(4\omega)] \\ & - 0.09990[G'(4\omega) - G'(2\omega)] \\ & + 0.02000[G'(2\omega) - G'(\omega)] \\ & - 0.21600[G'(\omega) - G'(\frac{\omega}{2})] \\ & - 0.39700[G'(\frac{\omega}{2}) - G'(\frac{\omega}{4})] \\ & - 0.11100[G'(\frac{\omega}{8}) - G'(\frac{\omega}{16})] \\ & - 0.02760[G'(\frac{\omega}{32}) - G'(\frac{\omega}{64})] \\ & - 0.00689[G'(\frac{\omega}{128}) - G'(\frac{\omega}{256})] - \dots \end{aligned} \quad (3.3)$$

Theoretically Eq. 3.3 consists of an infinite number of terms. Each additional term will have the frequency and the coefficient divided by the factor of 4 compared to the predecessor term. In this study 11 terms are used since additional terms have negligible improvement on the accuracy of the approximation. The relaxation modulus is approximated by means of a Prony series (Eq. 3.4).

$$G(t) = G_{\infty} + \sum_{i=1}^N G_i e^{-t/\tau_i} \quad (3.4)$$

In Eq. 3.4  $G_i$  are the stiffness of the non-equilibrium branches and  $\tau_i$  are the relaxation times. For approximation of the experimental data, a Prony series with  $N = 19$  non-equilibrium branches is used.  $G_i$  and  $\tau_i$  are determined by least square fitting.

The behavior at different temperatures is modeled by multiplying the relaxation times of the reference temperature  $T_0$  by shift factors of the corresponding temperature (Eq. 3.5). [62]

$$\tau_i T = \alpha_T \tau_i(T_0) \quad (3.5)$$

### 3.3.4 Implementation of Finite-Element Simulation

For modeling of the shape memory effect of 3D printed polymers, Ge et al. [57] and Mao et al. [58] use finite-element simulations with subroutines to predict the shape changing kinematics as well as the force produced by the SMPs. Bodaghi et al. [64] implemented an anisotropic material model subroutine for finite-element simulations taking the characteristic

layered micro-structure of parts manufactured by additive manufacturing into account. Others use simpler reduced order models to predict the kinematics of the shape changes. [4, 59].

Finite-element simulations allow the accurate modeling of shape changing kinematics and actuation forces. The drawbacks are that the simulations presented so far require the implementation of constitutive models in subroutines. The modeling of complex designs in FEM is computationally expensive. Reduced models on the other hand are not capable of accurately predicting the temperature-dependent recovery kinematics and actuation forces. We aim for modeling the 3D printed SMP using commercially available FEM software.

To model shape memory behavior, the Prony series equation in shear and the WLF equation implemented viscoelastic material model in Abaqus (Dassault Systems) are utilized. [64] In addition, in the fully relaxed state, the elastic behavior and the Poisson's ratio are specified. Nearly incompressible behavior is assumed  $\nu = 0.5$  and  $K(T) = \infty$ . This assumption is valid since all deformations occur at temperatures above the  $T_g$  at which the polymer is in a rubbery state and exhibits a Poisson's ratio close to 0.5. For modeling of the thermal strain, a temperature-dependent expansion coefficient is used. The model consists of C3D8RH hybrid brick elements that allow for simulation of incompressible behavior.

### 3.3.5 Validation of Model Accuracy

To validate the accuracy of the finite-element model, a shape memory cycle in a three point bending experiment is tested on a Perkin Elmer DMA 7e. In the first experiment, a free recovery test is performed and a cuboid specimen with the dimensions  $25 \times 5 \times 1.5$  mm is used. The specimen is held for 5 min at  $80^\circ\text{C}$ . Then the beam is programmed by a suddenly applied programming force of 750 mN. After holding the specimen for 3 min, the temperature is reduced to  $0^\circ\text{C}$  with a rate of  $10^\circ\text{C min}^{-1}$ . Then the specimen is held at  $0^\circ\text{C}$  for 1 min with the programming force applied and for 1 min further after removal of the programming force. The recovery of the original shape is initiated by heating the specimen to  $80^\circ\text{C}$  at a rate of  $20^\circ\text{C min}^{-1}$  and holding at  $80^\circ\text{C}$  for 10 min.

In the second experiment, the constrained recovery is tested. We use a specimen of the dimensions  $25 \times 5 \times 2$  mm and a programming force of 1200 mN. Instead of removing the force in the recovery step, 700 mN are applied to constrain the recovery of the SMP beam. The other experimental parameters are identical to those of the free recovery experiment.

The data from the three point bending experiment is compared to Abaqus simulations of the same experiments using the temperature-dependent viscoelastic material model. The temperature of the experiment measured at the thermocouple is used as input for the specimen temperature in the finite-element simulation.

### 3.3.6 Design of Active Structures

We propose active auxetic meta-materials that can be programmed by large deformations exhibiting a negative Poisson's ratio and recovering their original shape upon external stimulus. The design of the auxetic meta-materials are shown in Figure 3.2a,b,c.

Figure 3.2a depicts a compressible reentrant honeycomb. The geometry is designed to allow area changes of up to 160 %. The reentrant honeycomb in Figure 3.2b can be stretched in the programming step and will shrink in the recovery step. The area can be reduced by 200 %. Figure 3.2c shows a chiral auxetics, which can be compressed through internal rotation and expand its area by 50 % in the recovery step.

To evaluate of the shape transforming capabilities of the meta-materials, they are programmed at 80 °C. The programmed shape is fixed by cooling in a water bath of a temperature of 5 °C. The original shape is recovered by being submerged in 80 °C water.

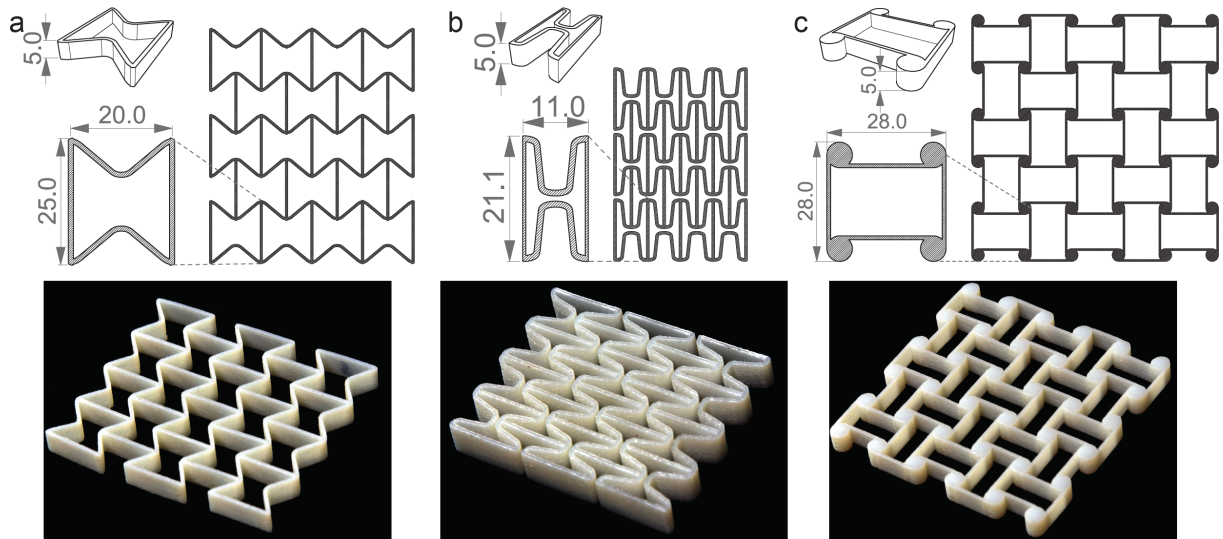


FIGURE 3.2: CAD models of active auxetics: a) reentrant honeycomb expansion [18], b) reentrant honeycomb (shrinkage), c) chiral auxetic. [65] All dimensions are stated in mm.

### 3.3.7 Modeling of Active SMP-based Designs

A reduced simulation approach is proposed for modeling of complex activation. The detailed finite-element simulation using hybrid brick elements and the thermo-viscoelastic material model is performed for the smallest unit of the meta-materials. Using this, applied displacement and the resulting reaction force of both the programming and the recovery step are recorded. A linear stiffness of a fictitious beam element is fitted to the force-displacement data. From these beam elements, complex designs are assembled and simulated with low computational expense.



## 3.4 RESULTS AND DISCUSSION

## 3.4.1 Material Characterization

Figure 3.3a shows the resulting  $\tan(\delta)$  curve of VW+ from the DMA experiment. The peak indicates a  $T_g$  of 60 °C and a wide transition region between approximately 40 and 80 °C. Thus 80 °C is used as the programming temperature and fix the deformation of the SMP by cooling to 5 °C. As shown in Figure 3.3b, a mostly linear relationship between stress and strain can be observed up to a compressive strain of 15 %. The results of the thermal strain measurements are shown in Figure 3.3c. Above the  $T_g$  a CTE of  $2.42 \times 10^{-4} \text{ }^\circ\text{C}^{-1}$  and below the  $T_g$  a CTE of  $1.60 \times 10^{-4} \text{ }^\circ\text{C}^{-1}$  is measured. Figure 3.3d depicts the shear storage modulus data of the frequency sweeps and the master curve constructed from the experimental data using a reference temperature of 40 °C. The transformed shear relaxation master curve and the Prony series fit are shown in Figure 3.3e. It is found that the 19-branch Prony series accurately approximates the experimental data, with a root mean square deviation of 0.528 MPa. The WLF approximation of the shift factors is shown in Figure 3.3f. For temperatures higher than the reference temperature of 40 °C, the shift factors are approximated very accurate. At lower temperatures, overestimation of the shift factors occurs.

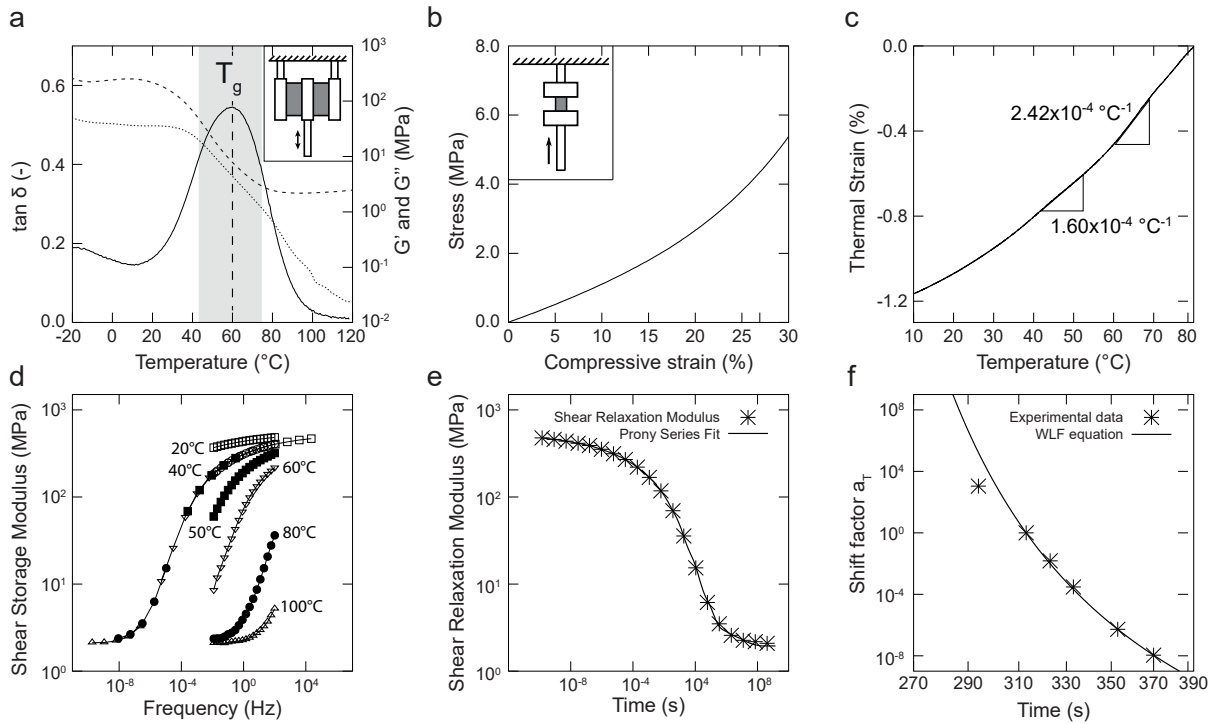


FIGURE 3.3: Thermomechanical material characterization of VW+. a) DMA shear setup, tangent delta over temperature,  $T_g$  approximately at 60 °C (solid line), shear storage modulus (dashed line), shear loss modulus (dotted line), b) Uni-axial compression test at 80 °C, c) Thermal strain experiment, d) Shear storage modulus from DMA frequency sweeps in shear setup and master curve with a reference temperature of 40 °C, e) Transformation to the shear relaxation modulus (dots) and Prony series approximation (solid line), f) Shift factors (dots) and WLF equation (solid line).

### 3.4.2 Validation of Model Accuracy

The results of the comparison between experimental and simulated shape memory cycle with free (a, b) and constrained (c, d) recovery are shown in Figure 3.4. Graphs (a) and (c) show the temperature (dashed line) and force (solid line) of the shape memory cycle. Graphs (b) and (d) compare the resulting beam deflections in the experiment (solid line) and the simulation (dotted line). The time axes are divided into the four steps of the shape memory cycle (step 1: programming, step 2: cooling, step 3: unloading, step 4: recovery).

The programming of the SMP beam is simulated accurately in both experiments. In the cooling step, the experiments show a larger thermal strain than the simulated three point bending beam (arrows in Figure 3.4). There is a slight delay between the experimental and the simulated recovery. Overall, excellent correlation between the experiment and the simulation is found.

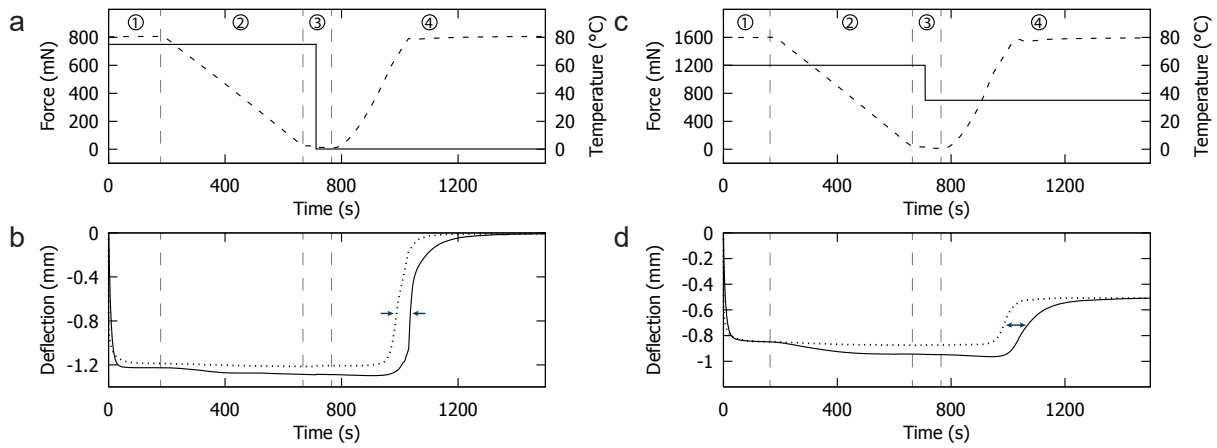


FIGURE 3.4: Comparison between three point bending free (a, b) and constrained (c, d) recovery experiment and simulation. (a, c) solid line force, dashed line temperature. (b, d) solid line experiment, dotted line simulation. Arrows in (b) and (d) indicate the discrepancy between simulation and experiment as a result of heat conduction.

### 3.4.3 Evaluation of Active SMP-based Designs

The shape transformation of the designed active auxetics is evaluated (Figure 3.5). While the rate of shape transformation depends on the temperature in the recovery step, all designs presented recovered their permanent shape in less than ten seconds in the experiments at approximately 80 °C.

Figure 3.5a depicts the shape transformation of the expanding auxetic reentrant honeycomb. An increase in area of more than 150 % is realized. The shape transformation of the shrinking auxetic reentrant honeycomb is shown in Figure 3.5b, with an area reduction of approximately 200 %. Figure 3.5c shows the shape transformation of the chiral auxetics with an area increase of 62 %.



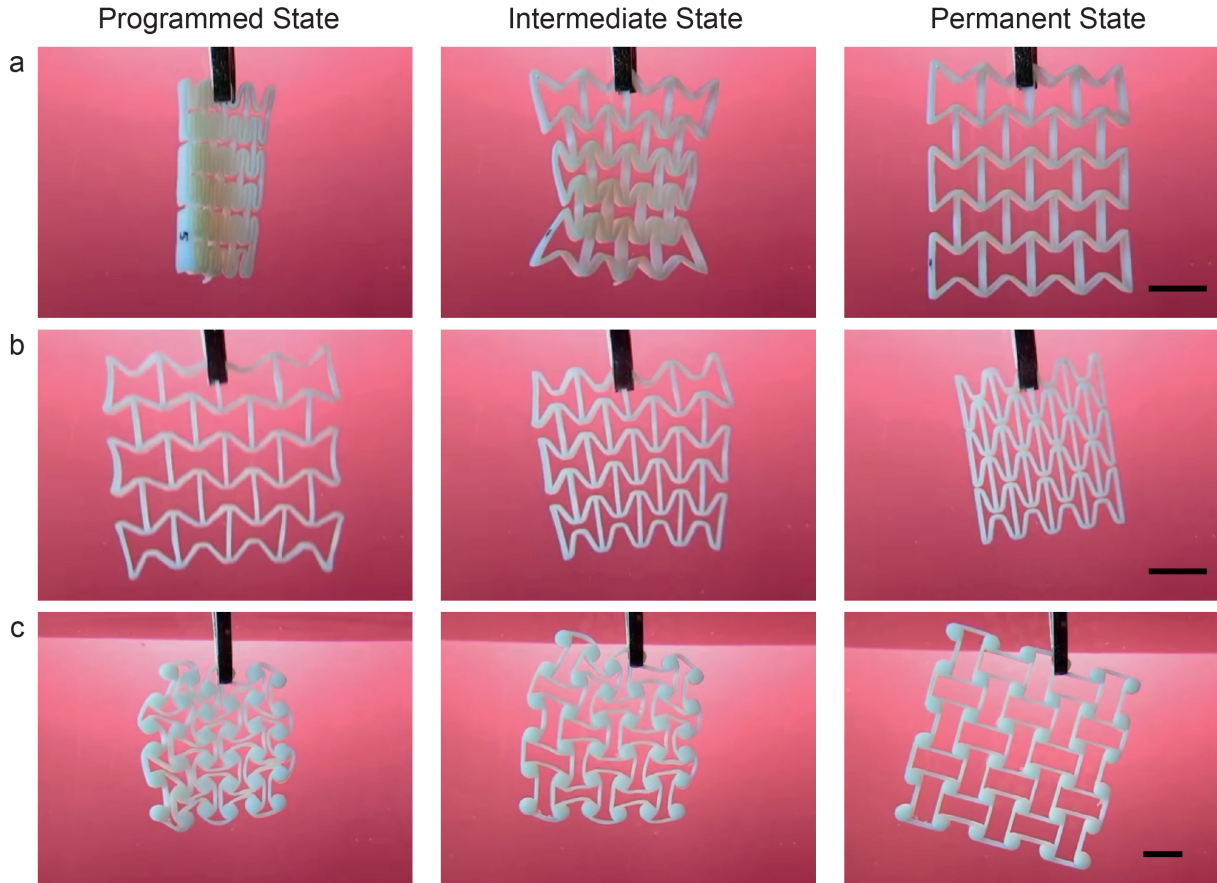


FIGURE 3.5: Shape transformation of active meta-material based polymer sheets. Left column: programmed state, middle column: intermediate state, right column: permanent state. Active auxetics: a) reentrant honeycomb expansion, b) reentrant honeycomb shrinkage, and c) chiral auxetic. Scale bars represent 10mm.

#### 3.4.4 Modeling of Active Auxetics

The modeling approach is illustrated in Figure 3.6. As shown in Figure 3.6a, the complete shape memory cycle using non-linear analysis and the viscoelastic material model is simulated on a brick-based finite-element model of the meta-material. The characteristic curve shown in Figure 3.6b is used to construct a linear stiffness (red line) with the same force displacement behavior. This reduced beam model is used to simulate a simple tiling of the reentrant honeycomb under compression (Figure 3.6c). Using this simplification, the computation time can be reduced from up to 24 hours to several minutes.

### 3.5 CONCLUSION

This chapter presents auxetic meta-materials that undergo large and versatile three-dimensional transformations. This broadens the applications of the existing 3D printed active meta-material based auxetic sheets. Testing of the active auxetics showed that the intended shape transformation is realized.

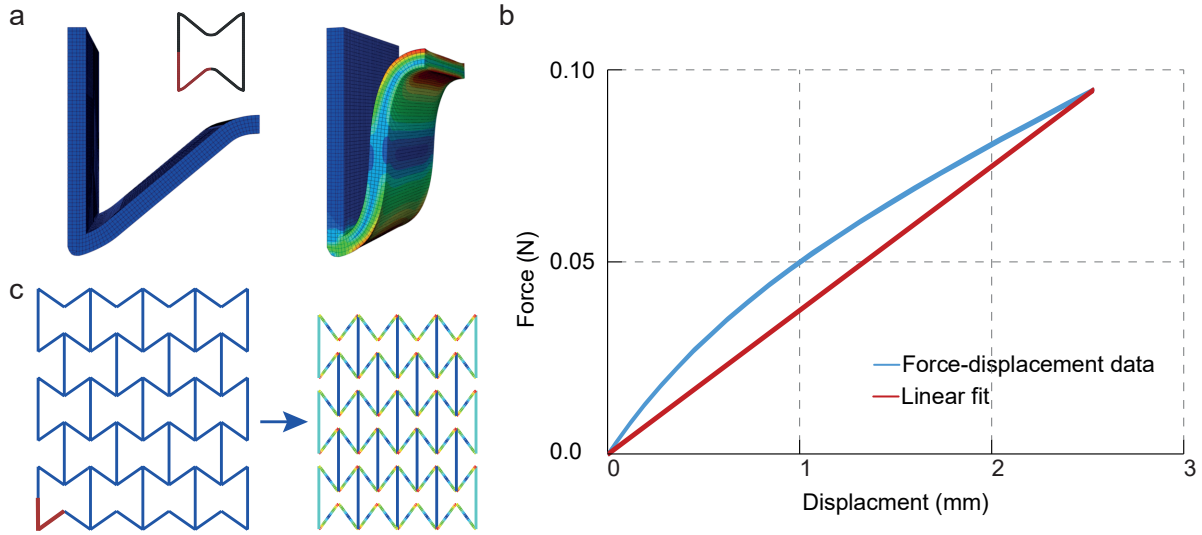


FIGURE 3.6: a) Brick finite-element model of quarter reentrant honeycomb. b) Force-displacement curve. c) Reduced order finite-element model of rectilinear tiling of the reentrant honeycomb.

It is shown that the thermo-viscoelastic equations implemented in Abaqus can be used to model the non-linear time and temperature-dependent shape memory behavior of 3D printed SMPs with excellent accuracy. Compared to other studies [4, 58], the implementation of a material subroutine is not required. This simplifies both material characterization and the FE modeling process as well as allowing the simulation to be performed by a non-expert.

The three-point bending experiments show higher thermal strain in the cooling step than the finite-element simulations. This can be possibly attributed to an entropy elastic behavior of the polymer above the  $T_g$ . With decreasing temperature, the modulus decreases, leading to increasing beam deflection. The delay between simulated and experimental recovery (arrows in Figure 3.4b and d) occurs due to heat conduction, i.e. time is required for the temperature measured at the thermo-couple to reach inside the specimen. In simulation, no heat conduction is taken into account and the temperature measured at the thermo-couple is directly used as input. This hypothesis is underlined by the fact that this effect is more pronounced in the constrained experiment in which a specimen with a higher thickness is used. Additionally the accuracy can be improved by accounting for the anisotropic properties of 3D printed parts.

Efficient numerical simulation models are developed to correctly predict the mechanical properties of complex designs during programming and recovery. The efficient reduced beam simulation model is able to simulate the complex designs composed with the proposed meta-materials. The advantages, physical accuracy of volume FE models, can be combined with the low computational expense of models like spring mass representations. However, since the behavior of activation and shape transformation is non-linear and thus an accurate prediction is only reached if the deformations in the reduced beam model does not differ too greatly from the deformations in the finite-element simulation of the brick model.

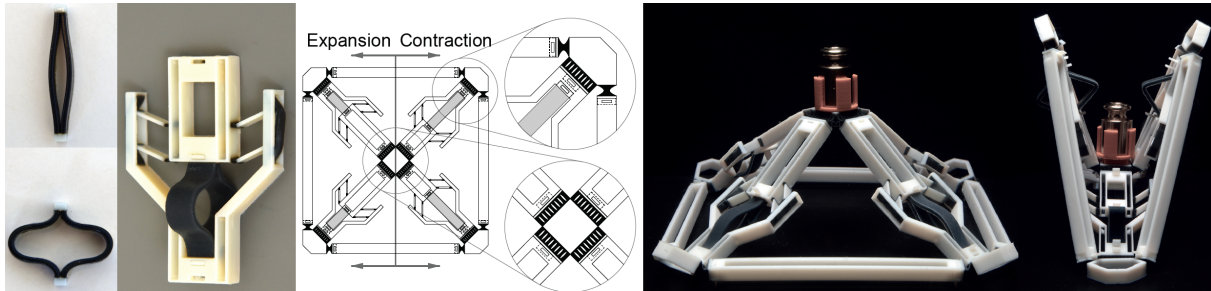
The active auxetics developed in this work undergo large shape transformation. This invariably leads to changes in mechanical properties such as stiffness, [61] Poisson's ratio, vibration

damping and energy absorption. This will be exploited in future studies to design mechanical systems that are capable of adapting their properties to their environment in a controlled manner.

A 3D printed shape memory polymer is used to fabricate active meta-materials. The meta-materials proposed can achieve area changes of up to 200 % within a programming and relaxation cycle. This property is inherited in complex designs that are formed with these meta-materials. These designs can be programmed into versatile shapes and recover their original form when subjected to heat. For simulation of the meta-materials, a viscoelastic constitutive model with data from thermo-viscoelastic material characterization experiments is constructed. The accuracy of the model is shown with a three-point bending test. To reduce computational effort, a reduced beam model is constructed to predict forces and deformations of complex active SMP based designs. Rectilinear tiling of the proposed meta-materials achieve the desired shape transformation. Simulation results confirm this behavior.



## AUTONOMOUS DEPLOYMENT OF STRUCTURES



The content of this chapter has been previously published in *3D Printing and Additive Manufacturing*,

Chen T. & Shea K., (2018), An Autonomous Programmable Actuator and Shape Reconfigurable Structures using Bistability and Shape Memory Polymers, *3D Printing and Additive Manufacturing*, 5(2), 91-101.

#### 4.1 SUMMARY

Thus far, the thesis have discussed the fundamentals of Shape Memory Polymers (SMPs) as well as the potential engineering applications of SMPs. Through SMPs, one is able to change both the geometrical shape as well as the function of an engineering system. The previous chapter has shown the potential for bistable mechanisms to deploy a structural system from a flat to a 3D state. Since each bistable mechanism has two equilibrium states, external work is only needed for state transformation, but not to maintain such a state.

Both SMPs and bistable mechanisms have some features that are missing when used in an engineering system. Through the use of SMPs alone, a system must be fabricated in the permanent state, manually programmed and reverts to the permanent state upon activation. Further, an SMP based system is not mechanically stiff under a high temperature environment since the SMPs are themselves in a rubbery state. Bistable mechanisms on the other hand, still need a mechanical force input for state transformation.

This and the following chapter explore the possibilities offered by combining the Shape Memory Effect and mechanical instability. Since the bistable mechanism is fabricated using materials that have either a much higher or lower activation temperature, it's mechanical behavior is not temperature dependent and remains stiff under a heated environment. On the

other hand, the autonomous triggering of the bistable mechanisms are enabled through the use of embedded SMPs.

In this chapter, I demonstrate the autonomous deployment of load-bearing structures. The structures are fabricated flat and autonomously deploy into their permanent 3D shapes that are load bearing under both the activation temperature and the operating temperature.

## 4.2 BACKGROUND

Deployable structures are used in a wide range of applications in space exploration, [66] biomedical, [67] and solar energy. [68] In these applications, the properties of the deployable structures typically sought include large-scale and predictable geometric reconfigurations, passively controllable activation, load bearing capability and tunable deployment conditions. In addition to motorized actuators, a number of passively actuated designs have been proposed, including electricity, [69] light, [70] pressure, [71] shape memory effect (SME), [5] swelling, [52] and piezoelectricity. [72]

In the aerospace field, deployment is a critical phase in the life cycle of a space structure. [73] With respect to kinematics, entanglement and jamming may occur if part movements cannot be precisely controlled. [74] Mechanically, the driving force must be tuned to overcome resistance at all stages of deployment. [75] Traditionally, designs often involve complex packing strategies, such as origami folding, [76] tensegrity, [77] as well as bulky powered driving mechanisms such as air pressure [78] and electrical drives. [79] With multi-material 3D printing technologies, there is potential to fabricate monolithic designs that can be autonomously activated by environmental triggers, e.g. temperature.

An increasing number of active structures are designed and fabricated in the newly coined field of 4D printing. [52] 4D printing uses properties of 3D printing materials to achieve design shape change under environmental forces. The development has been focused in the areas of material synthesis and geometric reconfiguration. In Raviv et al., [4] a hydrogel that swells under water is used as an actuator that changes the shape of a compliant string or surface. Gladman et al. [59] continued this method of actuation by designing anisotropic properties of a swelling meta-material. Ge et al. [57] first utilized the shape memory properties of the photo polymeric inks used in the Polyjet 3D printing technology to achieve shape change.

Each of these actuation methods have areas for improvement. Swelling hydrogel has a long activation time, imprecise geometric configuration change and lack of load bearing capacity. Additionally, it is often impractical to submerge a structure under water. Shape memory polymers, as implemented by Ge et al., [57] require the design to be fabricated in the activated state, while offering no real precision in the programmed state.

SME of polymers is adopted in this research as the activation material as it is able to produce a large actuation strain [80] and moderate recovery stress. While the shape memory effect is observed with most thermosets, it is not feasible for traditional fabrication methods to produce complex parts with multiple materials. In this work, the multi-material Inkjet technology is

exploited to fabricate complex designs by selectively depositing photo-reactive liquid resins of different stiffness and glass transition temperature. Currently there is no other means of fabrication to do this.

By combining this polymer with a bistable mechanism called the Von Mises Truss, I am able to define two distinct equilibrium states that can be precisely achieved. Von Mises type bistable mechanisms have previously been used in active masts, [28] for energy absorption, [17] and more recently to create 3D printed reconfigurable structures. [3]

In the activation phase, the bistable mechanism acts as a force amplifier, and renders the deployable structure load bearing. By combining the mechanics of bistability and shape memory polymers, I present a unit actuator that delivers the above characteristics and addresses the shortcomings. I propose to integrate this actuator in deployable structures as the source of activation for shape reconfiguration. The structures can be deployed from 2D to 3D states when temperature reaches a threshold. By presenting a synclastic and an anticlastic structure reconfigured from the same base design, I demonstrate both autonomous deployment and shape reconfiguration.

While it is possible to control individual shape memory elements through Joule heating, one of the aims of this work is to eliminate on-board electrical components in the proposed structures. Instead, activation is controlled through the surrounding environment. In particular, the structures are activated using heated water to simulate a reduced gravity environment. This is typically used to test space deploying structures and machineries [81] and provides more uniform heating compared to say a heat lamp. A similar application on a microscopic level would be the activation of micro-structures in blood vessels through body heat.

### 4.3 METHOD AND DESIGN

#### 4.3.1 Material Selection

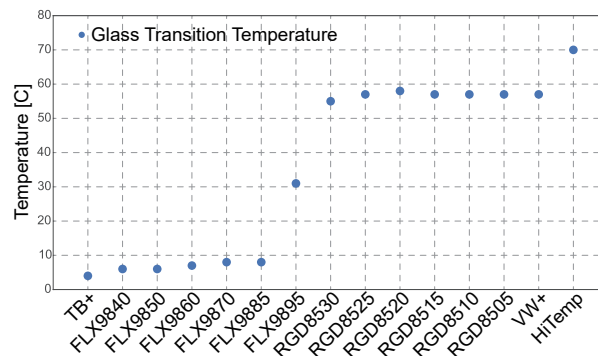


FIGURE 4.1: The glass transition temperature of the materials that are available to the Stratasys Objet 500 Connex 3 3D printer. Four groups of materials can be classified based on their  $T_g$ .

The precursor to this study follows the material characterization of VeroWhitePlus in Chapter 3, and uses Differential Scanning Calorimetry (DSC) to obtain the glass transition temper-



Material	Glass Transition Temperature
TB+ to FLX9885	$T_g < 10^\circ\text{C}$
FLX9895	$T_g \approx 30^\circ\text{C}$
RGD8530 to VW+	$T_g \approx 55^\circ\text{C}$
HiTemp	$T_g \approx 70^\circ\text{C}$

TABLE 4.1: The glass transition temperature of the four groups of materials.

ature  $T_g$  of all 12 digital materials between TangoBlackPlus (TB+), an elastomeric material, and VeroWhitePlus (VW+), as well as a high temperature material (HiTemp). The purpose of this study is to identify a SMP with a  $T_g$  distinct from other materials, such that the SMP can undergo a glass-rubber transition without affecting the other, “passive”, materials.

The results of this study (Fig. 4.1) show that there are four distinct temperature groups within the tested materials (Table 4.1). FLX9895 is a good candidate as the SMP; there is a complaint and a stiff material on either side on the temperature spectrum. RGD8530 is also a candidate as the SMP, however it was observed with DSC experiments that increase in heat capacity occurs over a large temperature range, i.e. the transition occurs at temperatures within 5 to 10 degrees of the stated  $T_g$ , and at such a temperature, HiTemp may rubberize as well.

A thermal-viscoelastic constitutive model is built for FLX9895 using a similar procedure as described in Chapter 3. A dynamic mechanical analysis (DMA) is used to obtain the storage modulus. The transformation of the storage modulus to relaxation modulus and modeling of this using the Prony series is detailed in Wagner, et al. [82]

#### 4.3.2 Programmable Unit Actuator

First, the geometry of the actuator design is introduced, then the kinematics and activation sequence are discussed, and lastly the mechanical behavior is investigated. For actuation, I propose a unit actuator consisting of a bistable mechanism that dictates the equilibrium states and shape change, and the shape memory strip (SMS) that provides the activation force. This unit actuator is capable of activating independently of the rest of the structure. The principle behind this proposed actuator is shown in Fig. 4.2a, where the shape memory effect is used to trigger bistability from the contracted to the expanded configuration or vice versa.

The bistable mechanism is a realization of the Von Mises Truss [83] and is adapted from designs proposed by Chen et al. [3] It is fabricated using rigid truss members, compliant joints and compliant beams. It has been shown that the activation force can be increased by increasing the joint material stiffness or decreasing the joint length. The flexible beam is added to better simulate the ideal boundary condition (Fig. 4.2b). The design is fabricated in either the contracted or the expanded configuration and is triggered by the SMS installed beneath the pin.



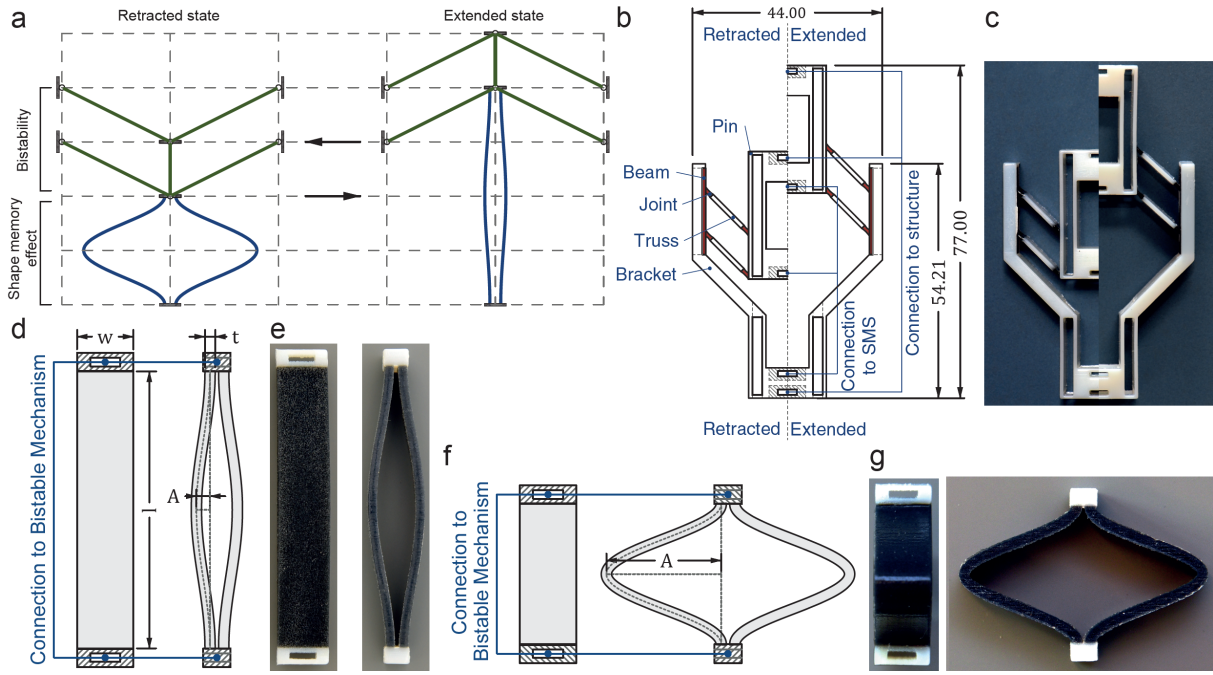


FIGURE 4.2: The design of a heat-activated bistable unit actuator. a) Schematic showing activation of the actuator. The actuator consists of a bistable mechanism and an SMS. The SMS provides the force to activate the bistable mechanism. b) The design of the unit actuator shows the bistable mechanism consisting of a bracket that provides structural rigidity, joints that provide the rotational DOF to the bistable trusses, and flexible beams that simulate the boundary condition of the von Mises truss. The overall dimensions and the connection points are indicated. d, f) The SMS whose geometry is parametrically defined to provide both expansion and contraction to the actuator. c, e, g) The fabricated specimens.

The SMS (Fig. 4.2d) consists of two thin, symmetrical strips with a rectangular cross section. The profile of the SMS is defined by a curve as bending is used as opposed to axial deformation, e.g. stretching, to maximize length change in the SMS without inducing excessive strain. The mechanical behavior of the SMS is parametrized by a cosine curve with amplitude  $A$  and thickness  $t$ . A cosine curve is used to reduce the stress concentration at the ends, as specimens typically fail at the interface between different materials. Fig. 4.2c shows an example of the unit actuator with the bistable mechanism. The stroke length of the bistable mechanism dictates the change in length of the SMS between the fabricated and the activated states. In this design, the stroke length is 20 mm, leading to a  $90^\circ$  rotation of the trusses.

The bistable mechanism is fabricated using TB+ as the compliant material, and HiTemp as the rigid material. Their  $T_g$  (Fig. 4.1) effectively renders both thermally stable at a temperature in the vicinity of the  $T_g$  of the SMS material, which is approximately  $30^\circ\text{C}$  (Fig. 4.1, FLX9895). While the actuator including both the bistable mechanism and the SMS can be fabricated in one piece, they are separated so that they can be investigated independently.

The deployment of the unit actuator procedure consists of two phases, the first phase is the programming and assembly of the SMS with the bistable mechanism. The second is the constrained recovery of the SMS and consequently the activation of the unit actuator. In the programming phase, the SMS is heated past  $T_g$  and is either stretched or compressed by a

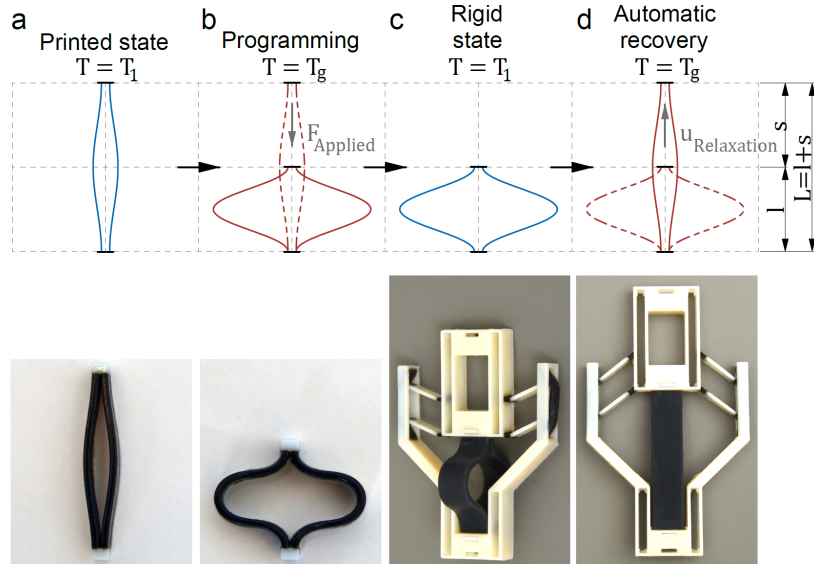


FIGURE 4.3: The programming and activation sequence of the unit actuator. a) The printed state of an expanded SMS. b) By heating the SMS past its  $T_g$  and applying a mechanical force, the SMS is deformed by the stroke length to its programmed state. c) The programmed SMS is cooled down and assembled into the bistable mechanism. d) The unit actuator is activated through heating. Upon cooling, the final activated state is rigid and behaves as a static member.

distance equal to the stroke length of the bistable mechanism (Fig. 4.3a to b). While confined, the SMS is cooled and installed in the bistable mechanism (Fig. 4.3c). The second phase is triggered by raising the temperature of the unit actuator past  $T_g$  (Fig. 4.3d). As the SMS recovers, it triggers the bistable mechanism and achieves the deployed state. Once cooled, this activated state behaves as a rigid structure as the SMS returns to its glassy state.

#### 4.3.2.1 Experimental Setup

To ensure deployment, the SMS must overcome the activation force of the bistable mechanism at all stages of the deployment process. Mechanical characterization of the SMS is performed in an Instron E3000 dynamic testing machine with an installed thermal chamber. The specimen is clamped with mechanical grippers. The interior volume of the heat chamber is heated to 40 °C. This temperature is maintained for 30 min prior to testing to ensure thermal equilibrium is reached. A displacement of 20 mm is applied and removed at a rate of 0.05 mm s<sup>-1</sup>. The reaction force is recorded with a load cell. This displacement is tensile for the extending SMS, and is compressive for the contracting SMS, and the magnitude of the displacement equals to the stroke length of the bistable mechanism. This experiment provides the stress strain behavior of the material under the rubbery state, and ensures that the resulting recovery force is sufficient to overcome the bistable mechanism's activation force.

#### 4.3.2.2 Simulation Procedure

To simulate the test condition, a Finite Element simulation is performed to obtain the behavior of the SMS using a linear viscoelastic constitutive model constructed for the shape memory

material. Static stress and strain behavior of the different materials is obtained from Chen et al. [3] Simulation of the bistable mechanism uses a static non-linear FEA with a prescribed displacement boundary condition and members are modeled with beam elements.

The bistable mechanism is meshed with a non-linear beam element B32 to reduce computational effort compared to brick elements while retaining accuracy. The flexible beam is assumed to be clamped on the ends. A hyperelastic material model is used for TB+. A displacement of 20 mm is prescribed to avoid snap-through and obtain the portion of the stress-strain curve with negative stiffness.

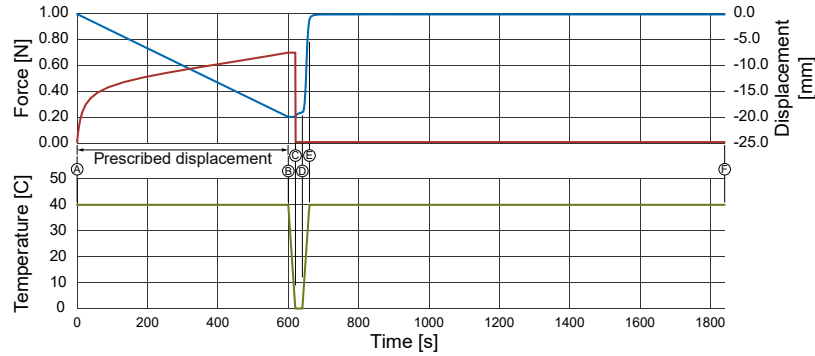


FIGURE 4.4: Simulation of the SMS with viscoelastic brick elements during programming and relaxation. From A to B, a displacement is prescribed under  $T = T_g$ , the reaction force is the output. From B to C, the prescribed displacement continues to be applied as the temperature decreases to 0°C. From C to D, the displacement is removed, a slight rebound is observed in deformation. From D to E, temperature increases and relaxation occurs. This continues to F.

Simulation of the SMS consists of a multi-step analysis (Fig. 4.4). The shape memory strips are meshed with viscoelastic brick elements C3D8RH. A displacement of 20 mm is incrementally applied under the heated condition (Step A to B). This displacement is maintained while the temperature cools to 0°C (Step B to C) and is removed from Step C to D. A slight rebound in displacement is observed. From Step D to E, the temperature is raised to 40°C and the relaxation is observed. Relaxation continues after the temperature reaches steady state.

#### 4.3.3 Deployable Structures

I demonstrate that the actuator can be integrated into a larger mechanical system first by showing the controlled activation of three serially connected actuators and then a autonomously deployable structure (Fig. 4.5). The serially connected actuators are designed such that the individual actuators sequentially. The sequence of activation is controlled by varying the thickness of the SMS. This is due to heat conduction of the shape memory polymer. The actuator is designed such that its pin is part of the frame of a second, serially connected actuator (Fig. 4.5b). This increases the overall expansion ratio as more actuators are linked.

Now the described actuators are integrated in 2D designs that deploy into load carrying 3D structures. An edge-node schematic of the structure is shown in Fig. 4.5c. The design can be simulated as a truss network, i.e. the edges can only sustain axial load and the nodes are

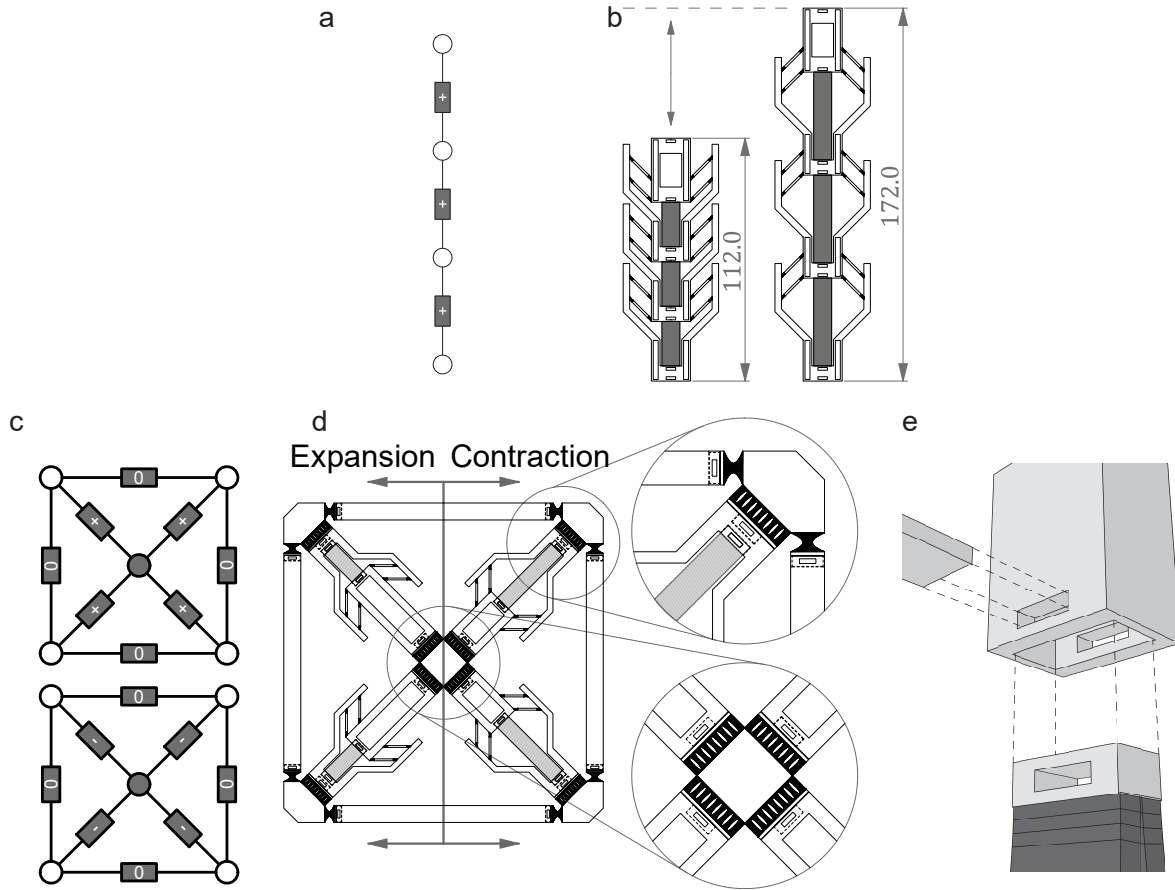


FIGURE 4.5: Schematic design of deployable structures. a) Schematic showing three expansion actuators connected in series (+) b) Physical design of the sequential actuators in both initial and final state. c) Schematic of the designs of the two types of deployable structures. Four actuators are integrated in a flexible frame, the first has four expansion actuators (+), and the second has four contraction actuators (-). d) The physical design of the structures, the compliant joints are fabricated with a flexible material and functionally graded to provide the desired flexibility and robustness. e) A detailed view of a universal connector between all parts of the assembly.

pin jointed. The design consists of a rectangular frame with four cross edges. Each edge can assume three behaviors: expansion, contraction or remain static. In this work, two physical realizations of the design are demonstrated by switching the initial configuration of the cross edges between expansion and contraction actuators (Fig. 4.5d). Compliant joints are placed at the nodes where rotational Degrees of Freedom (DOF) are required. The stiffness of the joints is reduced by fabricating them with a soft elastomer and internal microstructure. The different parts are assembled with a common joint (Fig. 4.5e).

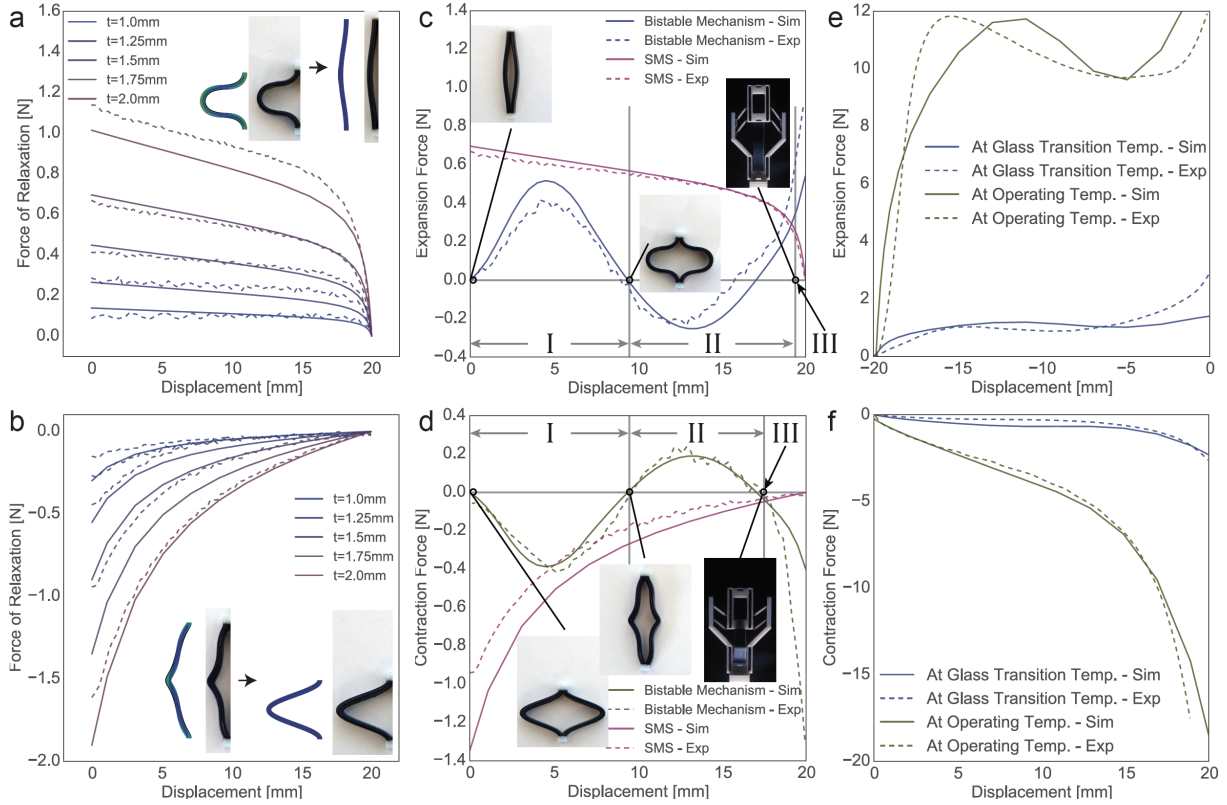


FIGURE 4.6: Mechanical characterization of the unit actuator, both in expansion (a, c, e) and contraction (b, d, f), including simulation (solid lines) and experimental (dashed lines), results in both the glassy and the rubbery regime. a, b) Parametric study of the influence of the SMS thickness and recovery direction on its activation force at a temperature load above  $T_g$ . The range of the thickness studies is between 1.0 and 2.0 mm in 0.25 mm intervals. c, d) The force/displacement curves of the bistable mechanism and the chosen SMS. Activation is guaranteed when the SMS force is greater than the bistable force in region I. In region II, both SMS and bistability are acting in the same direction. Stable equilibrium is indicated at point III. e, f) These plots compare the overall behavior of the actuator at  $T_g$  and at an operating temperature of 20 °C

## 4.4 RESULTS AND DISCUSSION

### 4.4.1 Programmable Unit Actuator

Simulation and experimental results are shown in Fig. 4.6. Panels a and b show the force exerted by the SMS during relaxation when  $T \geq T_g$ . Under this deformation, the maximum strain within the extending and the contracting SMS is 0.258 and 0.374 respectively. By varying the thickness of the SMS, the force can be tuned from 0.1 to 1 N during expansion and 0.1 to 2 N for contraction. Using this data, I select a SMS with the force required to activate the bistable mechanism. As shown in Panels c and d, to activate the bistable mechanism when  $T \geq T_g$ , the SMS must deliver a constrained relaxation force that is greater than the bistability activation force, i.e.  $F_{SMS} - F_{bi} \geq 0$ . This must be explicitly satisfied in Region I where the bistable force acts in opposition to the SMS. In Region II, after the bistable mechanism triggers, both forces act in the same direction. This enables the force amplification characteristic of the



bistable mechanism. Equilibrium occurs at the end of Region II where the two forces balance once again (labelled as III). Note that this is slightly before full stroke length as the bistable mechanism has an asymmetrical behavior.

Panels e and f show the overall mechanical behavior of a unit actuator under either activation temperature (i.e.  $T \geq T_g$ ) or operating temperature (i.e.  $T < T_g$ , in this case,  $T \sim 22^\circ\text{C}$ ). In the first instance, the overall behavior equals to the sum of the relaxation force of the SMS and the activation force of the bistable mechanism. In the second instance, by cooling the SMS to its glassy state, its Young's modulus increases significantly. As a result, the unit actuator behaves as if it were a static structural element, allowing a much stiffer force displacement response.

#### 4.4.2 Deployable Structures

Testing of the deployable structures are done under water that is heated with a heating element. For deployment, water is heated past  $T_g$  before the specimens are submerged.

For the serially connected actuators, first I identify the SMS with the sufficient force to trigger bistability. The activation force of the SMS with different thickness show a monotonic increase ranging from 0.2 to 1.0 N in the expansion direction (Fig. 4.7a) and 0.3 to 2.0 N in the contraction direction (Fig. 4.7b).

Actuators with thickness above 1.5 mm provide sufficient force to trigger the bistable mechanism. Therefore the thicknesses of 1.50, 1.75, 2.00 mm are used for the SMS as they can all trigger the bistable element, yet have different activation times. The activation sequence begins with the thinnest SMS and completes with the thickest SMS (Fig. 4.7c).

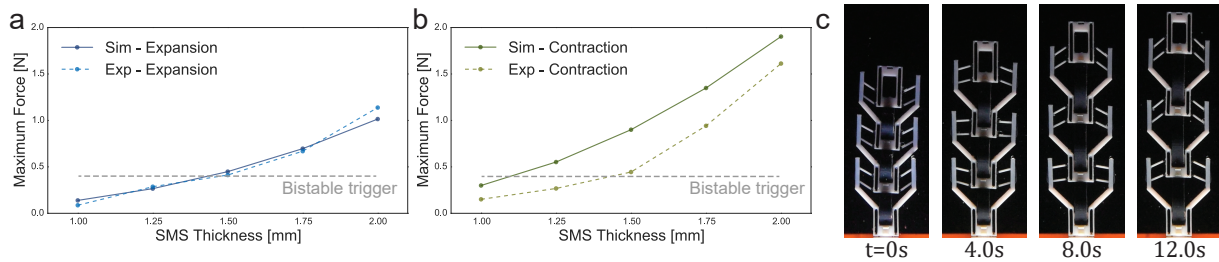


FIGURE 4.7: Serially connected actuators activating in sequence. a, b) Activation force of the SMS of different thickness in both expansion and contraction directions. c) Video stills of the activation process. Both simulation and experimental results are shown.

For the deployable structures (Fig. 4.8), due to the fast activation time, the specimens are slightly activated by the time they are placed at the base of the water tank. The water is cooled below  $T_g$  to test structural behavior under operating conditions.

Each SMS is programmed separately and assembled into the structure. The initial state is planar. For deployment, the structure is submerged under  $40^\circ\text{C}$  water. Self-weight of the structures is neglected as the density of the materials are approximately  $1175\text{ kg m}^{-3}$ , which is slightly higher than water. Both structures activate as predicted assuming the actuators are

springs pre-strained by the stroke length. With the expanding structure, a synclastic surface is formed resembling a pyramid. With the contracting structure, an anticlastic surface is formed. The timing of the activation for both is under three minutes, which is significantly faster than using swelling.

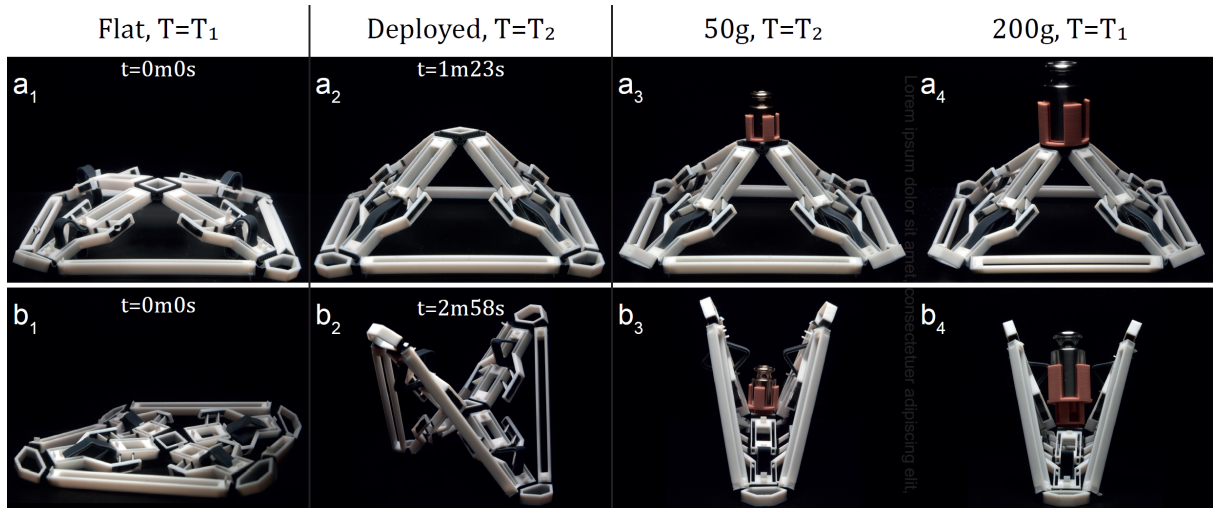


FIGURE 4.8: Shape reconfigurable structures showing activation and load-bearing capability. (a, b) Video screen captures of the expanding and contracting structural deployment, respectively, (1) flat state, (2) activated state, (3) load-bearing capacity under high temperature, and (4) load-bearing capacity under operating temperature

In addition to activation, two load cases are tested by placing a specified mass at the apex of each structure. The first is under the deployment condition where the temperature remains at  $40^{\circ}\text{C}$ . The load sustained is  $0.050\text{ kg}$ , or an equivalent weight of  $0.430\text{ N}$ . The second load case is conducted after the surrounding temperature lowers to approximately  $22^{\circ}\text{C}$ . The load sustained is  $0.20\text{ kg}$  or an equivalent weight of  $1.70\text{ N}$ .

## 4.5 CONCLUSION

The presented work demonstrates the design of autonomous shape reconfigurable structures. I propose a programmable unit actuator that either expands or contracts under temperature change. Using the viscoelastic behavior of thermosetting polymers, a pre-strain is imposed on the Shape Memory Strips (SMS) at a temperature greater than the polymer's glass transition temperature,  $T_g$ . This pre-strain locks in when the temperature lowers and is released when the temperature increases again, thereby triggering the bistable mechanism. Using this actuator, the deployment of 2D sequenced actuators and load bearing 3D space structures are demonstrated.

The proposed unit actuator can be integrated in structural applications where the transport volume must be much smaller than the operating volume. With respect to the example of deployable space structures, the proposed design has a number of advantages compared to the state-of-art in all phases of the deployment process. In the fabrication phase, both the bistable mechanism and the SMS are 3D printed with minimal support material and assembled with

a universal connector (Fig. 4.5c). The activation force of the bistable mechanism is dependent on its joint length and stiffness. [3] The triggering temperature and duration of the SMS can be tuned by varying the chemical composition of the shape memory polymer resin [57] and by changing its thickness respectively.

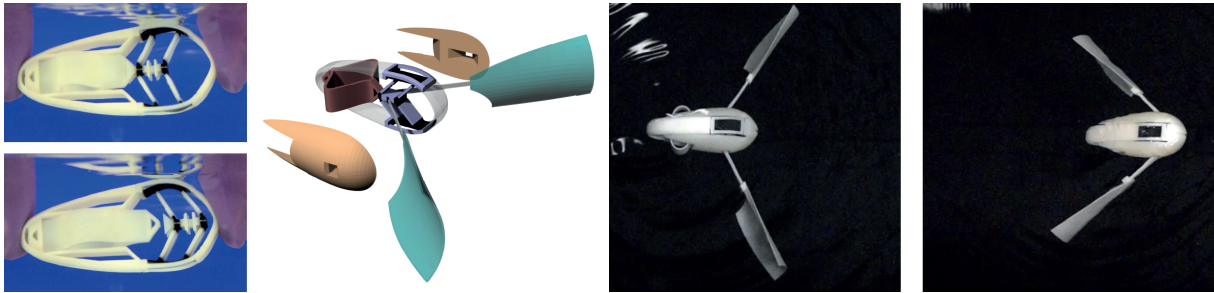
In transportation and the deployment phase, the stowed or programmed state of the proposed structure is precisely defined by the first equilibrium point of the bistable mechanism. This stowed state is maintained without a restraining mechanism. [84] Rather than motorized deployment, the proposed structures are activated through environmental change, thereby removing the need for electrical energy input and eliminating the possibility of jamming of parts.

While initially flat structures are demonstrated as an example, one is able to design the stowed state to accommodate given space requirements. By contrast, designs that feature only SMPs are programmed with limited precision using ad-hoc methods such as hand pulling. [85] The proposed structures are load bearing as they are deployed, i.e. under high temperature, as the bistable mechanism amplifies the load bearing capacity of the unit actuator independently of the surrounding temperature. This is in contrast with most 4D printed designs that focus solely on shape transformation<sup>8</sup> and do not exhibit significant load bearing capacity during deployment but rather only after the deployed design cools below  $T_g$ . Under operating temperature (i.e.  $T < T_g$ ), the SMS returns to its glassy state and behaves as a rigid member, effectively making the unit actuator a static structural element.

As demonstrated, the structures can reconfigure themselves both positively and negatively, with a combination of these two modes and given many actuators, one can form a surface of almost any given curvature. As I have characterized the thermal mechanical behavior of the unit actuator, simulation of the deployment can be done using form-finding algorithms, developed in previous work, that can be extended to generate and optimize large scale reconfigurable structures. [3]



## AUTONOMOUS ROBOTIC PROPULSION



The content of this chapter has been previously published in *Proceedings of the National Academy of Sciences*,

Chen, T., Bilal, O. R., Shea, K. & Daraio, C. (2018), Harnessing bistability for directional propulsion of untethered, soft robots, *Proceedings of the National Academy of Sciences of the United States of America*, 115(22), 5698–5702.

### 5.1 SUMMARY

A major challenge in soft robotics is the integration of sensing, actuation, control, and propulsion. In most macro-scale robotic systems, propulsion and controls are enabled through a physical tether or complex on-board electronics and batteries. A tether simplifies the design process but limits the range of motion of the robot, while on-board controls and power supplies are heavy and complicate the design process. Here, I present a material-based design principle for an untethered, soft swimming robot with preprogrammed, directional propulsion without a battery or on-board electronics.

I further utilize the actuator that consists of a bistable mechanism and a shape memory polymer (SMP) to achieve propulsion. With the SMP acting as a thermally activated muscle, the actuator harnesses the large displacement of the bistable mechanism to push the fins backward, and the robot forward. The swimming robots are fabricated using a commercially available 3D printer. As a proof of principle, these robots are shown to be able to be preprogrammed to follow specific routes or deliver a cargo and navigate back to their starting point.

## 5.2 BACKGROUND

Soft robotics [2, 86–89] and robotic materials (a.k.a. programmable matter) [90–92] are blurring the boundary between materials and machines while promising a better, simpler, safer and more adaptive interface with humans [93, 94]. Propulsion and navigation are core to both soft and rigid robotic systems. Autonomous (or pre-programmed) propulsion is a central element in the road map for future autonomous systems, enabling, for example, unguided traversal of open waters (e.g., studying marine biology [95], ocean dynamics [96]). Power supply to enable propulsion remains one of the major obstacles in all forms of locomotion. One of the easiest solutions for supplying power to soft robots is the use of a tether [87]. Tethered pneumatics, for example, enabled active agonistic and antagonistic motion [21] and an undulating serpentine [97]. Dielectric elastomers were used to create tethered soft crawlers [20] and to simulate the up and down motion of a jellyfish [98]. Electro-magnetics were used to create a tethered Earthworm-like robot [99], and untethered micro-swimmers under a rotating magnetic field [100]. A pressure deforming elastomer was utilized to design an artificial fish tail that can perform maneuvers [101]. Untethered robots, on the contrary, sacrifice simplicity in design for moving freedom without restriction. An untethered robot needs to encapsulate programming, sensing, actuation, and more importantly, an on-board power source.

The demonstration of an entirely soft (composed of materials with elasticity moduli on the order of  $1 \times 10^4$  to  $1 \times 10^9$  Pa) untethered robot, “the Octobot” [2], opened the door to a new generation of robots [89]. The Octobot is powered through regulated pressure generating a chemical reaction. Fabrication of the Octobot requires a combination of lithography, molding, and 3D printing. However, it does not exhibit locomotion. A common feature of all current demonstrations of soft robots is the presence of a complex internal architecture as a result of multi-step fabrication and assembly process. Here, a methodology is presented for designing an untethered, soft robot, which can propel itself and can be pre-programmed to follow selected trajectories. Furthermore the robot can be preprogrammed to reach a destination, deliver a cargo and then reverse its propulsion direction to return back to its initial delivery point. The robot can be fabricated using a commercially available 3D printer in a single print. However, the presented prototypes are partitioned to highlight the different components and speed up the printing process.

I focus on the actuation, design and fabrication of a robot that exploits bistable actuation for propulsion, and responds to temperature changes in the environment, to control its directional locomotion. Shape memory polymers (SMPs) is used to create bistable “muscles” that respond to temperature changes in the environment. Bistable actuation is often found in biological systems, like the Venus fly-trap [102] and the Mantis shrimp [103]. When working near instabilities, bistability can amplify displacements with the application of a small, incremental force [15]. Engineers started to integrate instabilities in design [94], for example, in space structures [28], energy absorption mechanism [29] [17] and fly-trapping robots [32]. By amplifying the response of soft SMP muscles, snap-through instabilities can instantaneously exert high force and trigger large geometrical changes [14]. Bistability has also been utilized to

sustain a propagating solitary wave in a soft medium [15]. More recently bistability enabled the realization of the first purely acoustic transistor and mechanical calculator [104]. A typical bistability is found in the Von Mises truss design, which allows a simple 1D system to have two stable states [36]. Combining this principle with multi-material 3D printing, it is possible to realize bistable actuators with a tunable activation force through material and geometry changes [3]. These actuators can be used to create load-bearing, multi-state reconfigurable 3D printed structures, where large shape changes are possible due to the long stroke length of the bistable actuator design. To activate them, they can be combined with 3D printed shape memory strips, which respond to different temperatures, to create time sequenced linear actuators and the first 4D printed, deployable structures [105]. Here, I build on these works to create untethered robots.

### 5.3 METHOD AND DESIGN

#### 5.3.1 Propulsion Element

First the “engine” and the “power supply” of the swimming robot is described. To achieve propulsion, I further leverage the pairing of a bistable mechanism and a SMP-based muscle (Fig. 5.1a). In this design, the SMP muscle supplies the “power” to trigger the bistable mechanism, the “engine”, which in turn drives the robot forward. The SMP muscle consists of two strips of SMP material similar to the design in Chapter 4. The SMP muscle is fixed at one end, and in touch contact with the bistable mechanism at the other end. The bistable mechanism is fabricated using a compliant and a stiff material. The fixed supports are provided by a chassis. In the design, the SMP muscle expands and moves the bistable mechanism from equilibrium state I to II (Fig. 5.1b). Due to the inherent asymmetry of the stress-strain behavior of the bistable mechanism, the two equilibrium states are not equally energetic. This allows for a larger energy release which translates to forward motion.

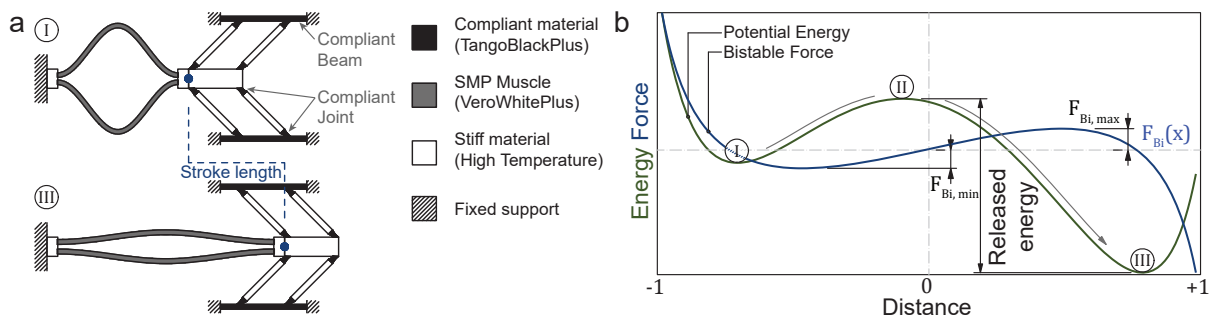


FIGURE 5.1: Propulsion through bistability. a) Schematic of the bistable mechanism and SMP muscle pair, before (I) and after (III) actuation. Different material assignment and support conditions are indicated. The SMP muscle is rotated  $90^\circ$  with respect to the bistable element for visualization. b) Energy potential of the bistable element with two stable states: I and III. The asymmetry in the curve indicates the need for a larger amount of energy to move backward than forward.

The SMP muscle must be programmed prior to insertion into the actuator assembly. Programming involves heating the SMP to above its  $T_g$ , compressing it by an amount equaling to the stroke length of the bistable mechanism, and cooling it down to room temperature  $T = R.T.$  (Fig. 5.2a). The SMP muscle is then inserted in position to trigger the bistable mechanism when the temperature reaches  $T_g$  (Fig. 5.2b).

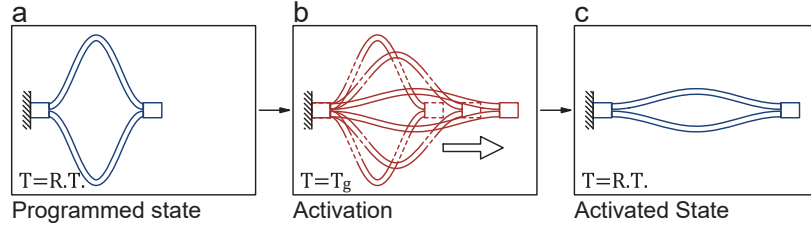


FIGURE 5.2: Programming activation cycle of the SMP muscle, including insertion (I), transition (II), and activated phases (III).

To trigger the instability, the actuation force of the SMP must overcome the energy barrier of the bistable mechanism, i.e.  $F_{Bi,min}$  (Fig. 5.1b). First I derive an analytical relationship between the applied force and the displacement of the bistable mechanism, taking into account the contribution from both the compliant beam and the compliant joint (Fig. 5.1a). The compliant beam is modeled as a linear spring with the spring stiffness derived from assuming the beam undergoing four point bending. The derivation assumes the bistable mechanism is in a deformed state prior to snapping. The variables are shown in Fig. 5.3.

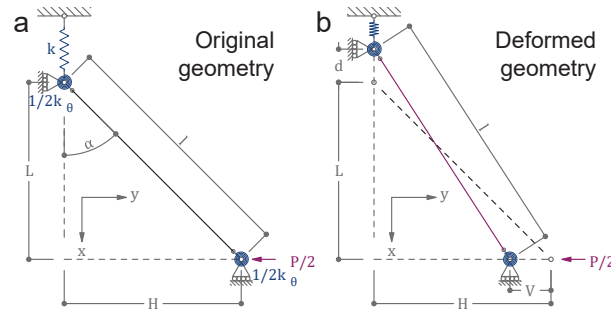


FIGURE 5.3: An idealization of the bistable mechanism in both the original and an deformed state. The support is idealized by a linear spring  $k$ , and the joints by a torsional spring  $k_\theta$ .

In order to determine the range of operational actuation forces, the finite element method is used to simulate the constrained recovery of the actuation pair (i.e., the bistable mechanism and the SMP muscle). The thickness of the SMP beams is varied between 0.6 and 1.6 mm. A geometrical non-linear solver with thermal-viscoelastic material model is used. To determine the activation time needed, the actuation process is simulated using an invariant boundary temperature, while calculating the time for the muscles to reach thermal equilibrium through conductive heating. To characterize the activation time experimentally, six SMP muscles were first programmed and then submerged in hot water simultaneously.

### 5.3.2 Swimming robot

To demonstrate the underlying principle of the design concept, I first study a robot propelled by a single actuator (Fig. 5.4). To reduce design complexity and ease prototyping, the robot (Fig. 5.1a) is decomposed into five parts (outer shell, floaters, fins, bistable mechanism and shape memory “muscle”). The shell supports the bistable mechanism to ensure linear actuation and provide stability for the robot. The floaters insure that, in the vertical direction, the SMP strips are fully submerged in water. The groove in the floaters provides the pivot point for the fins. The fins are attached to the bistable mechanism with elastomeric joints, ensuring flexibility. The vertical equilibrium of the robot is achieved by balancing buoyancy and weight, in-plane acceleration occurs when propulsion overcomes drag.

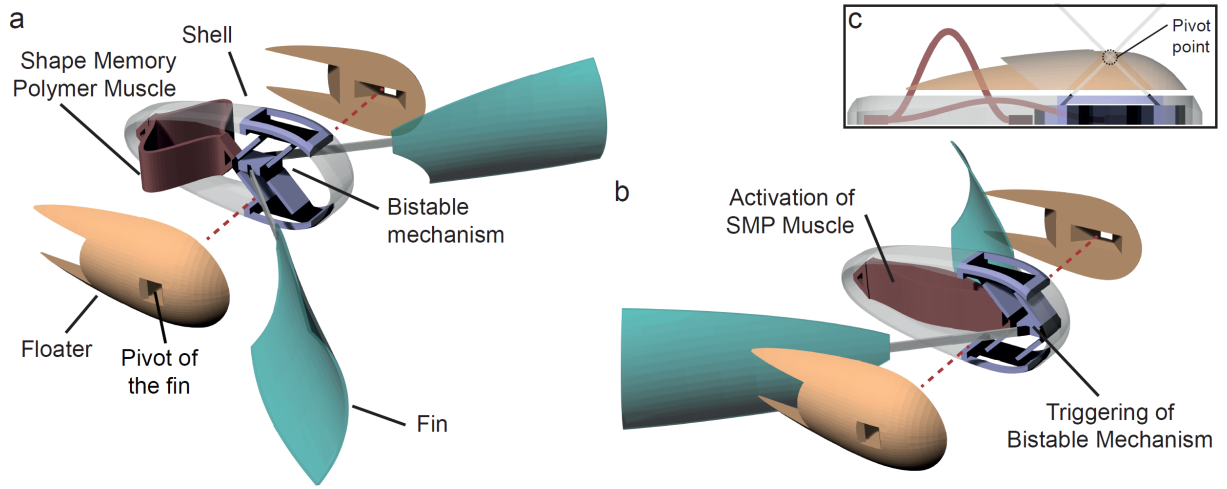


FIGURE 5.4: Design of a single actuator swimming robot. The different components are false colored and labeled. Note that the floaters are moved aside to give a better view of the internal mechanisms. a) shows the robot prior to actuation. b) shows the robot post actuation. c) shows the actual position of the floaters, and the position of the pivot given by the floating element.

The propulsion mechanism follows the forward motion of many organisms with fins submerged in water [106]. The fins, which perform a paddling motion, are driven primarily by destabilizing buckling trusses. Before deploying the robot, the printed SMP muscle is heated past its glass transition temperature ( $T_g$ ) and mechanically deform it to the programmed shape (Fig. 5.2). After deploying the robot in water with temperature equal-to or larger-than ( $T_g$ ), the muscle relaxes, transforming back into its original/printed shape. Since this is a constrained relaxation, the muscle must overcome the activation force of the bistable mechanism at all points between state I and II, i.e.  $F_{SMP}(x) > F_{Bi}(x) \quad \forall x = -1, \dots, 0$  (Fig. 5.1b). Post actuation, the system transitions into state III.

This robot is fabricated with a multi-material Stratasys Connex printer. The SMP muscles are fabricated with VeroWhitePlus plastic ( $T_g \simeq 60^\circ$ ). The compliant components within the bistable mechanism are fabricated with Agilus30 with ( $T_g < -5^\circ$ ) and therefore remains in the rubbery state throughout the experiments. All remaining components are fabricated with a high temperature resistant material, RGD525 ( $T_g > 80^\circ$ ), which retains its stiffness

throughout the activation process [82]. The stiffness of the materials used in the actuator are VeroWhitePlus (1 GPa) and Agilus30 (1 MPa), which falls within the range of soft materials as defined in Wehner, et al.[2]

A water container is used to test the performance of the swimming robots. The dimensions for the water container used to demonstrate the single and sequential motion is 967(L) x 555(W) x 393(H) mm. The water is heated by an Atwood heating element keeping the water temperature consistently above the glass transition temperature of the used materials. This setup is used for all subsequent robots.

### 5.3.3 Sequential and Directional Propulsion

The use of bistability for propulsion can be expanded from a single-stroke to a multi-stroke robot (Fig. 5.5a). Multiple bistable mechanism-muscle pairs can be compacted into the same robot in either a connected or separate fashion. If  $N$  pairs are completely disconnected, they can induce  $N$  independent strokes that are either simultaneous (using identical pairs) or sequenced (using different ones). If the pairs are connected in series (e.g., the muscle of pair two is attached to the bistable mechanism of pair one), they can create synchronized strokes based on the propagation of a Soliton-like actuation (Fig. 5.5b) [16]. This guarantees that  $n^{\text{th}}$  stroke will always be executed before the  $(n + 1)^{\text{th}}$ .

The schematic in Fig. 5.5b(II) shows post-activation of actuation pair one, muscle two is moved into position to activate the bistable mechanism of pair two. As the combined force of the already-activated bistable mechanism and the muscle from pair one is greater than the actuation force of muscle two, i.e.,  $F_{\text{Act},1} + F_{\text{Bi,max}} > F_{\text{Act},2} > F_{\text{Bi,min}}$ , muscle two displaces more in the forward direction and activates the second bistable mechanism. This creates a forward chain action.

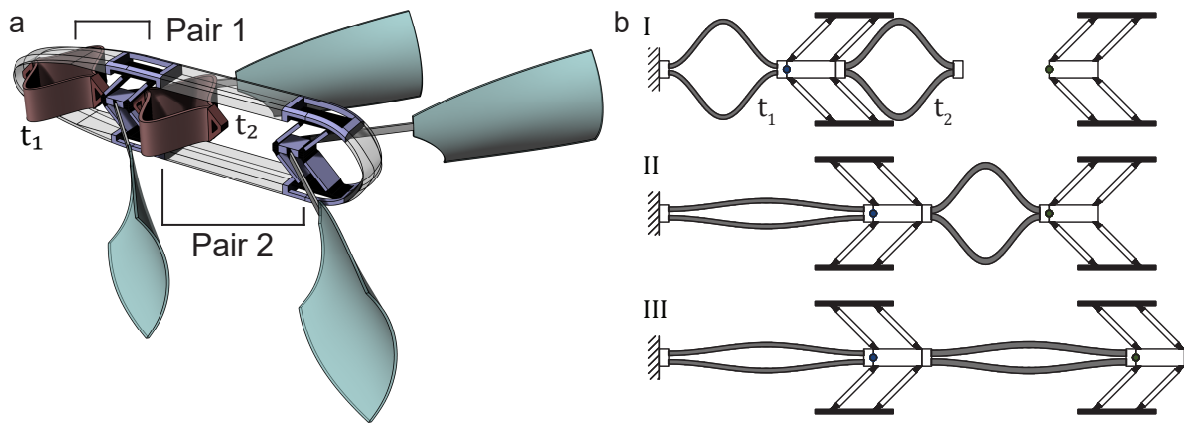


FIGURE 5.5: Sequential and directional propulsion: a) A schematic of a robot with two bistable mechanism-muscle pairs. A thinner muscle with faster actuation time is placed at the rear, i.e.,  $t_1 < t_2$ . b) Activation sequence: (I) initial state with both muscles programmed. (II) the thinner muscle activates, triggering the first bistable mechanism and pushing the second muscle to touch the second bistable mechanism. (III) The second (thicker) muscle triggers the second bistable mechanism.



In addition to the increased net forward motion, due to the added actuation pairs, propulsion in various directions can be achieved by adjusting the placement of the fins. Having two fins (one on each side) induces a symmetric moment that moves the robot forward. When one of the fins is removed, an asymmetric moment arises, giving the robot a push towards the direction of the missing fin. By strategically placing the fins, navigation can be preprogrammed in advance, setting the robot on a predefined path. The sequential nature of actuation allows for predictable directional change at each stage.

#### 5.3.4 Cargo Delivery and Reverse Navigation

In many scenarios, such as cargo delivery or retrieval, a robot is required to navigate back to the starting point of its journey after the required operation is completed. To demonstrate cargo delivery and robot return, a shape memory gripper is added at the front of the robot to hold a 3D-printed penny (Fig. 5.6a). The sequential and directional motion of the robot presented so far is based on identical muscles (i.e., same material) with varying thickness. This thickness variation translates into different activation times at the same temperature.

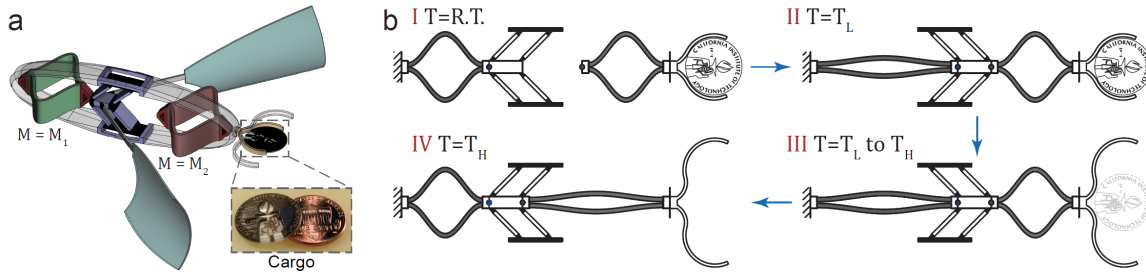


FIGURE 5.6: Reverse navigation: A schematic of a robot with two muscles and a single bistable mechanism. The first muscle,  $M_1$ , is fabricated with a material that activates at  $T_L$ . The second muscle,  $M_2$ , activates at  $T_H$ , which is higher than  $T_L$ . b) Sequence of activation, (I) at room temperature,  $T_{R.T.}$ , both muscles are programmed. (II) As water temperature increases to  $T_L$ , the first muscle triggers the bistable mechanism and propels the swimmer forward. (III) As water heats to  $T_H$ , the grippers relax and release the cargo. (iv) When the water temperature reaches  $T_H$ , the second muscle reverses the bistable mechanism and reverses the robot back to its starting position.

In order to design the robot to reverse its navigation path, an extra muscle is incorporated on the other side of the bistable mechanism (Fig. 5.6a). For the second set of muscles (i.e., for reverse navigation) I add an extra dimension to the design, that is the activation temperatures. As it has been shown that by varying the constituting Inkjet materials, one can achieve different glass transition temperatures [13]. Utilizing this property, two identical muscles are fabricated with two different materials and therefore activation temperatures  $T_L$  and  $T_H$ . The second muscle induces enough force to overcome both the bistable potential and the first muscle. Such force can trigger the instability producing a force in the opposite direction to the initial actuation, causing the robot to reverse its navigation direction. In this case, material  $M_1$  is FLX9895, with  $T_g \simeq 35^\circ$ .



## 5.4 RESULTS AND DISCUSSION

### 5.4.1 Propulsion Element

In order to analyze the bistable mechanism, I first fabricate a bistable mechanism-muscle pair enclosed in a planar shell identical to that of a single stroke swimming robot (Fig. 5.7). The four bars within the bistable mechanism form two “V” shapes pointing to the right, representing one of the stable states of the mechanism. The sample (the pair confined in the planar shell) is then immersed in 60 °C water (state I), equivalent to the glass transition temperature of the muscle material (VeroWhitePlus). As the muscle temperature rises due to water contact, both of the deformed beams within the muscle start relaxing into their original/printed shape. At the onset of the instability, where the truss-like bars of the bistable mechanism are vertical (state II), the muscle pushes the mechanism slightly towards its second stable state (where the “V” shapes are pointing to the left) (state III).

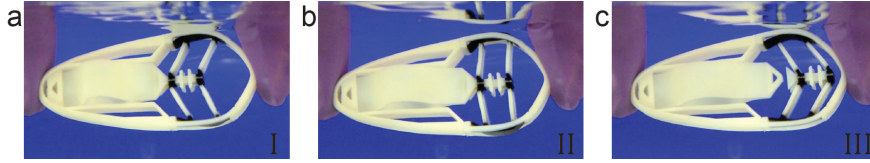


FIGURE 5.7: Video snapshot of the actuation of the bistable mechanism. Note that from stage II to III, the SMP muscle does not contribute to propulsion as it is completely detached from the bistable mechanism.

In order to model the bistable behavior of the mechanism, one of its four bars is considered (Fig. 5.3). The bars are printed with VeroWhitePlus with Young’s modulus  $E = 2 \times 10^9$  Pa, while its connections to the planar shell are printed with TangoBlackPlus with a Young’s modulus  $E = 2 \times 10^6$  Pa. Since the bar material has a stiffness that is  $1e3$  higher than its connection points, the bar is modeled as an inclined rigid truss element supported by two torsional springs with a spring constant ( $k_\theta$ ) and a linear spring with a constant ( $k$ ). The rotational springs  $k_\theta$  are the torsional resistance of the compliant joints. The linear spring,  $k$  simulates bending of the flexible support through linear force in the  $y$  direction. A Lagrangian equation is used to construct a relationship between the force  $P$  and the corresponding displacement  $V$  with respect to the deformed geometry. The bar is assumed to be axially rigid.

$$\mathcal{L} = \frac{1}{2}kd^2 + \frac{1}{2}k_\theta\Delta\alpha^2 - \frac{1}{2}PV \quad (5.1)$$

Then I consider the deformed geometry with a rigid truss bar, to relate the different displacements in the model:

$$\sqrt{H^2 + L^2} = \sqrt{(H - V)^2 + (L + d)^2} \quad (5.2)$$

The solution of  $d$  is the difference between the deformed projected length and the original one,

$$d = \sqrt{2HV + L^2 - V^2} - L \equiv L_1 - L \quad (5.3)$$

To simplify the representation, the first term of the solution is denoted as  $L_1$ . The Lagrangian equation becomes

$$\mathcal{L} = \frac{1}{2}k(L_1 - L)^2 + \frac{1}{2}k_\theta \left( \arctan \frac{H - V}{L_1} - \arctan \frac{H}{L} \right)^2 - \frac{1}{2}PV \quad (5.4)$$

I obtain the relationship between  $P$  and  $V$ , by differentiating the system w.r.t. to  $V$  and setting the result to zero,  $\frac{\partial \mathcal{L}}{\partial V} = 0$ . Such an equation provides the means to assess the impact each variable on the overall behavior of the system has, and therefore design the bistable mechanism.

$$P = -2\frac{1}{L_1} \left[ k(L - L_1)(H - V) + k_\theta \left( \arctan \left( \frac{H - V}{L_1} \right) - \arctan \left( \frac{H}{L} \right) \right) \right] \quad (5.5)$$

In the initial state (I), The shape memory muscle doesn't exert any force  $P = 0$  on the bistable mechanism. As the surrounding water heats the muscle, it starts to relax to its original/printed shape, pushing the bistable truss towards its second stable state. Until the muscle pushes the truss to be vertical, i.e.  $H = 0$  (II), beyond this point, the mechanism flips to the second equilibrium state (III), where the muscle is physically detached from the mechanism.

The FE analyses of SMP muscle and bistable mechanism pair show that full recovery (i.e., snapping of the bistable mechanism) does not occur for beams with thicknesses lower than 1.2 mm (Fig. 5.8a). Thinner beams induce localized stresses in the bistable mechanism, although not enough to cause it to snap. The recovery forces of the muscle range from 0.2 to 2.1 N in simulation (Fig. 5.8b). However, slightly larger forces are observed experimentally at higher thickness values due to the fusion of the two SMP beam strips at both ends of the muscle during polymerization. The time of activation is extracted from the recorded video. At equal length, the force supplied by the muscles as well as the actuation time increases with thickness (Fig. 5.8b).

#### 5.4.2 *Swimming Robot*

By observing the forward movement, it is observed that the forward motion of the robot occurs in the transition between state a and c, and consists of prior- and post-snapping (Fig. 5.9). Prior to the onset of the instability, the shape memory muscle moves the bistable mechanism and drives the fins backward until they are perpendicular to the direction of motion. This is a relatively slow motion with low energy output. Immediately after, the bistable mechanism snaps to its second equilibrium position. This drives the fins rapidly and increases the velocity of the robot. The difference is shown by recording the time of each state transition.

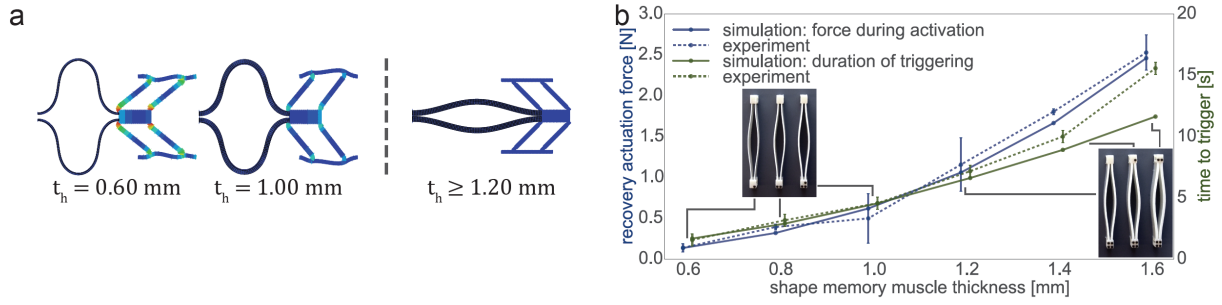


FIGURE 5.8: Actuator design: a) FEM simulations of the constrained recovery of the bistable-muscle pair. The vertical dashed black line separates thicknesses unable to activate the bistable mechanism (left) from functional thicknesses (right). b) Experimental and numerical correlation between the thickness of the SMP muscle and its recovery forces as well as the time it takes to heat to its original shape. The inset shows the different muscles tested. The error bars in the force readings represent the standard deviation. The error bars for the activation times represent the error in reading the times from video recordings of the experiments.

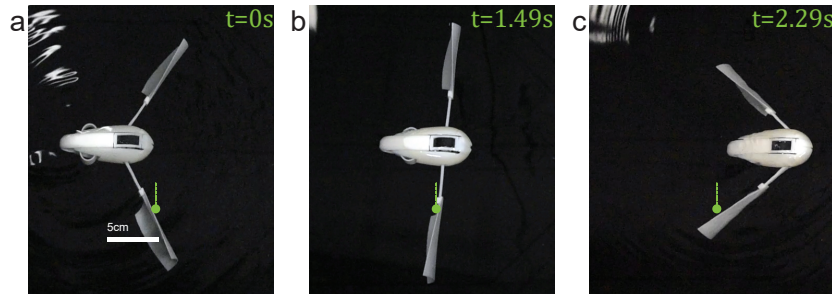


FIGURE 5.9: Video stills of the single stroke swimming robot from the initial state (a), to moments before instability is triggered (b), to the second equilibrium state (c).

In order to assess the contribution of the muscle-induced force on the distance traveled by the swimming robot, the same robot is deployed with various muscles. The thickness of the beams within the muscle is increased systematically, therefore increasing the resultant force (Fig. 5.10a). For beams with thickness  $t < 1.2$  mm, the robot did not move forward, as the muscle force is not strong enough to overcome the bistability energy barrier. All the muscles with beams  $t \geq 1.2$  mm overcame the energy barrier and were able to propel the robot forward. However, the robot traveled the same distance (Fig. 5.10b), regardless of the increase of the force amplitude by a factor 2. Therefore, the distance traveled by the swimmer depends on the bistable mechanism rather than the muscle force, as long as the muscle is strong enough to push the mechanism to the onset of the instability.

Such demonstration shows the significance of the bistability and long stroke length for the propulsion of soft robots, regardless of the initial actuation force. Since inducing a stroke depends on overcoming the bistable energy barrier rather than the actuator force, the bistable mechanism can be designed with a very small energy barrier [104] and high asymmetry [15]. This is also promising for the miniaturization of the actuators and the increase of the number of actuators in a given robot.

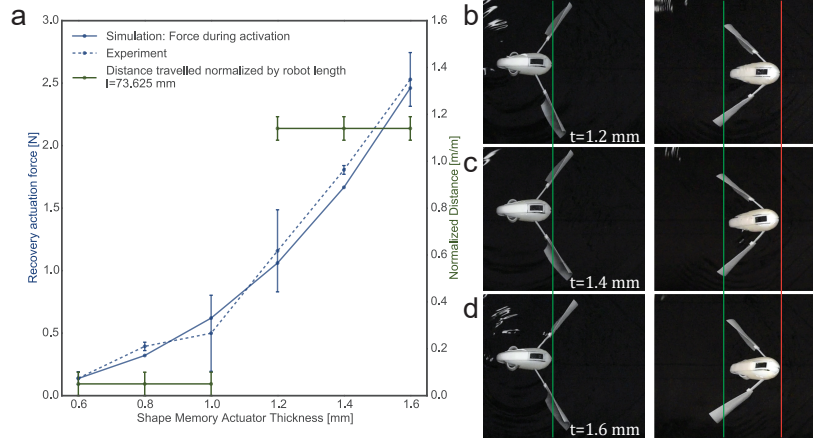


FIGURE 5.10: Effect of SMP thickness on distance traveled. a) Plot showing the activation force of the SMP muscles with varying thickness and the corresponding distance traveled. b) Three swimmers travel the same distance when the shape memory actuator of three different beam thicknesses are used. This shows that propulsion comes predominantly from triggering of the bistable mechanism. The beam thickness values are 1.2 mm, 1.4 mm and 1.6 mm.

#### 5.4.3 Sequential and Directional Propulsion

To demonstrate the sequential forward motion of the robot, four fins are placed symmetrically on the sides of two actuation pairs. The force needed to trigger the bistable mechanism is identical to that of the single stroke robot. The thickness of the rear muscle is 1.2 mm, while the front one is 1.6 mm, to have a sufficient time gap between the two activations. Once deployed, two consecutive forward motions are executed, increasing the overall distance traveled to 190% of a single stroke robot length (Fig. 5.11a). Next, the front left fin is removed and the robot is deployed again (Fig. 5.11b). The rear (symmetric) actuation induces a forward motion followed by a left turn with  $\approx 23.85^\circ$ . Afterwards, the robot is deployed with only two fins placed asymmetrically in the front-left and rear-right position (Fig. 5.11c). The robot takes a left turn of  $\approx 21.64^\circ$  followed by a right one of  $\approx -21.45^\circ$ . By designing different sizes of fins, one can control the turn angle of the robot. These different configurations show that by combining series of the bistability-muscle pairs and arranging the fins accordingly, one can navigate the swimmer in a predefined path.

#### 5.4.4 Cargo Delivery and Reverse Navigation

Once the reversing robot is deployed in water with temperature,  $T_L$ , the first muscle activates and triggers the bistable mechanism, thus propelling the swimmer forward to the delivery point (Fig. 5.12b). Once the water temperature reaches the glass transition temperature of the gripper, it relaxes to its original shape and releases the penny (Fig. 5.12c). When the temperature reaches  $T_H$ , the second muscle triggers the bistable mechanism in the reverse direction causing the robot to move backwards to its original delivery point (Fig. 5.12d). The principle of reverse propulsion can be easily extended to more complex trajectories and multiple cargoes.

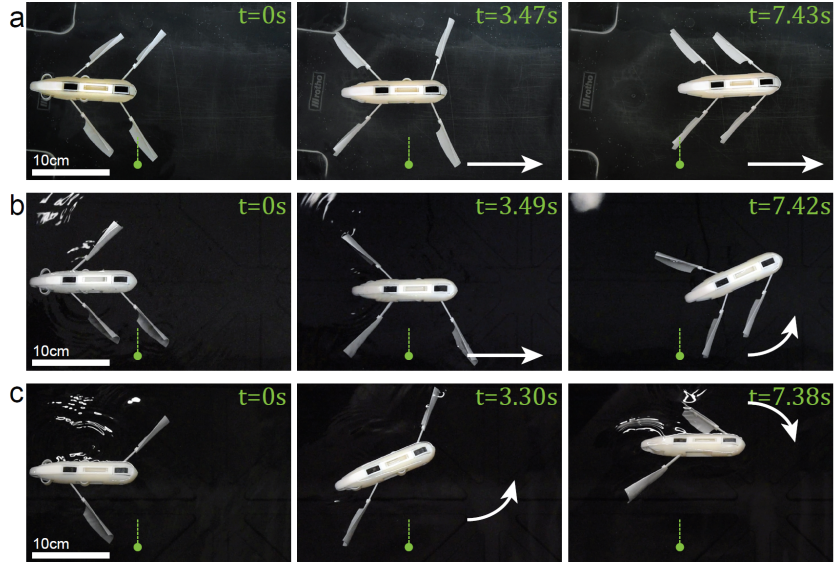


FIGURE 5.11: Sequential and directional propulsion showing three different paths that are achieved through placement of fins. a) Two forward motions are achieved by installing all four fins. b) One forward motion is followed by a left turn by removing one fin. c) Left turn is followed by a right turn by removing one fins.

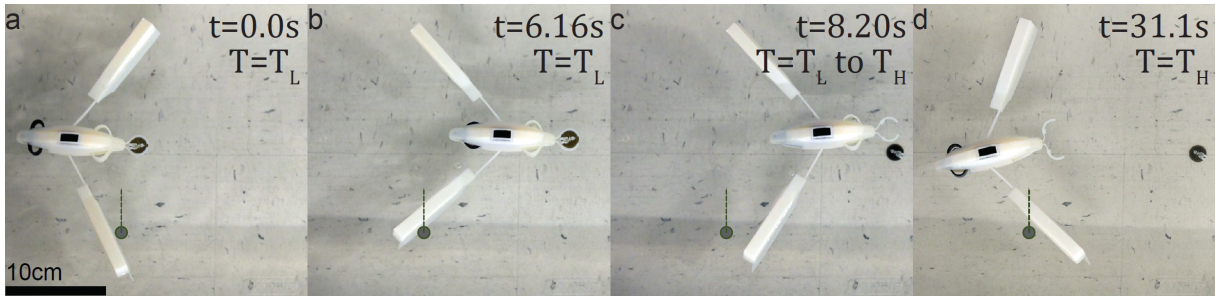


FIGURE 5.12: Video stills capturing the reversing swimming robot from a) delivery, to b) forward motion, to c) cargo delivery and to d) revering back to the starting position.

## 5.5 CONCLUSION

Propulsion requires an input of energy, and the transfer of that energy into mechanical energy. It must also ensure a net-forward motion in reversible designs [107]. Both are achieved by combining shape memory polymer and a bistable mechanism. When heated past its glass transition temperature, the shape memory polymer delivers a mechanical force needed to trigger bistability. The bistable mechanism moves from the higher energy state to the lower one, thereby releasing energy. The second requirement is achieved with the design of the fins and the asymmetry of the bistable mechanism.

Future improvements of this technology could include the use of pre-strained materials [80], reversible shape memory polymers (rSMPs) [108] or liquid crystal elastomers (LCEs) [6, 109] in the “muscles”. LCEs activated by light [109] or temperature variations [6], for example, could achieve cyclic actuation in response to diurnal/nocturnal cycles.

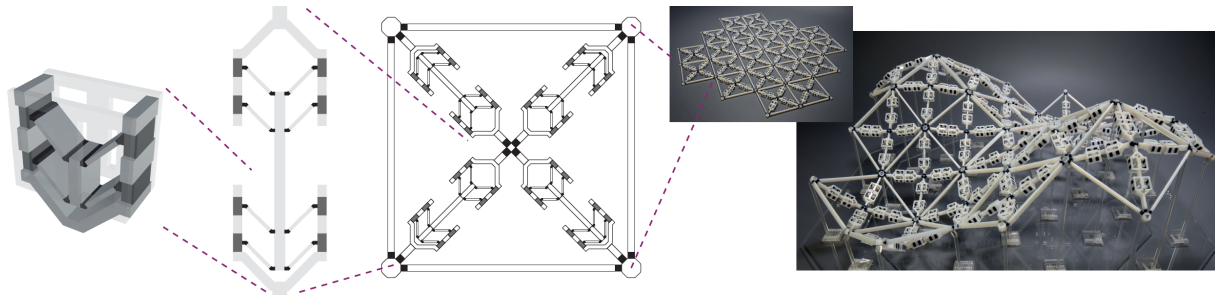


This work presents an a 3D-printable, swimming robot that requires neither complex on-board components nor a tether to achieve directional propulsion. Instead, programmed shape memory polymer muscles are used as the power supply, a bistable mechanism as the “engine”, and a set of fins as the propellers. By reacting to varying external temperature the robot can move forward, turn, reverse and/or deliver a cargo. At constant temperature, the robot response time can be controlled varying the geometry and material properties of both the bistable mechanisms and the shape memory strips. This demonstrates a first step in the realization of soft locomotive robots, potentially applicable in a variety of applications, such as navigation and delivery.





## GENERATIVE DESIGN OF MULTI-STABLE SURFACES



The content of this chapter is to be submitted,

Chen, T. & Shea, K., (2019), Generative design of multi-stable surfaces.

### 6.1 SUMMARY

A flat surface that can be reconfigured into given 3D target shapes is of great importance in numerous fields at different length scales, e.g. aeronautical systems, architectural installations, and targeted medicine delivery. Such a mechanical system is able to drastically reduce demands on fabrication and transportation, and enable precise controlled deployment. Given an arbitrary target shape, such an inverse problem is typically tackled by discretizing the target shape, then mapping each element to the flat surface. During the mapping process, either the periodicity or the internal properties of the elements are changed. As this is a geometric problem, the system is not necessarily mechanically stable when reconfigured into the target shape, i.e. when the means of reconfiguration is removed, the system will revert back to the flat shape. A method is proposed for the generation of flat surfaces that are able to be reconfigured into a number of target shapes, each of which are mechanically stable. First, the target shapes are discretized using a Chebyshev net. The resulting quadrilateral elements are mapped to a flat surface by accounting for their defects, or excesses in the internal angles. These are then accommodated by the lengthening or shortening of the added diagonal members. By embedding bistable elements into the diagonal members, the length change necessary is achieved while ensuring mechanical stability after the lengths are changed. Using a multi-material 3D printer, this method is demonstrated by fabricating one flat surface that reconfigures into two distinct and stable target shapes. The proposed method serves as a new direction for the design of reconfigurable systems. The combination of such systems with autonomous activation may enable complex, self-reconfiguration of surfaces.

## 6.2 INTRODUCTION

Deployable and reconfigurable systems have seen many applications at different scales in architecture, engineering, medicine, and other fields where geometrical and functional reconfiguration brings great benefits. Examples of such systems include temporary shelters, space solar panels, coronary stents and drug delivery mechanisms. This is done with the valid assumption that flat objects cost less to transport, and takes less time to fabricate. This in conjunction with recent advances in the field of additive manufacturing allow these generated designs to be fabricated physically at different length scales.

Numerous methods have been proposed for the inverse design of such systems within the field of origami, where a crease pattern is generated such that it can be folded to a target shape. Lang [110] introduced an optimization problem whereby given a stick figure, a novel crease pattern is generated. More applicable to folding of continuous surfaces where the dihedral angles are not necessarily  $2\pi$ , Tachi [111] introduced a tucking fold where excess material is folded under the visible surface. Recently, a regular Kirigami unit pattern is proposed [112, 113]. Using a periodic tiling of this pattern with internal topological variation, one is able to approximate a continuous curved surface. The patterns generated by some of these methods may be extremely difficult to fold, and the folded shapes may collapse due to the inherent bending stiffness of the substrate (e.g. paper).

Within the domain of reconfigurable surfaces, the generation of a flat sheet such that it can transform to the target surface is commonly referred to as an inverse problem. Aharoni et al. [114] proposed a recipe for generating a directional field for the fabrication of a flat nematic elastomer such that when heated, this flat sheet transforms into a target surface of revolution. The applicability to free-formed surfaces remain elusive. Garg et al. [115] generated an initial wire mesh and optimized its shape and density with respect to the target surface. This allows the wire mesh to be formed onto a target surface with less distortion. However, the forming process requires a rigid target surface for the wire mesh to be affixed to. Using a combination of selective auxeticity and gravity or pressure, Konakovic et al. [116, 117] designed auxetic sheets composed of rotating triangles that drape to achieve curvatures. The sheets collapse back to the flat shape with the removal of gravity or pressure. Using pneumatic pressure, Pikul et al. [25] generated rings of alternating stiff and compliant materials in order to give rise to non-zero Gaussian curvature when inflated. Due to the simple projection mapping, the selection of target surfaces is limited. Celli et al. [26] proposed non-period cutting pattern such that curvature is created when the sheet is tensioned.

Commonalities are identified in some of the recent work that aim to generate designs that transform to free-formed doubly curved surfaces. 1) Information is obtained from the target surface and mapped to a flat geometry. 2) There exists a basic unit cell topology that is repeated to form a flat surface. To achieve the target geometry, either the periodicity of the tiling or the parameter within each unit cell is optimized during mapping, i.e. the resulting design has no repeatable pattern. 3) The geometric change is embedded in the material and geometry. This greatly simplifies the actuation procedure. 4) The 3D geometry is not in mechanical

equilibrium, i.e. with the removal of the activation force (e.g. air pressure), the 3D geometry will return to its 2D shape.

This chapter proposes a computational method to generate a planar grid structure that is able to reconfigure to a number of target surfaces. The first three characteristics above are adopted, while this work improves on the last. The reconfiguration is achieved by changing the internal angles within each quadrilateral grid cell, knowing that the angles can directly control the Gaussian curvature of the grid [118]. The bistable mechanism proposed in Chapter 2 is used to affect the change in internal angles. With this method the following contributions are offered:

- Through the use of bistable mechanisms, static equilibrium is ensured once the target surface(s) are reached. The degree of transformation is encoded in the stroke length of each bistable mechanism.
- Activation force is needed only during reconfiguration and can be subsequently removed. The bistable mechanisms can be individually activated without causing internal stress.
- The design can be fabricated flat, thereby drastically reducing the time of fabrication as well as the cost of transportation.
- After deploying to the first target shape, the design can return to the flat configuration and subsequently reconfigure to a second target configuration.

First this chapter presents the generation method that translates a number of target surfaces to discrete grid meshes through the use of Chebyshev net. The embedment of the bistable mechanisms within the grid meshes is described. In the result and discussion, the generative method is applied to three target surfaces including a flat surface, an trigonometric doubly curved surface, and a free-formed surface of revolution.

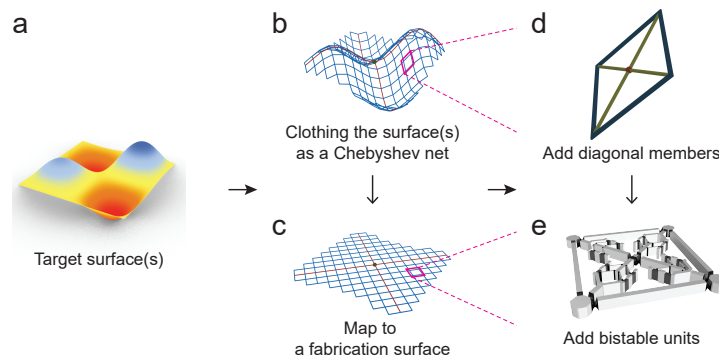


FIGURE 6.1: Steps in the proposed generation method. a) A target surface is given as an input, more than one surface may be accepted. b) A quadrilateral mesh called a Chebyshev net is generated for each target surface. c) The meshes are mapped to the surface for fabrication, which can be a flat surface. d) The mapping process is described per mesh element, a centroidal vertex and four diagonals are added. e) Length change of the diagonal elements between the target and the fabrication mesh are calculated. Bistable units are added to account for the length change.

### 6.3 METHOD AND DESIGN

Chapter 2 demonstrates the design and fabrication of flat structures which reconfigures into various doubly curved surfaces. These structures consist of grids of square unit modules. In each square module, there exists four equal length orthogonal edges. There also exists four diagonal members connecting each of the four vertices to the center point. Some of these diagonals may have bistable mechanisms. It is noted that in the unit modules, the length of the orthogonal edges remain invariant during reconfiguration. The quantities that change are the diagonal lengths through the activation of bistable mechanisms. By changing the diagonal lengths, the four internal angles of the unit module also change. This relationship between the curvature and the internal angles was formalized by Hazzidakis [118], who suggests that the Gaussian curvature of a quadrilateral can be controlled by the four angles of a quadrilateral.

Given at least two surfaces with one surface selected for fabrication, the method described in this chapter generates a reconfigurable structure that lies on this surface. The generated structure is able to be reversibly transformed into the other surface(s), denoted as target surface(s). The proposed method aims to derive the angle change in each grid element between the target surface(s) and the surface for fabrication, and use bistability to affect this change. The generation method (Fig. 6.1) is described in three steps: 1) the meshing of target surface(s) with quadrilaterals of the same edge length, creating a Chebyshev net for each target surface, 2) mapping the target meshes to surface for fabrication, which is potentially flat, 3) finally encoding each quadrilateral element of the mesh with the desired angle change.

#### 6.3.1 Meshing of the Surfaces as Chebyshev Nets

First the given surfaces are meshed using Chebyshev nets, which is a quadrilateral mesh with equal edge length. Chebyshev nets are commonly used to represent weaved fabric, where it was recognized that the shape conforming aspect of cloth comes from the local change in the angle between the weft and the warp fibers, and not the actual length of the fibers themselves which are assumed inextensible. The algorithm implemented here is adopted from Popov et al. [119] The algorithm starts by accepting as input, a set of surfaces  $S$ , consisting of one surface for fabrication and a number of target surface (Fig. 6.2). The meshing algorithm is performed on each surface  $S^i$  where  $i$  is the index of the particular surface,  $S^{i=0}$  is denoted as the surface for fabrication. For each surface  $i$ , a starting point  $p_{0,0}^i$  and two vectors  $u^i, v^i$  are given. The quantity shared between all  $S$  is the edge length  $L_e$ .

The starting points  $p_{0,0}^i$  and the two vectors  $(u^i, v^i)$  define a curvilinear coordinate system on  $S^i$  with four quadrants,  $[(u^i, v^i), (-u^i, v^i), (-u^i, -v^i), (u^i, -v^i)]$ . The meshing algorithm consists of two stages. Operations in the first stage (Fig. 6.2 a-c) are performed on the two opposing quadrants, i.e.  $q_1^i, q_3^i$  or  $q_2^i, q_4^i$ . Using  $q_1^i$  as an example, the first stage starts by finding equidistant points on the given surface along  $(u^i, v^i)$ . An iterative algorithm begins by drawing a circle of radius  $L_e$  with origin at  $p_{0,0}^i$  and normal to  $v^i$ . The point of intersection between this circle and  $S^i$  in the positive  $u^i$  direction becomes the next point  $p_{1,0}^i$ . The process repeats

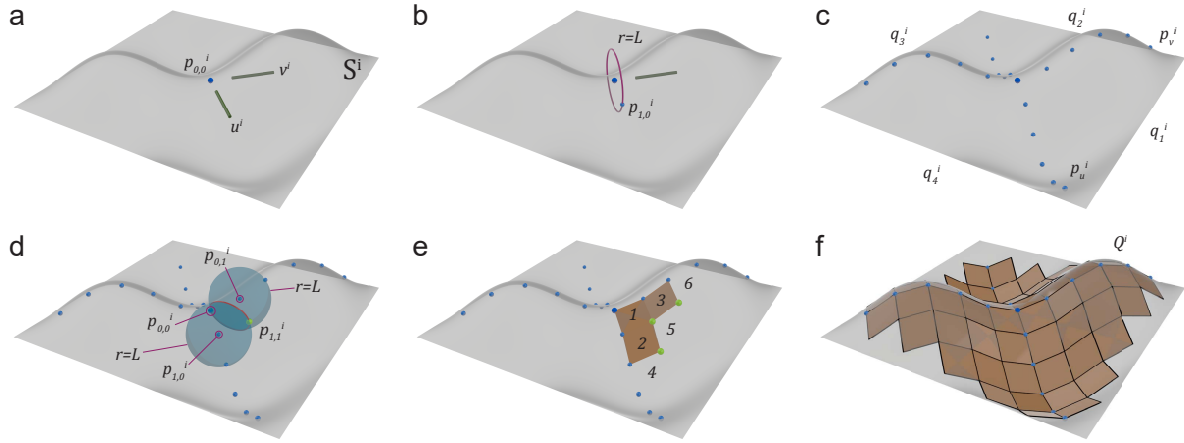


FIGURE 6.2: Meshing algorithm that generates a quadrilateral mesh per given surface with identical edge length. a) Given a target surface  $i$ , an initial point  $p_{0,0}^i$  and two vectors  $u^i, v^i$  are assigned. b) A circle with radius equaling to the edge length of the eventual mesh  $L_e$  to generate the next point along  $u$  and  $v$ . c) The initial sets of points are generated by drawing subsequent circles using previously generated points. d) The four quadrants are filled by intersecting two spheres. e) Subsequent points are found by diagonally iterate through each quadrant. f) A mesh  $Q^i$  is generated for each target surface  $S^i$ .

with  $p_{1,0}^i$  as the center of the circle. Prior to reaching an edge of the surface, the intersection will always result in two points beyond  $p_{0,0}^i$ . One of these two points already exists in the set  $p_u^i$  and is neglected. The iteration terminates when no new intersection point are found. The same operations are performed for circles normal to  $u^i$ , creating the set  $p_v^i$ .

Two assumptions are made in this part of the algorithm, 1) while  $u$  and  $v$  are not necessarily orthogonal, it is assumed that they are for our application, this ensures the quadrilaterals are squares in the flat configuration, 2) for our application, the surface is assumed to be open and bounded. In the case of a closed surface, the iteration must terminate at a predefined counter, and a subsequent stitching operation must be performed [115].

The second stage of the algorithm (Fig. 6.2d-f) uses these generated points to fill the space in each of the quadrants with non-planar quadrilaterals that have equal edge lengths. Using the first quadrant as an example again, starting from the origin, with three known vertices,  $[p_{0,0}^i, p_{1,0}^i, p_{0,1}^i]$ , and the surface  $S^i$ , a fourth point can be uniquely determined. First, two spheres of radius  $L_e$  are drawn with centers at  $p_{1,0}^i$  and  $p_{0,1}^i$ . The intersection between these two spheres is a circle that by definition passes through  $p_{0,0}^i$  and potentially another point on the surface. This point, if it exists, becomes the fourth vertex of the quadrilateral,  $p_{1,1}^i$ . This becomes a known vertex for the next iteration, which progresses diagonally outward until no further points can be found (i.e. the edge of the surface is reached). These operations are performed for each of the four quadrants. The resulting set of quadrilaterals constitutes the mesh of surface  $S^i$ . This mesh is denoted as  $Q^i$ .

### 6.3.2 Design of the Reconfigurable Structure

A set of meshes  $Q$  result from the above meshing operation for each surface in  $S$ . To allow reconfiguration between the surfaces, each quadrilateral must be uniquely mappable to all surfaces. The two stage meshing process, as opposed to a single stage spiraling generation process [119], allows a two stage set intersection procedure.

The first set intersection is performed prior to the second meshing stage. Since the cardinality of sets  $p_u^i, p_v^i$  must be identical for all surfaces or  $S^i$ s, the sets with greater number of elements than the minimum number of elements of all sets must have the additional elements truncated. The truncation is unique if origin,  $p_{0,0}^i$ , and the four quadrants are respected. This set intersection is particularly effective when given one target surface that is much larger than the other; it is computationally wasteful to fully mesh the larger surface. The second set intersection is performed after completing the meshing operation using the updated  $p_u^i, p_v^i$ . From the resulting sets of quadrilaterals, the final design is derived with a set intersection,  $\cap_i Q^i$ .

These two set intersection operations ensure that both the number of elements and the adjacency matrix is same for all  $Q$ s. For our application, a flat bounded surface is assigned as the surface for fabrication  $S^{i=0}$ . This flat surface is treated as another surface which the above algorithm is operated upon. It is sufficiently large such that the resulting set of quadrilaterals  $Q^{i=0}$  is a superset of all others in  $Q$ .

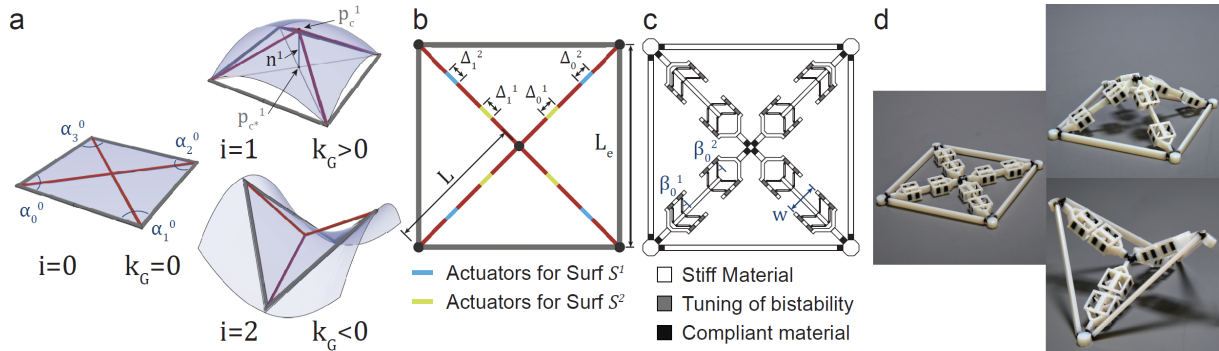


FIGURE 6.3: Embodiment design of a one element surface that reconfigures into two different surfaces. a) One element mesh of the surface for fabrication  $i = 0$ , a synclastic surface  $i = 1$  and an anticlastic surface  $i = 2$ . Both mesh edges and diagonal members are drawn. b) The change in length of the diagonal members necessary to reconfigure the flat surface to the target surfaces. c) The placement of the bistable mechanisms to affect these changes. d) Physical specimens of the flat element that reconfigures to both the synclastic and the anticlastic surface.

### 6.3.3 Design of the Quadrilateral Unit Module

Now with a set of quadrilateral meshes  $Q$  is generated with the mesh elements from one mesh is uniquely mappable to all the other meshes. For each mesh quadrilateral element, there are four internal angles  $\alpha_{0..3}^{i,j}$  for each mesh element  $j$  in  $Q^i$  for surface  $i$ . The reconfiguration between the surface for fabrication to the target surface is achieved by changing individually the



four sets of internal angles of the first surface to that of the second. The problem is further simplified by the assumption that between surface to surface reconfigurations, the flat configuration is always visited since this is the configuration in which the surface is fabricated. Therefore the angular change for each mesh element  $j$  is calculated as the difference between the  $\alpha_{0..3}^{i>0,j}$  and  $\alpha_{0..3}^{i=0,j}$ .

The mapping from the angle change to the embodiment design of each mesh element is illustrated using the example of a single element flat prototype that reconfigures between a purely positive to a purely negative Gaussian curvature surface (Fig. 6.3).

The first is a flat surface that is  $75 \times 75$  mm centered around the origin  $(0,0)$ . The initial point is  $(-37.5, -37.5)$  and the initial vectors are  $(1,0), (0,1)$ . The second and third surfaces are parametrized by Eq. 6.1 and 6.2 respectively. The amplitudes are  $A_1 = 8.25$  and  $A_2 = 10.5$ . The initial points for the second and third surfaces are  $(-37.5, -37.5)$  and  $(-40.55, 0)$  respectively. The initial vectors are  $(1,0), (0,1)$  and  $(1/\sqrt{2}, 1/\sqrt{2}), (-1/\sqrt{2}, 1/\sqrt{2})$ . Meshing is performed on the first quadrant. The edge length is  $L_e = 75$  mm.

$$z = -\frac{x^2 + y^2}{A_1^2} \quad x, y = [-37.5, 37.5] \quad (6.1)$$

$$z = \frac{x^2 - y^2}{A_2^2} \quad x, y = [-42.5, 42.5] \quad (6.2)$$

The superscript  $j$  is omitted since there is only one element. First a centroidal vertex,  $p_{c*}^i$  is found using the four corner vertices. Especially for a positively curved surface, this vertex may rest far from the actual surface. To reduce error, a surface normal,  $n^i$ , is defined using the four corner vertices and  $p_{c*}^i$  is projected along  $n^i$  to the surface. The intersection point  $p_c^i$  is defined as the center point. Four diagonal members are then constructed by connecting  $p_c^i$  and the four corner vertices. The procedure is not a part of the canonical Chebyshev net.

Shown in Chapter 2, it is shown that  $\alpha_{0..3}^i$  can be altered by changing the length of the diagonals of each quadrilateral. Since the opposing angles for every mesh element are equal, i.e.  $\alpha_0 = \alpha_2$  and  $\alpha_1 = \alpha_3$ , the length of the opposing diagonal members are also equal. Further, since  $u, v$  are assumed to be orthogonal, in the flat configuration  $\alpha_{0..3} = \pi$ . The difference in length of the diagonal members are calculated as  $\Delta_k^i = L_k^i - L_k^{i=0}$  for diagonals  $k = [0..3]$  where  $L_k^{i=0}$  is identically  $1/\sqrt{2}L_e$  (Fig. 6.3b).

For this example, there exists two target surfaces. Two bistable mechanisms are placed on each diagonal, leading to eight per mesh element, or four for each target surface. The stroke length refers to the total length change of each bistable mechanism, and is designed to equal  $\Delta_k^i$  where  $k = [0..3]$ . This is translated into the angle of inclination of the trusses within the bistable mechanisms,  $\beta = 2\Delta_k^i/w$  where  $w$  is the width of the bistable mechanism (Fig. 6.3c).

The absolute limit of  $\beta$  is from  $-1/2\pi$  to  $+1/2\pi$  where negative and positive  $\beta$  contracts and expands respectively when transformed. However, a more restricted range of  $\beta$  is defined to avoid self-contact due to finite thickness of the members and to ensure snap-through [17].





The minimum edge length  $L_e$  of the mesh is determined by the number of target surfaces and by the maximum and minimum  $\beta$  of the mesh of each target surface. Positive  $\beta$  require the least amount of space (Fig. 6.5), with the requirement increasing as  $\beta$  decreases. With additional target surfaces, one only needs to add more bistable mechanisms to each diagonal.

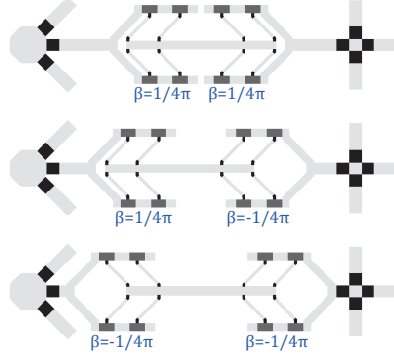


FIGURE 6.5: Placement of bistable mechanisms of different  $\beta$  values.

## 6.4 RESULTS AND DISCUSSION

### 6.4.1 Design and Fabrication of a Multi-stable Surface

Three surfaces are chosen to demonstrate the method from generation to fabrication. The first is a flat plane, which is used as the surface for fabrication. The second is a doubly curved surface formed by a trigonometric function parametrized by  $u, v = [-l, l]$  [4]. The third surface is defined by revolving a Nurbs curve around the vertical axis. The coordinates of the control points of the Nurbs curve are listed in Eq. 6.4. The overall dimension of target surfaces are identical. Due to fabrication constraints, i.e. minimum feature size and maximum enveloping dimensions, the physical prototype is limited to a grid of 6 by 6. The amplitude  $A = 64$  mm and the coordinates of the control points are chosen such that the maximum absolute value of the actuation angle  $\beta$  is below  $1/5\pi$ . To ensure the overall dimension of target surfaces are identical,  $l$  is set at 210 mm for both surfaces.

$$A \sin \frac{2\pi}{l} u \sin \frac{2\pi}{l} v \quad (6.3)$$

$$p_n^{0..6} = (0, 0.325l), (0.1l, 0.325l), (0.32l, 0.265l), \\ (0.5l, 0), (0.84l, 0), (0.96l, 0.20l), (1.1, 0.325l) \quad (6.4)$$

All three surfaces are meshed with the initial point being  $p_{0,0} = (0, 0, z)$  where  $z$  is found through vertically projecting the origin to the target surfaces. The initial mesh vectors with respective to the parametrization of the surfaces are  $u, v = (1/\sqrt{2}, 1/\sqrt{2}), (-1/\sqrt{2}, 1/\sqrt{2})$ . The mesh edge length  $L_e = 75$  mm is chosen to adequately represent the surface and provide sufficient space for the bistable mechanisms. The meshing algorithm generates 24 elements

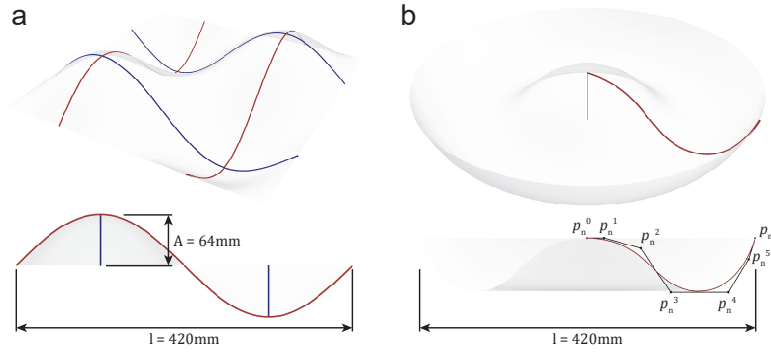


FIGURE 6.6: Parametrization of the two target surfaces.

for each surface after the set intersection operation between the individual meshes. The stroke length of each bistable mechanism is derived from the angle change of the internal angles of each element.

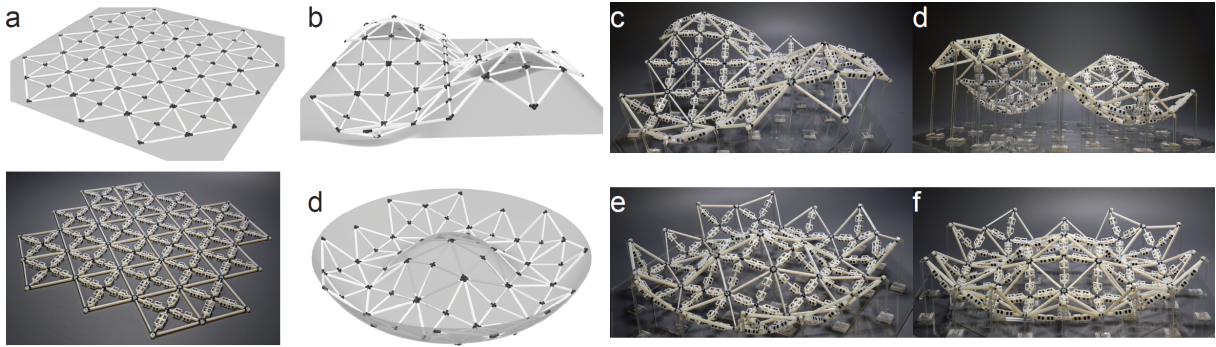


FIGURE 6.7: Demonstration of a reconfigurable structure from the flat surface to two unique target surfaces. a) The design and fabrication of the flat configuration. b,d) The model of the target surfaces  $i = 1$  and  $i = 2$  respectively. c,d,e,f) Photographs of the same flat surface reconfiguring to both target surfaces.

The reconfigurable surface is fabricated in four segments and connected using adhesives. The four segments are printed in six hours. They are submerged in the dissolving solution for eight hours and neutralized with an acid solution. They are then air dried for twelve hours. The supports are 3D printed using the same process but a translucent stiff material. They are fixed at the base to a laser cut sheet.

The edge members are dimensioned 2 by 4 mm. Compliant hinges are placed between the nodes and the edges. The nodes that are shared between the quadrants are printed twice but with half the depth such that they serve as points of connection between two segments. The center node is printed four times at quarter of the thickness as it is shared between all quadrants.

Kinematically, the structure reconfigures to each of two target surfaces while reaching self equilibrium, i.e. the structure is free from self-stress. However, since the design process does not specify boundary conditions, additional supports are needed depending on the application of the structure. Further, with the placement of the centroid node in each mesh element, additional DOFs are introduced. This results in two mechanisms for flat mesh elements, i.e. when the centroid is on the lines formed by the opposing vertices. Lastly, the bistable force is

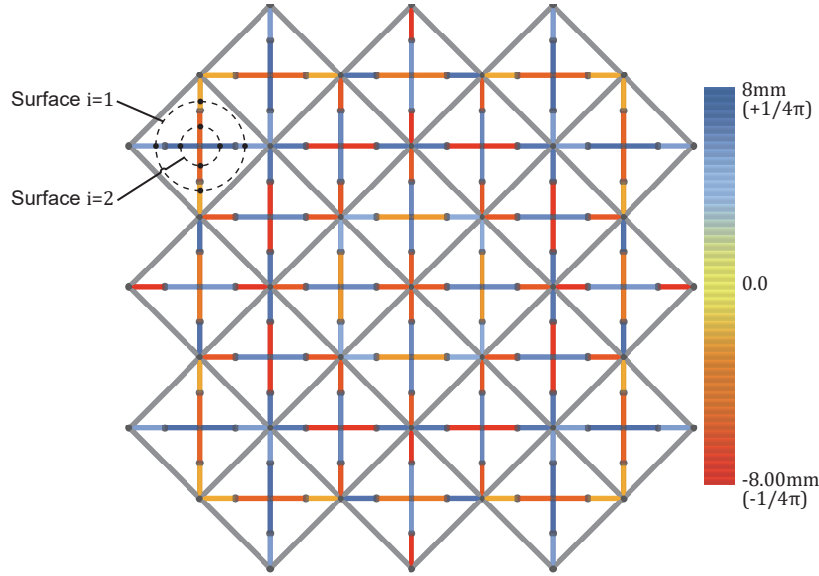


FIGURE 6.8: Design schematic showing both the rigid orthogonal members, and the degree of extension or contraction of the diagonal members. In each mesh element, the diagonal members are split in two, with the four further from the centroid color coded to show the bistability angle  $\beta$  for the first target surface. The four closer to the centroid refer to the second target surface.

dependent on the  $\beta$  angle, with a shallower angle resulting in a smaller triggering force [3]. Depending on the boundary conditions, this force may be overcome by the self-weight of the structure in the deployed configuration. For demonstration, supporting columns are added during deployment in locations typical of such reconfigurable structures. The results show remarkable similarity to the target surfaces as modeled (Fig. 6.7).

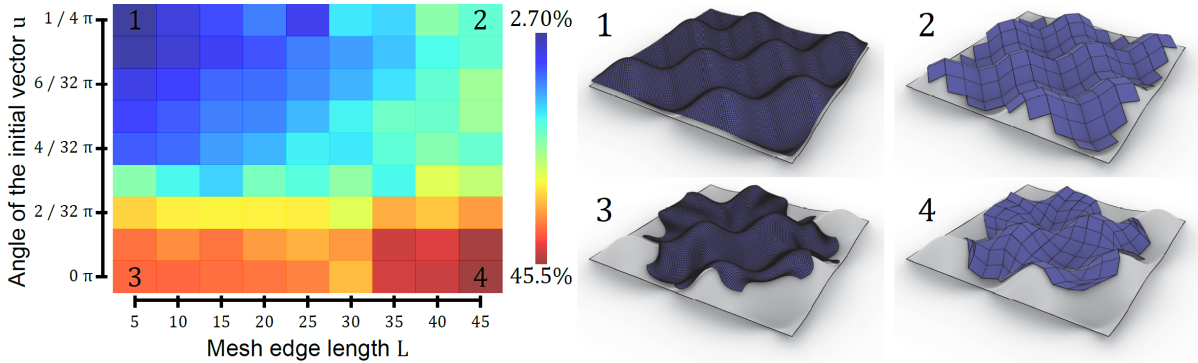


FIGURE 6.9: Mesh coverage error as influenced by the initial meshing vectors and the edge length of the mesh elements. The plot shows the initial vectors have a large influence over the coverage, whereas the edge length is influential mostly at the boundaries. Meshes 1-4 are indicated on the plot. The target surface is lowered for visualization.

#### 6.4.2 Meshing Sensitivity

Two types of errors are defined in the generation method. The first is the volumetric difference between the surface and the quadrilateral mesh of that surface. The second error is the differ-

ence between the surface area of the target surface and the area covered by its mesh. Note that this sensitivity study is computational in nature, as comparisons to the physical prototypes must account for extrinsic properties such as the load and boundary conditions.

Since all vertices of the mesh is guaranteed to be on the surface, the first error is calculated per element and summed. The element-wise error of the target surface is calculated by 1) deriving the normal at each vertex of each element, 2) cutting the target surface with the four planes drawn from neighboring pairs of normals and the flat plane that is constructed from the four vertices, 3) Summing the volume of resulting sections. Theoretically, the error could be minimized by vanishing  $L_e$ , as is the case in most woven fabric. However, the lower bound of  $L_e$  is define by the number of bistable mechanisms in each element and is limited by the fabrication method. With the introduction of the centroidal node in each element, the error is reduced by the volume of the tetrahedron formed from the centroid and the four vertices. This reduction is equivalent to increasing the mesh density by a factor of four. This is illustrated most clearly with a synclastic surface in Fig. 6.3a.

The second error is a result of the meshing algorithm. Here, a much larger surface is used as an example to study the influence of the initial vectors and the edge length  $L_e$  on the mesh coverage. The choice of such a surface largely eliminates the influence of boundaries. The vectors are measured by their angular deviation from the surface orthogonal direction from 0 to  $1/4\pi$ . The lengths studied are from 5 to 45 mm. It is shown that the choice of the initial vectors have a large influence on the coverage of the target surface 6.9. The influence of mesh density is less predominant. To improve the mesh coverage, and for more complex surfaces, a user assisted meshing tool can be adopted [115].

#### 6.4.3 Example of Encapsulation

One potential application for such a method is the design of encapsulation devices (Fig. 6.10). Using a sphere and a cylinder as the target surfaces, a similar reconfigurable flat structure is generated that is able to encapsulate both surfaces. For biomedical applications, a microscopic length scale is used. The edge length of the elements is set at 1.85 mm.

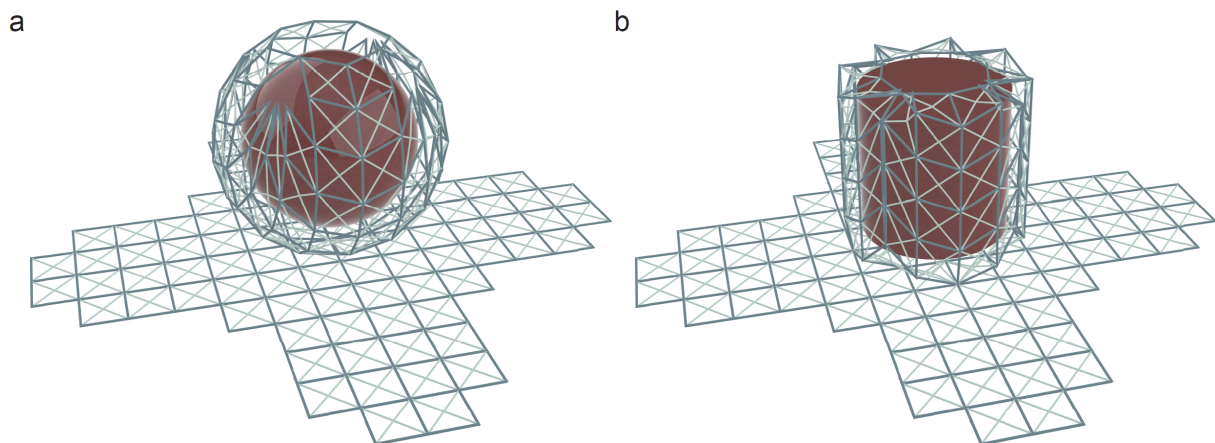


FIGURE 6.10: Design of an encapsulation device for a spherical object (a) and an cylindrical one (b).



#### 6.4.4 Example of Large Scale Structure

Similarly, the method is capable of generating large scale structures (Fig. 6.11). As an example, a mountain, the Matterhorn in Switzerland, is meshed using 34,000 elements with an edge length of 20 m to represent a structure with an envelop size of  $3 \times 3$  km. It is clear in this case, however, that structural considerations would dominate the design process. The bistable mechanisms at the base of the structure would experience significant compression.

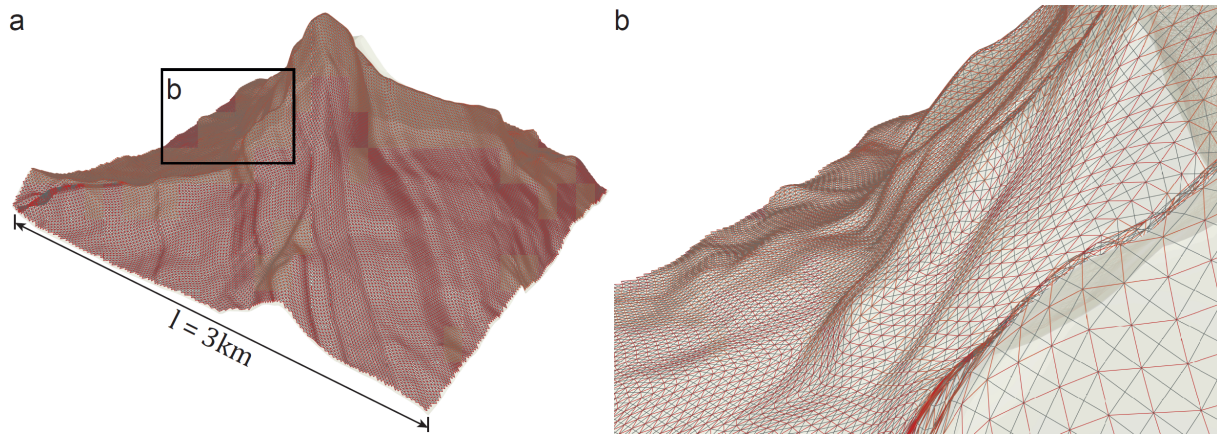


FIGURE 6.11: Design of a structure that reconfigures to the shape of a mountain.

## 6.5 CONCLUSION

This chapter demonstrates a solution to the inverse problem of designing a flat surface that can reconfigure to a number of target shapes while maintaining equilibrium. The proposed method first accepts a number of target surfaces, and meshes each using quadrilateral elements of the same edge length. By ensuring that each element in one mesh is directly mappable to a unique element in all the other meshes, the reconfiguration is done by changing the four internal angles of the elements in one mesh to the other. Bistable mechanisms are used to lengthen or shorten the diagonal members, which in turn change the internal angles. Since the stroke length of each bistable mechanism is derived from the angle change, as long as they trigger, the target surface will emerge. Furthermore, the use of bistability ensures that when the angle change is achieved, the system is in self-equilibrium.

The proof-of-concept example shows a mesh consisting of 24 elements that reconfigures to two target surfaces. For ease of fabrication and demonstration, the envelope size of the examples are  $420 \text{ mm}^2$ . However, the method can easily be adapted to micro-scale devices, as well as large scale constructions, as shown in Fig. 6.11. For such an example, it would be impossible to design by hand.

This method is able to generate a flat surface that can be reconfigured into a number of target surfaces. Comparing to fabricating the surface directly in the target shape, this drastically reduces the time of fabrication, material used, as well as the cost of transportation.

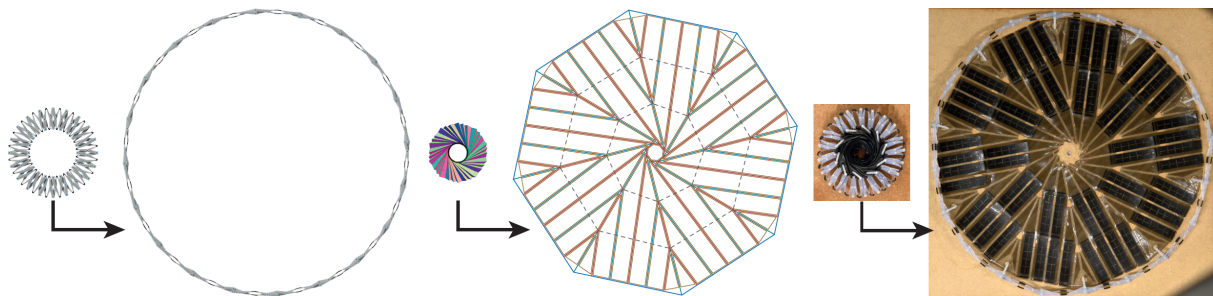
Through the use of bistable mechanisms, the configuration is guaranteed to be in static equilibrium once the target surface(s) are reached. In comparison with similar methods where the means of reconfiguration must always be present to maintain the target shape, in our design, the activation force is needed only during reconfiguration and can be subsequently removed. Furthermore, the bistable mechanisms can be individually activated without causing internal stress. After deploying to the first target shape, the design can return to the flat configuration and subsequently reconfigure to a second target configuration.

Moving beyond mechanical actuation of each bistable element, novel functional materials and fabrication techniques are developed to enable autonomous reconfiguration of the generated designs from 2D to 3D. One example could be the autonomous deployment of surfaces using shape memory polymers as the actuator (Chapter 4).



## SELF-DEPLOYING SOLAR PANELS

---



The content of this chapter is to be submitted,

Chen, T., Bilal, O. R., Lang, R., Daraio, C. & Shea, K., (2019), Autonomous deployment of a solar panel using an Elastic Origami and Distributed Shape Memory Polymer Actuators.

### 7.1 SUMMARY

Thus far, Shape Memory Polymers (SMPs) have been mostly used to achieve shape transformation, where through programming and relaxation, one is able to change an object from one shape to another. There has been few instances where SMPs are used in the reconfiguration of a mechanical system for functionality. In this chapter, I demonstrate the use of SMPs in a realistic mechanical system and illustrate the advantages that arise through autonomous transformation. In particular, I introduce the concept of robust functional transformation by embedding multi-functional SMPs in a distributed manner using the example of the deployment of a solar panel.

Traditional mechanical systems are comprised of an assembly of components, with each components designed to perform a particular function. In the space industry in particular, due to weight and volume restrictions, the mechanical systems have stringent and conflicting requirements. Solar panels are often used as a mean to provide power within a space system such as a satellite. The surface area of a solar panel therefore needs to be as large as possible to maximize power generation; yet during launch from earth's surface, the satellite must be confined within a given envelope. This led to the intricate stowage of passive modules, and sophisticated deployment using a network of motorized actuators. As a result, a significant portion of the stowed mass and volume are occupied by these support systems.

An autonomous solar panel array deployed using the inherent material behavior remains elusive. In this chapter, I improve the robustness and efficiency of solar panel deployment by

embedding SMP-based actuation within the structural elements of the system, i.e. materials under high temperature behave as actuators that transform the solar panel from the stowed to the deployed state, and under lower temperature, acts as stiff structural elements that support the solar panel. The system utilizes a network of shape memory polymer-based scissor mechanisms combined with an elastic “flasher” origami. The scissor mechanism is optimized to provide the maximum expansion ratio while delivering the necessary force. Its distributive nature allows one or two linkages to fail without causing failure in the deployment process. The origami substrate is also optimized to carry the maximum number of solar cells while still meeting space constraints. Folding of the “flasher” origami substrate shows a bifurcation behavior resulting in a cone shape and a disk shape in both simulation and experiments. A strategy is devised to avoid the undesired cone shape. The resulting design is entirely 3D printed, achieves an expansion ratio of 1000% in under 40 seconds, and shows excellent agreement with prediction both in the stowed and deployed states.

## 7.2 BACKGROUND

The surging demand for deployable mechanical systems is predominantly driven by the need to explore ever more inaccessible environments and to deliver increasingly large and complex payloads. Existing need for deployable systems includes space-based solar power[120, 121], geoengineering[122], antennas[123], and propulsion[124]. The design of these mechatronic systems largely considers the stowage of the payload[125] and the actuation which transform the payload from the stowed to the deployed state[126]. Traditionally, the actuation is achieved through a network of controlled actuators, which unpacks the passive payload. While numerous studies are behind done to ensure a robust stowage and deployment process, with ever more complex systems, autonomous large scale deployment, weight and volume of power supply, component jamming and failure, placement of the actuators, and control mechanism continue to challenge engineers.

The nascent field of programmable matter, where engineers integrate material and functionality[127] to create more reliable, adaptive and robust designs, is utilized here to address these challenges. Programmable matter refers to a material or a structure whose shape or stiffness can be controlled[128]. Numerous designs have started to demonstrate shape reconfiguration. For example, fabricating swelling hydrogel to create doubly curved surfaces[4] or flower petals[59], programming and activation of shape memory polymer to transform a sheet into a box[13] or to deploy a shape that was stowed in a cylinder[82] and transformable sheets using liquid crystal polymer[129] or printing pre-strain[130].

Functionalities beyond shape reconfiguration have also been demonstrated. Pneumatics has been used to actuate soft crawlers[21], robotic octopus[2], and transformable surfaces[25]. Negative Poisson’s ratio meta material has been used for vibration mitigation[131]. Electrical components have been embedded within the material itself to create soft electronics[132] and cardiac micro-physiological devices[133]. Instability has been used to create multi-stable structures without mechanical hinges[105], the actuation of soft directional swimmers[134], and

stable propagation of elastic energy[15]. While these works eliminate the need of a physical tether or rigid machineries, the active components are still being treated as separate entities that need to be embedded into a passive vessel. This complicates the design process and makes the system error prone. In contrast, biological systems often are multi-functional and truly self-reconfigurable. As an example, the leaves of Victoria water-lilies also serve as their own structural system (Fig. 7.1a,b).

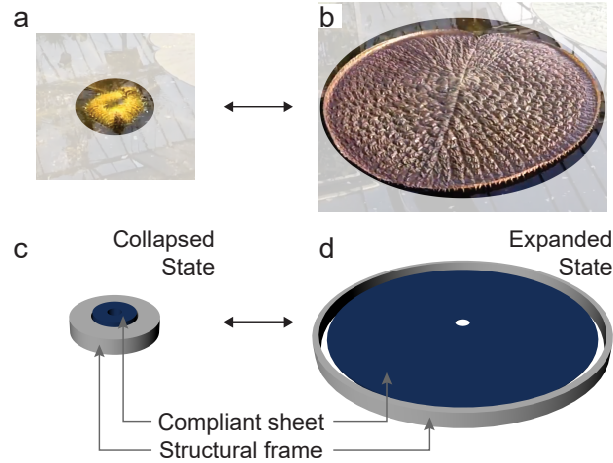


FIGURE 7.1: Autonomous deploying systems. a,b) The collapsed and expanded state of Victoria water-lilies leaves. Biological systems distribute actuation mechanisms within the material to create a robust and redundant structure. c,d) The schematic of the deployment strategy of the presented mechanical system. An outer ring acts as the primary actuation mechanism and structural support. An inner substrate forms the secondary actuation mechanism and provides the surface to carry the payload. Both components are fabricated using a shape memory polymer as the actuation mechanism.

Utilizing advanced manufacturing technologies, it becomes possible to embed and distribute sensing, control, actuation, and logic within the material itself rather than as discrete components in an assembly[135]. Using a self-deploying soft solar panel array as an example, I aim to demonstrate stable self-deployment through distributed actuation using the shape memory effect. The proposed mechanical system consists of an outer ring and an inner substrate (7.1c,d). The outer ring serves as the primary structural system and actuation mechanism. The inner substrate carries the payload and serves as the secondary actuation mechanism. In such a configuration, I show that the inner substrate fit entirely within the inevitable void of the collapsed outer ring.

To achieve a tunable expansion ratio, the outer ring adopts the design of the Hoberman Sphere where a series of scissor mechanisms in a ring configuration serves as the structural system and primary actuator. An elastic “Flasher” origami serves as a deployable surface and a secondary actuator. I pose the maximization of expansion ratio and the maximization of the number of fitted solar cells as discrete problems that are solved analytically considering only kinematics. The resulting mechanical system is able to achieve an area expansion ratio of ten, from approximately  $0.05$  to  $0.5 \text{ m}^2$ . The dynamics of folding the “Flasher” origami is studied in detail as a bifurcation behavior is observed in both simulation and experiments. It is shown that depending on the rate of folding, the origami folds into either a cone or a disk shape. As

a result, a rotational mechanism is devised for collapsing of the whole system into its stowed state.

For actuation, by distributing a shape memory polymer in both the Hoberman ring and in the origami substrate, I enable tuning of material stiffness by sensing the surrounding temperature. In both stowage and operating configurations where the temperature is lower than the glass transition temperature  $T_g$  of the polymer, both components contribute to the system's overall stiffness. During collapsing and deployment, sensing a temperature higher than  $T_g$ , the material reduces in stiffness by orders of magnitude and becomes compliant. In this example, collapsing to the stowed state is manual and programs a pre-strain in the shape memory polymers. The autonomous self-deployment occurs when the reduction in stiffness relaxes the pre-strain and reconfigures the system.

The method section describes the design of both the Hoberman ring and the elastic “flasher” origami, as well as the assembly of the two. The parametric optimizations considering dimensions and kinematics are detailed. In the results section, the mechanical behavior of the Hoberman ring and the folding dynamics of the origami are investigated. The deployment of the assembly is also shown. A discussion and conclusion follows.

### 7.3 METHOD AND DESIGN

The design of the autonomous self-deploying solar panel array is described in detail first through its components, i.e. the Hoberman ring, and the elastic “flasher” origami. Then the entire assembly is presented. The Hoberman ring is described in terms of its 1) mechanism and 2) analysis of its ratio of expansion. The elastic “Flasher” origami is then described with respect to the parametric optimization of the crease pattern.

#### 7.3.1 Hoberman Ring

The Hoberman Sphere[136] was initially patented by Hoberman before being popularized as a toy. It makes clever use of the classic scissor mechanism[137] to create a sphere-like object which can expand to several times its collapsed volume (Fig. 7.2a). Hubs are placed at the intersection of the scissors, and pins are used to enable the scissoring mechanism (Fig. 7.2b). I adopt the 2D version of this design to make an expanding planar mechanism, or the Hoberman ring (Fig. 7.2c).

The Hoberman sphere is created using a regular polyhedron as a base, similarly, the ring can be created using a regular polygon. I define the expansion ratio of the Hoberman ring as the change in area from the expanded to the compacted state  $\Delta A = A_{\text{expanded}} / A_{\text{collapsed}}$ . The area of each configuration is measured with the radius equally to the distance between the polygon center and the outer most vertex of the geometry.

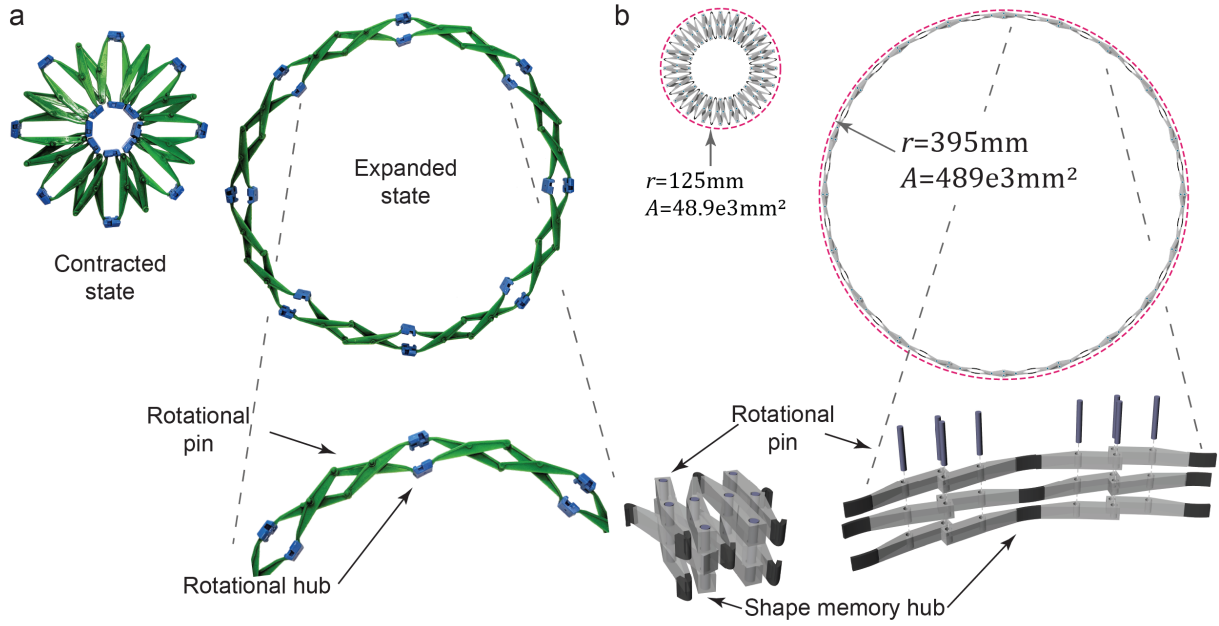


FIGURE 7.2: The design of the autonomous self-deploying Hoberman ring. a) A ring of the Hoberman Sphere toy in both collapsed and expanded state. b) Zoomed to show the mechanism with hubs and pins indicated. c) CAD model of the 3D printed Hoberman ring in both collapsed and expanded configurations showing 10 times change in area. d) Zoomed in render showing the shape memory polymer hubs and articulated pins.

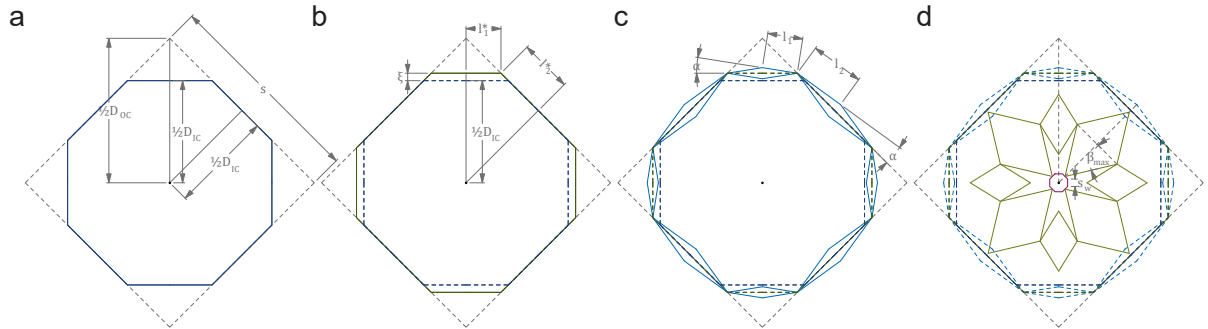


FIGURE 7.3: Parametric design of the Hoberman ring accounting for fabrication limitations and width of the members. a-d) The variables used in the derivation of the expansion ratio are shown.

Since the number of edges  $n$  of the initial polygon determines the expansion ratio of the mechanism given a set of physical and fabrication constraints, I set out to derive the analytical relationship between  $\Delta A$  in relation to  $n$ . Further, I introduce three variables to account for fabrication constraints (Fig. 7.3). Given the circumscribing diameter of the polygon,  $d_{OC}$ , as dictated by the maximum fabrication dimension, I calculate the edge length  $s$ , the inscribing diameter  $d_{IC}$ , the external angle  $\theta_{EA}$  and the internal angle  $\theta_{IA}$ .

$$s = d_{OC} \sin\left(\frac{\pi}{n}\right) ; d_{IC} = s \cot\left(\frac{\pi}{n}\right) \quad (7.1)$$

$$\theta_{EA} = \frac{2\pi}{n} ; \theta_{IA} = (n-2) \frac{\pi}{n} \quad (7.2)$$

I introduce an isogonal polygon with  $2n$  edges for the construction of the double scissor mechanism. The edges of this polygon is alternately grouped into two sets  $e_1$  and  $e_2$  with lengths  $l_1^*$  and  $l_2^*$  respectively. The perpendicular distance from the origin to edge set  $e_1$  is defined by varying the inscribing diameter  $d_{IC}$  with  $\zeta$  to create the isogonal polygon. Edge set  $e_2$  rests on the original regular polygon.

$$a = \frac{1}{2}d_{IC} + \zeta \quad (7.3)$$

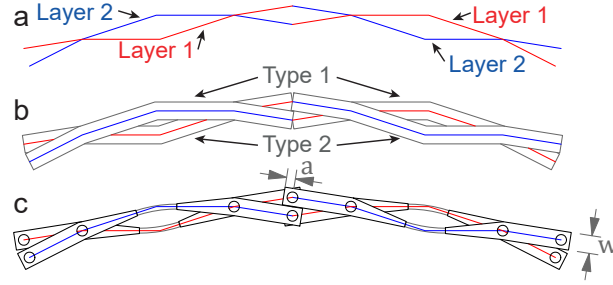


FIGURE 7.4: Detailed design of a scissor linkage mechanism. a) Blue and red lines indicate linkages on different layers. b) An outline is created using offset of width  $w$ , creating two different types of linkages. c) The ends of each linkage is extended by  $a$ . Where the linkages on the different layers intersect, a pin is added. The offset is thinned at the middle of the linkage, and a SMP strip is added at the middle of each linkage.

This is done such that the nominal length of scissors with pin ends are shorter than the one with hub ends. The pin ended scissors require an added length as a hole must be made at the end of the link, (Fig. 7.4), where as the hub is a flexible polymer which deforms. By adding  $\zeta$ , I can tailor the system such that the physical embodiment would be closer to equal length. Length of edge set  $e_1$  is then,

$$l_1^* = \left(\frac{1}{2}d_{OC} - a\right) \tan\left(\frac{\theta_{IA}}{2}\right) \quad (7.4)$$

To calculate the length of the edge set  $e_2$  I first calculate the two angles,  $\theta_1$  and  $\theta_2$ , formed by connecting the ends of each set of edges to the center,

$$\theta_1 = \tan^{-1}\left(\frac{l_1^*}{a}\right) \quad (7.5)$$

$$\theta_2 = \frac{1}{2}\theta_{EA} - \theta_1 \quad (7.6)$$

Then I find the length of edge set  $e_2$ ,

$$l_2^* = \tan(\theta_2) \frac{d_{IC}}{2} \quad (7.7)$$

Should there be an initial angle in the scissor mechanism  $\alpha$  so there is a bias, (Fig. 7.3b) the length of the half scissor is then  $l_1$  and  $l_2$ ,

$$l_1 = l_1^* \frac{1}{\cos(\alpha)} ; \quad l_2 = l_2^* \frac{1}{\cos(\alpha)} \quad (7.8)$$

Without losing generality, I assume  $\xi \geq 0$  since a negative  $\xi$  of the same magnitude would only mirror the structure. With this assumption, I see that  $l_1 < l_2$ . I define  $l = l_2$  and  $\theta = \theta_2$ . Here I introduce the dimension of the embodiment design to the consideration of the compacted ring. Assuming that the width of each scissor,  $w$ , equals to the edge length of a fictitious inner polygon of edge  $2n$ , and an inscribing diameter  $d_{IC,f}$ , then I can calculate an angle  $\beta_{\max}$  as the angle between two scissors in the compacted state.

$$d_{IC,f} = w \cot\left(\frac{\pi}{2n}\right) \quad (7.9)$$

Maximum angle of rotation between the scissors is therefore,

$$\beta_{\max} = \frac{\pi}{2} - \theta - \arcsin \frac{d_{IC,f} \sin(\theta)}{2l} \quad (7.10)$$

The expansion ratio  $\Delta A$  can thus be calculated and plotted (Fig. 7.3) for different  $w$ ,

$$\Delta A = \frac{[d_{IC} + 2 \sin(\alpha)l]^2}{[4l \sin(\beta_{\max}) + d_{IC,f}]^2} \quad (7.11)$$

The schematics (Fig. 7.5) show the geometric configuration of collapsed verses expanded rings for various  $n$ s assuming zero thickness  $w$  of the members. In this theoretical scenario, the inner vertices of the ring coincides at the center of the polygon [138, 139]. By introducing finite thickness, the inner vertices collide with each other as the ring collapses, forming an inner circular void. Quantitatively, it is observed that for a given  $w > 0$  with increasing  $n$ , the expansion ratio reaches a maximum. This maximum occurs with smaller  $n$  for larger values of  $w$  as the thickness of the members prevents the mechanism from collapsing to the center. With fabrication limitations, a thickness of  $w = 4$  is chosen as it is tested to be robust enough for repeated cycles of collapse-expansion. The maximum expansion ratio of  $\Delta A = 10.79$  is results for  $n = 20$ .

### 7.3.2 Elastic "Flasher" Origami

Origami has been studied extensively in the context of mechanical systems. ranging from the Miuri pattern [140], energy harvesting, negative Poisson's ratio and bistability [141]. In the case of rigid origami, the path of folding and unfolding can be predicted with precision [142]. This allows the mechanism to be actuated using motorized actuators or thrusters. Reconfigurable systems also benefit from the large volume change ratio of some origami patterns. In exist-



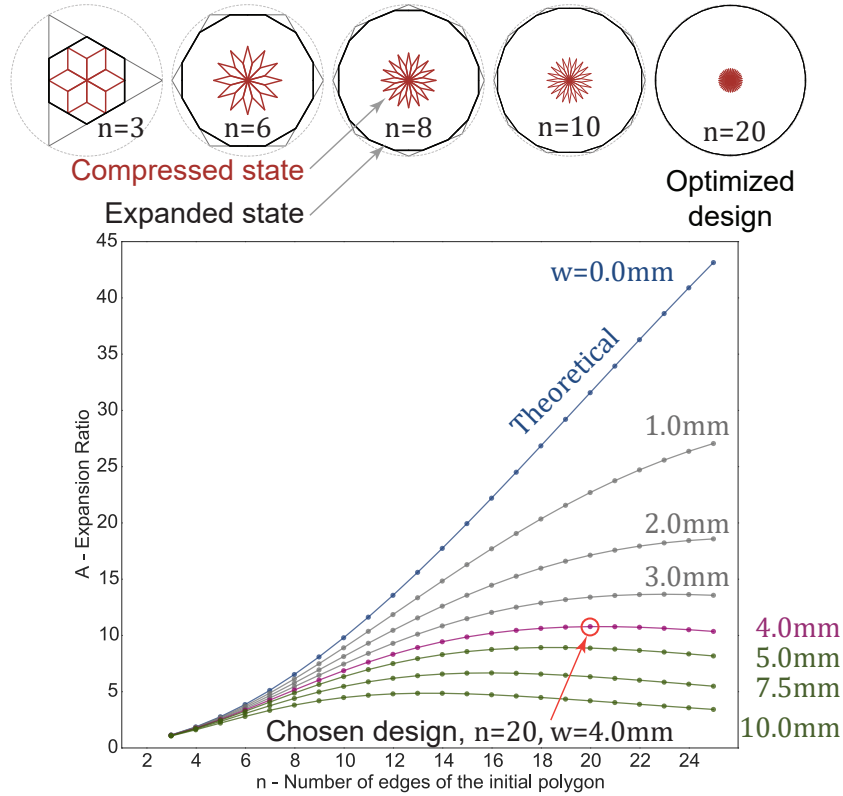


FIGURE 7.5: Parametric design of the Hoberman ring accounting for fabrication limitations and width of the members. Expansion ratio versus number of edges of the initial polygon are plotted for different member widths. It is shown that with the current fabrication method, specimens with  $w \geq 4$  are robust enough to undergo multiple expansion-collapsing cycles. For this width, the optimal expansion ratio occurs at  $n = 20$ .

ing deployable designs, the origami surface typically serves as the passive component that needs a motorized unfolding mechanism[124]. Indeed, while the concept of using a Hoberman like scissor mechanism to unfold panels has been proposed[143], the lack of mean of actuation or the space to store rigid panels remain unaddressed. There has been an increased interest in studying the mechanical response of origamis as it is realized that the tunability of mechanical response arise primarily from geometrical configuration. With the introduction of 4D printing, fold lines within an origami pattern could be programmed to self-fold[85]. This reconfigurability has recently been exploited in the design of acoustic waveguides[144], prismatic reconfigurable materials[145] and tunable thermal expansion meta-material[146].

To create a systematic collapse process, I adopt the “flasher” origami pattern (Fig. 7.6) [147]. This flat origami can be folded into a cylinder, where each arm of the “flasher” folds by wrapping around a common core. The mock up of the solar cells are printed on acetate which has comparable stiffness[148] and same dimension[149] to the encapsulation of commercially available flexible solar cells.

Numerous work has done on the deployability of rigid foldable versions of the “flasher”[122, 150]. Using similar terminology[150], the proposed flexible crease pattern can be categorized with two variables. First, the rotational order of the “flasher”  $n$  which is also the number of

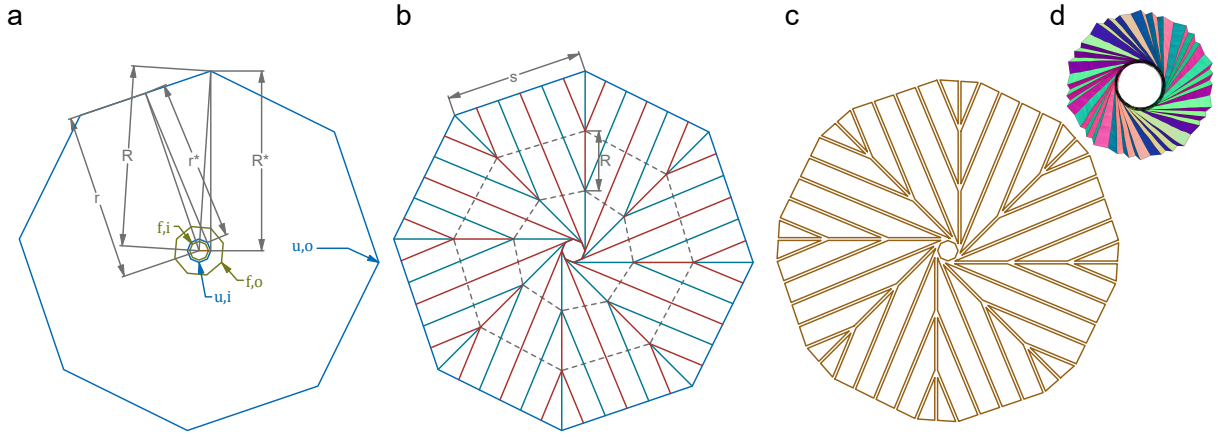


FIGURE 7.6: Elastic “Flasher” origami in both collapsed and expanded states. a) Variables used in the derivation of the constraint expressions. b) Crease pattern of the origami. c) Position of the origami panels, where the flexible solar cells are attached. d) The collapsed or folded state of the origami.

sides of the outer polygon. Second, the number of circumferential layers in the crease pattern,  $c$ . The panels are not physically discretized in the radial direction as the panel fold flexibly.

As the origami is intended to serve as a substrate, I optimize the crease pattern to fit the maximum number of solar cells of a given size. While flexible solar cells can bend to a certain curvature, if they are placed across folding lines, they would increase the folding resistance and potentially break during folding. Therefore, they are only placed on panels. In the generation of the fold pattern, the thickness of the panels is neglected, and allow them to be straight to better accommodate the rectangular solar cells. The strain during folding is assumed to be accommodated by the elastic substrate. The optimization problem is stated in Eq. 7.12, where the number of solar cells that can fit within a given pattern is maximized. Constraints to this problem are as follows, g1) the outer dimension of the unfolded and folded origami must fit within the expanded and collapsed Hoberman ring respectively, and g2) Each panel of the crease pattern be at least as wide as a given solar cell plus the width of the fold lines.

$$\underset{c,n}{\text{minimize}} \quad -\max[p(c,n), 0]$$

where

$$p(c,n) = \text{floor} \left[ \sum_{i=1}^c \left[ r_{u,o} - \frac{w_{PV} + h_f(i-1)}{\tan(\pi/n)} \right] \right] \quad (7.12)$$

subject to

$$r_{f,o} - r_{\max} \leq 0$$

$$w_{PV} - h_f \leq 0$$

Where  $r_{u,o}$  and  $r_{f,o}$  are the inscribed radii of the outer polygon in the unfolded and folded state respectively,  $w_{PV}$  is the smaller dimension of a rectangular solar cell,  $h_f$  is the height of the origami in the folded state,  $r_{\max}$  is the inner void space of the Hoberman ring.

Here the analytical expression is derived for the two constraints using the variables indicated in Fig. 7.6. Given two concentric polygons of  $n$  sides, the outer polygon is rotated such that the edges of the inner polygon if extended outward, bisects the edges of the outer polygon. This defines the outer and inner limits of the unfolded pattern. Two other polygons of  $n$  sides are used to define the outer and the inner limits of the folded pattern. The circumscribing radius, inscribing radius, and edge length is denoted as  $R$ ,  $r$ , and  $s$  respectively.

The superscript  $*$  refers to two outer polygon offset by the asymmetry of the origami pattern, the relationship between the offset quantities is as follows,

$$R_{u,o} = (R_{u,o}^{*2} + R_{u,i}^2)^{\frac{1}{2}} \quad (7.13)$$

These four polygons are denoted with subscripts  $u,o$ ,  $f,o$ ,  $u,i$ ,  $f,i$  referring to unfolded outer, folded outer, unfolded inner, and folded inner respectively. The known quantities are  $R_{f,i}$ ,  $R_{u,o}^*$ ,  $R_{u,i}$ .

I define the radius of the folded geometry,  $R_{f,o}$ , as  $R_{u,i}$  plus the number of wrapped layers,  $p$ . The variables  $c$  and  $t$  refers to the number of levels in the “flasher” pattern, and the thickness of origami sheet respectively.

$$R_{f,o} = R_{f,i} + p(2ct) \quad (7.14)$$

The number of edges each triangle of the outer polygon can wrap around the inner polygon is calculated as ratio between the inscribed radius of the unfolded geometry and the edge length of the folded geometry,  $S_{f,o}$ . Note that this edge length increases as more layers are wrapped and the radius increases.

$$p = \frac{r_{u,o}^*}{S_{f,o}} \quad (7.15)$$

The inscribed radius is  $r_{u,o} = R_{u,o} \cos \frac{\pi}{n}$  and the edge length is  $s_{u,o} = 2R_{u,o} \sin \frac{\pi}{n}$ . Similarly, I calculate the edge lengths  $s_{f,i}$ ,  $s_{u,i}$ , and the inscribed radius of the inner polygon  $r_{u,i}$ . The offset inscribed radius is calculated,

$$r_{u,o}^* = (r_{u,o}^2 - r_{u,i}^2)^{\frac{1}{2}} - \frac{s_{u,i}}{2} \quad (7.16)$$

and the edge length of the folded polygon follows,

$$s_{f,o} = 2R_{f,o} \sin\left(\frac{\pi}{n}\right) \quad (7.17)$$

The variable  $R_{f,o}$  is solved to form  $g_2$  constraint in Figure 7.7.

$$\begin{aligned}
R_{f,o} = & \left\{ \sqrt{\sin\left(\frac{\pi}{n}\right) \left( -4ct \sin\left(\frac{\pi}{n}\right) R_{u,i} + 4ct \sqrt{\left(\cos\left(\frac{\pi}{n}\right)\right)^2 R_{u,o}^{*2} + \sin\left(\frac{\pi}{n}\right) R_{f,i}^2} \right) R_{f,i}} \right. \\
& + 2ct \sqrt{\left(\cos\left(\frac{\pi}{n}\right)\right)^2 R_{u,o}^{*2} + (-2ct R_{u,i} + R_{f,i}) \sin\left(\frac{\pi}{n}\right)} \left. \right\} \\
& \left\{ R_{f,i} \sin\left(\frac{\pi}{n}\right) \right. \\
& + \left. \sqrt{\sin\left(\frac{\pi}{n}\right) \left( -4ct \sin\left(\frac{\pi}{n}\right) R_{u,i} + 4ct \sqrt{\left(\cos\left(\frac{\pi}{n}\right)\right)^2 R_{u,o}^{*2} + \sin\left(\frac{\pi}{n}\right) R_{f,i}^2} \right)} \right\}^{-1}
\end{aligned} \tag{7.18}$$

The first constraint requires the height of the folded origami to be greater than the smaller dimension of the PV cell. The height is simply the edge length of the unfolded polygon divided by twice number of layers in the “flasher”. Both constraints are shown in Fig. 7.7.

$$h_f = \frac{\sqrt{R_{u,i}^2 + R_{u,o}^{*2}}}{c} \sin\left(\frac{\pi}{n}\right) \tag{7.19}$$

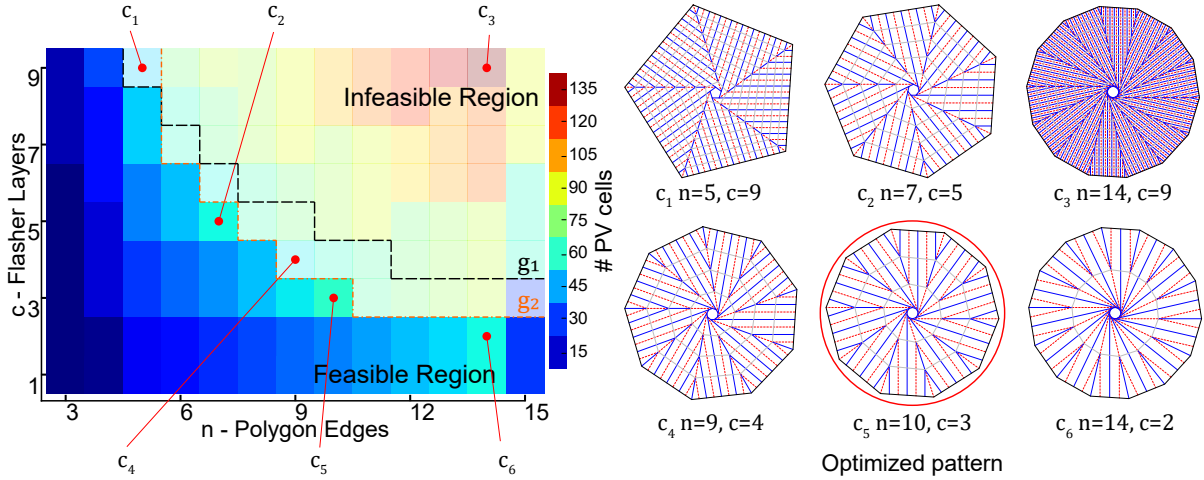


FIGURE 7.7: Maximizing the number of flexible solar cells by changing the “Flasher” origami crease pattern. Two variables,  $n$  - number of edges in the pattern’s outer polygon,  $c$  - number of radial layers in the pattern, are optimized to fit the largest number of solar cells of a given dimension. The contour plot shows the number of solar cells that can fit for every pair of  $(n, c)$ . Two constraints are imposed to 1) ensure solar cells can fit width-wise within a single panel of the pattern, and 2) the outer diameter of the folded origami can fit within the inner diameter of the collapsed Hoberman ring. Preferences are given to patterns which can construct periodic linkages to the Hoberman ring.

The feasible region of the objective landscape (Fig. 7.7) show optimized solutions of 60 solar cells at  $(n, c) = (7, 5), (10, 3), (14, 1), (14, 2)$ . As expected, as the number of rotational order  $n$  increase, more solar cells can be fitted. The constraints however dictate that beyond a certain  $n$  or  $c$ , the folded dimension  $r_{f,o}$  exceeds that of the inner dimension of the Hoberman ring  $r_{\max}$ . The adopted solution is a decagon ( $n = 10$ ) with three layers ( $c = 3$ ). This design is adopted

because  $n = 10$  is a fraction of the number of scissor mechanisms in the Hoberman ring. In this way, periodic connections can be made between the two.

### 7.3.3 Solar Panel: Fabrication and Assembly

While the entire design can be fabricated in one piece, for demonstration, the Hoberman ring and the elastic origami are fabricated separately using the Polyjet 3D printer. The Hoberman ring is fabricated with three layers of scissor mechanisms, e.g. two blue and one red layer (Fig. 7.4). An odd number of layers is required to have symmetrical out-of-plane behavior, and three layers is shown to provide sufficient force of expansion. Each layer consists of ten type I and II linkages each that are fabricated separately. Each linkage is 5 mm. A total of 80 pins are fabricated. The SMP within each linkage is 1.1 mm thick, and has an arc length of 9.14 mm. The stiff parts of the linkages are fabricated using VeroClear, and the SMPs are fabricated using FLX9895 (a digital mix between VeroClear and TangoBlackPlus).

The origami is fabricated in two piece with two types of layers. The base layer and the panel layer are 0.15 mm and 0.24 mm in thickness respectively. The thickness of the panels provides structural rigidity during the initial folding process yet is compliant enough to be wound around the center. The gap between the panels form the lines of fold. The gap width is greater than  $2t$  where  $t$  is the thickness of the panel. Due to the inherent elasticity of the material in the rubbery state, both mountain and valley crease lines are assigned the same width. Voids are placed at intersection of multiple crease lines to reduce stress concentration. Ten hooks are fabricated to connect the Hoberman ring with the elastic origami (Fig. 7.8). The origami substrate is fabricated using FLX9895. VeroClear stiffeners is added to points of connection to ensure the substrate does not tear.

## 7.4 RESULTS AND DISCUSSION

### 7.4.1 Hoberman Ring

Inspired by numerous work which converts pure mechanisms into mechanical metamaterials[151], autonomous expansion within the ring is enabled by replacing the hubs with shape memory polymers as actuators. The shape memory hubs have two polymer states, glassy or rubbery, depending on whether it is above or below its glass transition temperature  $T_g$ . At a temperature above  $T_g$ , it is able to be programmed to a second shape. If held in this shape while cooled down, this strain is “locked-in”. When reheated past  $T_g$ , the shape memory hubs relax this pre-strain and consequently deploy the structure.

The radial pressure required during collapsing and exerted during expansion can be predicted by understanding the force displacement behavior of the shape memory hubs. It is known that the recovery force is dependent on the dimension of the shape memory material, strain rate, and the ambient temperature[82]. Compression experiments are done to a seg-

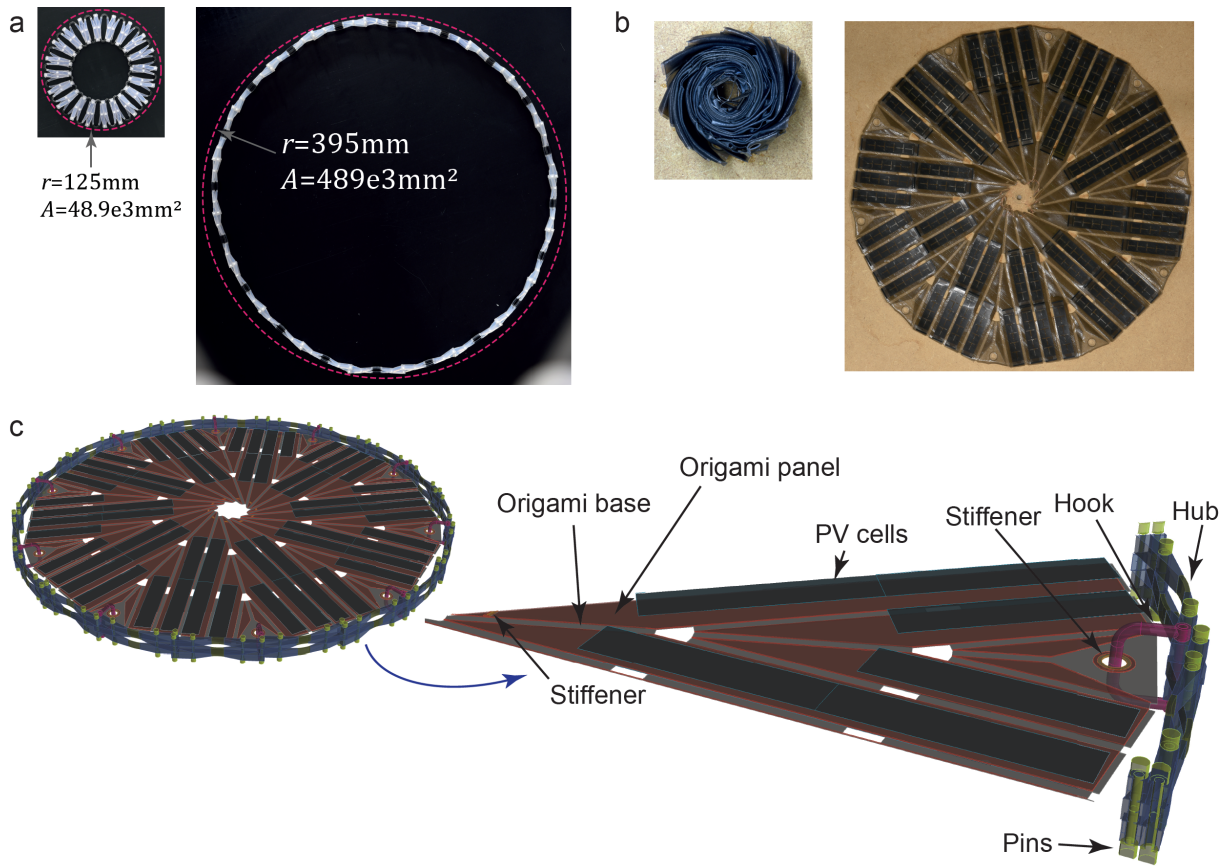


FIGURE 7.8: Fabricated components of the solar panel, as well as the assembly schematic. a) The Hoberman ring showing a ten-fold area change. b) The folded and unfolded "flasher" origami. The mock-up of flexible solar cells are attached. c. Assembly schematic between the two components.

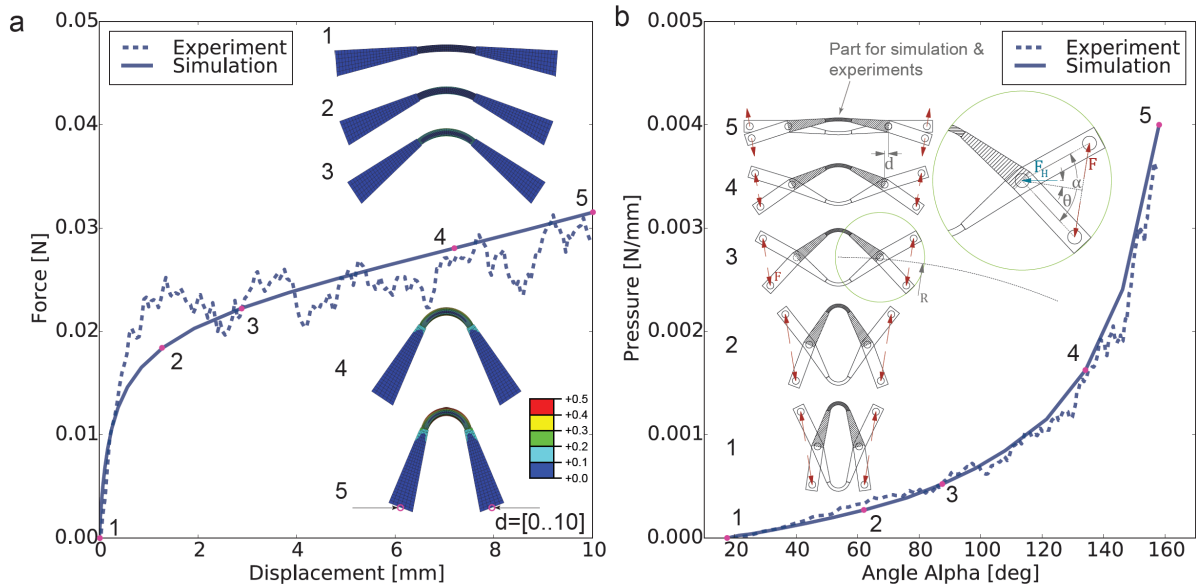


FIGURE 7.9: Mechanics of the shape memory hubs and the relationship with the radial pressure of the Hoberman ring. a) Force displacement plot of a single Shape memory hub from experimental and simulation. b) Overall pressure produced by all the shape memory joints of a  $n = 20$  Hoberman ring as a function of the angle between the scissor mechanism.



ment of the Hoberman ring under temperature  $T > T_g$ . 10 mm of displacement is prescribed to both sides of the segment at a rate of  $0.5 \text{ mm s}^{-1}$ . The ends of the segment are pin-connected to the compression plates. The reaction forces are recorded. Due to the small forces exerted by each shape memory hub, six are used to obtain less noisy measurements. A load cell with maximum load of 250 N is used, the measurement error is  $\pm 0.005\%$  or  $\pm 0.00125 \text{ N}$ . The same geometry is simulated using finite element analysis. The shape memory hub is meshed using a linear viscoelastic constitutive model[105] and deformed with a prescribed displacement  $d = [0..10]$ . The shape memory hub exhibits a non-linear force displacement behavior (Fig. 7.9a) as it bends in both experiments and simulations. The results are comparable despite the noise introduced due to the low force output.

The radial pressure is calculated with trigonometry (Fig. 7.9b). As  $F_H$  is horizontal at all stages of loading, the force in the radial direction depend only on the angle  $\alpha$ . The angle  $\alpha$  is empirically measured from the expanded to the collapsed configuration and plot against the radial pressure (Eq. 7.20), where  $n$  is the the number of polygon edge and  $R_{\text{exp}}$  is the outer radius. This pressure overcomes friction at the pins, and between the system and the ground.

$$p = F_H \frac{n}{2\pi R_{\text{exp}}} \frac{\tan(\alpha)}{\cos(\frac{\pi}{n})} \quad (7.20)$$

#### 7.4.2 Elastic “Flasher” Origami

For programming of the origami and consequently of the whole assembly, the strategy is to apply a rotation at the center while keeping the mountain and valley fold lines of the origami in the correct half plane(i.e.  $z > 0$  and  $z < 0$ )[152]. To apply this rotation, flexible wires are connected between the inner most vertices of the origami and a common rotational core. It is noted that during folding, the center may “pop” out of plane, forcing the whole origami to irreversibly assume a cone-like shape. To better understand this phenomenon, the folding process is simulated by assuming the crease pattern is an edge-node network. The coordinates of the nodes are solved such that there is minimal axial strain along the bars, and that the dihedral fold angle between all crease lines equal to a prescribed value  $\theta$ [153]. By incrementing  $\theta$ , a pseudo-dynamic folding simulation is achieved. As this method is used for rigid origamis, the panels of the “flasher” in the radial direction are finely segmented to mimic a flexible behavior. The error is then the elastic energy originated from strain within the bars, as this strain reflects stretching or compression of the panels. A bifurcation behavior is observed, i.e. two different heights can be achieved from the same fold angle(Fig. 7.10a,  $c_{1-5}$  and  $d_{1-5}$ ). The cone shape is triggered if the change in folding angle is small between two pseudo time steps, and disc shape is triggered if the change is large. I see that the strain energy or the error is much larger for smaller fold angles for the disc than it is for the cone. This correlation inverses at a larger fold angle(Fig. 7.10b). This explains the center of the origami “popping-up” during folding, and is resolved by holding the center core down and folding in shallow water to minimize buoyancy.



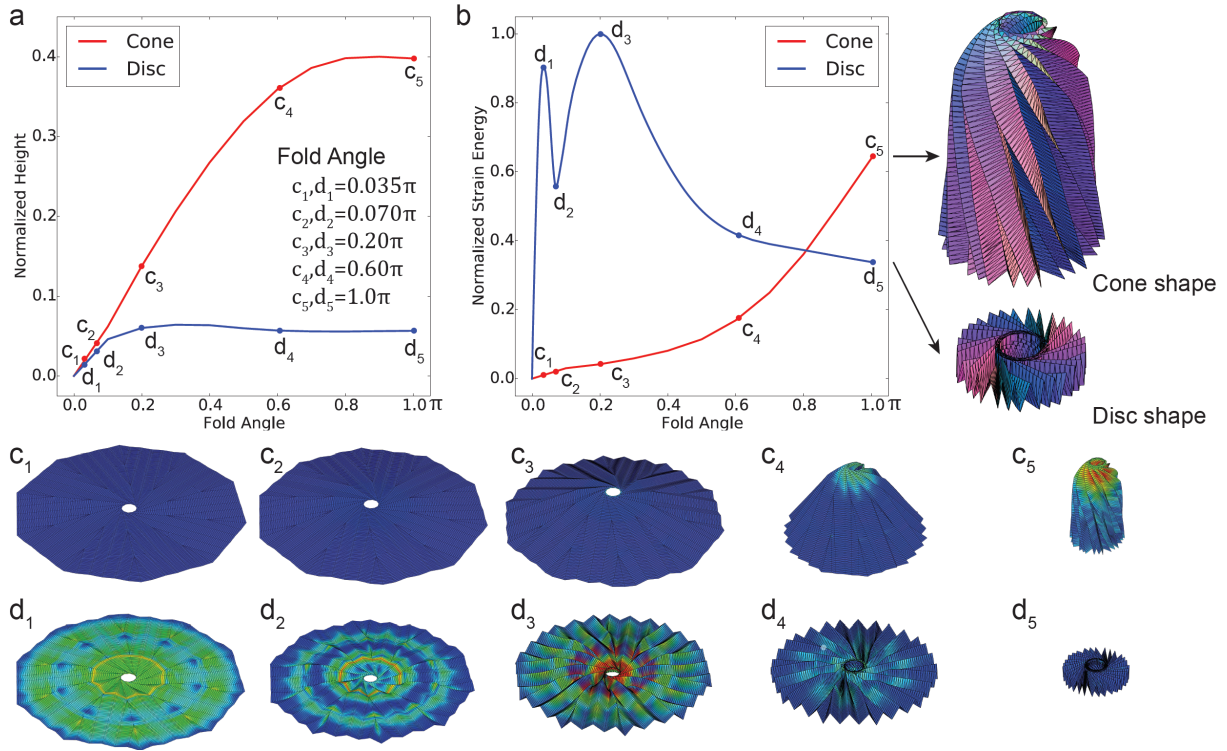


FIGURE 7.10: Bifurcation during folding of the “Flasher” origami as explained by the elastic energy within the fold lines. Two distinct folded shapes are observed during folding both in experiment and in simulation. a) Plot of total height of the origami verses percentage of fold angle (i.e. 0 to  $\pi$ ). b) Plot of total elastic energy verses percentage of fold angle. c) Simulated folded shapes (i.e.  $\alpha = \pi$ ) resulting in either a cone, or a disc.

#### 7.4.3 Solar Panel

While both components have been programmed individually for demonstration (Fig. 7.8a and Fig. 7.8b), the assembly is programmed in one step under an heated environment ( $T \geq T_g$ ) by one person. The collapse starts by rotating the core which the panels are connected to. As this core rotates, the whole geometry is pulled in and wrapped. This is assisted by the fact that the Hoberman ring has a Poisson’s ratio of  $-1$  at all strains. Then a cylindrical mold that would give the desired compacting ratio is used to demonstrate that the collapsed design can fit within a given geometry. While confined in this mold, the compacted design is cooled to the stowing temperature (Fig. 7.11a). The mold is then removed.

To deploy the design, the solar panel array is submerged in an environment heated past  $T_g$ . It is deployed under water to simulate a reduced gravity environment. First a rapid rotational motion is observed, where the deployment is largely initiated by the origami itself. At a certain stage, the rotation stops and the remaining folds are flattened by the Hoberman ring (Fig. 7.11b). This deployment behavior mimics a proposed two-stage mechanized deployment of a solar sail, Mori *et al.* [124] yet requires no actuators or power supply.

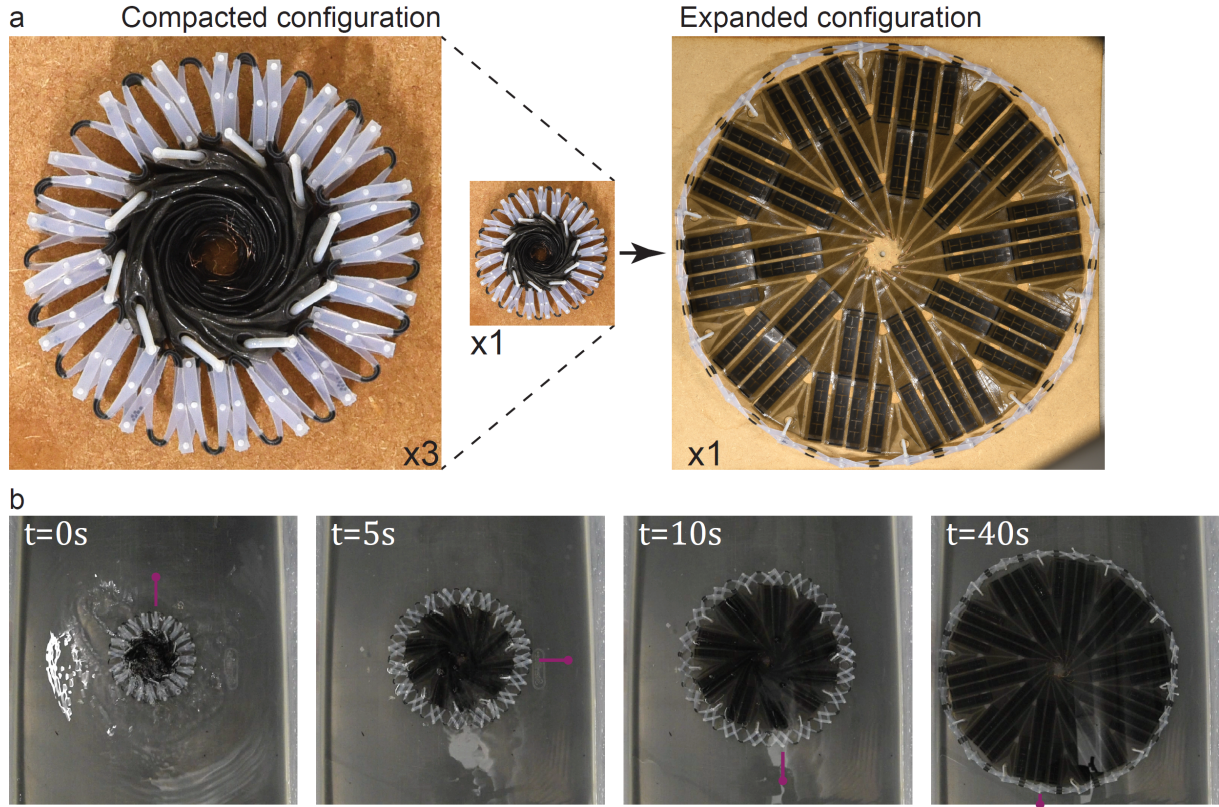


FIGURE 7.11: The autonomous deploying solar panel array. b) Photos showing the compacted and the expanded configuration of the PV array. b) Video frames of the deployment process under water above  $T_g$

## 7.5 CONCLUSION

The large area expansion capability of the Hoberman ring is exploited to autonomously deploy an array of flexible solar cells mounted on an elastic “flasher” origami substrate. The design of the system is done by analyzing the Hoberman ring and the “flasher” origami separately. First I propose to replace the rotational hubs of the Hoberman ring with shape memory polymers to enable autonomous deployment. I then parametrize and optimize the expansion ratio of the Hoberman ring assuming rigid behavior. Lastly, the mechanics of collapse and expansion of a single shape memory hub is analyzed. Through this, I am able to represent the autonomous Hoberman ring as a system that produce a mechanical overpressure.

The analysis of the “flasher” origami begins by parameterizing and optimizing the crease pattern to accommodate the largest number of solar panels while still fitting within the collapsed Hoberman ring. Second, a simplified strain-energy model is proposed to explain the seemingly bifurcating behavior exhibited while folding, resulting in a folding strategy that ensured the disc shape is achieved.

By deploying the assembly under water and achieving the predicted expansion, I demonstrate that by embedding and distributing the method of deployment within the material itself, I am able to deploy a mechanical system without external actuators, sensors or power supply. As the proposed design is under the highest mechanical stress during the collapse process,

it is guaranteed that during deployment no material failure can occur. The proposed system may serve as a new way to design complex mechanical systems.



## DISCUSSION AND OUTLOOK

---

### 8.1 PRINCIPLE FINDINGS AND CONTRIBUTIONS

Work presented in this thesis designs next generation mechanical systems for shape reconfiguration, deployment and propulsion. Specifically, this work demonstrates the design of mechanical systems that are able to achieve autonomous functional transformation through the underlying materials. By 3D printing these complex systems with the functional materials embedded, their performance becomes tunable and assembly is reduced. In this chapter, the principle findings are summarized, and the contributions from each are put in the context of the above research goal and the hypotheses outlined in Chapter 1.

Two fundamental building blocks used in this work are mechanical instability and the shape memory effect. Chapter 2 and 3 investigate each of these building blocks. In Chapter 2, a bistable mechanism is proposed to enable multi-stable multi-state shape transformation that are load bearing. The proposed mechanism is fabricated using a combination of compliant and stiff materials. Utilizing a compliant material for the joints that undergoes a  $90^\circ$  rotation, the stroke length of the bistable mechanism is greatly increased. The triggering force of the bistable mechanism is tunable by changing the joint stiffness without impacting the stroke length. The mechanical behavior of this bistable mechanism is verified through experimental testing and finite element simulation. It is shown that the behavior of this mechanism is asymmetric, i.e. the two equilibrium states are not equally energetic. The rotational stiffness of the joints is crucial in accurately portraying this asymmetry. The proposed bistable mechanism is placed within a 2 dimensional lattice to enable out-of-plane structural deployment. Accounting for the asymmetric behavior, a kinematic simulation, modified Dynamic Relaxation, is able to accurately predict the deployed shape. This chapter proposes a mechanism that is able to remain stable in two or more configurations with energy only needed during transformation.

In Chapter 3, a 3D printed Shape Memory Polymer (SMP) is characterized for its suitability to power autonomous transformation. A viscoelastic constitutive model this polymer is proposed following a thermomechanical analysis. First the  $T_g$  of a number of digital materials are investigated using DSC. One material with  $T_g$  above room temperature is selected for further characterization. Such a material will remain in its glassy state under room temperature, and provide structural stiffness. Dynamic mechanical analysis is conducted on the material to eventually construct a viscoelastic material model that can be used in a finite element package. Two dimensional auxetic meta-material is created to demonstrate the shape memory cycle. This chapter provides a fundamental understanding of a polymeric smart material in the context of engineering applications.

Using these two fundamental building blocks, functional transformation is demonstrated in both a static and a dynamic mechanical system. In Chapter 4, pairing a SMP strip with a bistable mechanism, I achieve the deployment of structures that are load bearing during deployment and after. The SMP strip is designed to either extend or contract depending on the programming. When exposed to higher temperature, the strip relaxes and triggers the bistable mechanism. While the SMP itself is able to achieve transformation, the bistable mechanism provides two significant advantages, 1) it defines the magnitude of SMP programming, i.e. the extension or the contraction of the SMP is identical to the stroke length of the bistable mechanism, 2) during deployment under an elevated temperature, the bistable mechanism amplifies the load bearing capacity of the SMP. The bistable SMP actuator is similarly installed in a flat lattice to demonstrate structural deployment.

In Chapter 5, a similar bistable SMP pairing is used to achieve autonomous propulsion in a swimming robot. In this case, the SMP acts as a muscle that expands to trigger snap-through bistability. When the bistable mechanism is moved beyond its mid-point (unstable equilibrium), it snaps towards the second stable equilibrium state rapidly. By pre-programming both the SMP muscle and the bistable mechanism, and leveraging the asymmetric behavior of the bistable mechanism, a smaller energy input into the system allows the release of a larger energy output. By connecting the bistable mechanism to a pair of oars, the robot is propelled forward by the momentum generated when the snapping occurs. By connecting multiple pairs of SMP muscle and bistable mechanisms, sequential propulsion is achieved. The positions of the oars and the  $T_g$  of the SMP materials are tuned to change the path (left, straight or right) or directionality (forward or backward) of the propulsion.

The proposed robot demonstrates the use of soft materials to replace and integrate complex mechanical components. In particular, the power supply and the actuator are replaced by the SMP muscle and the bistable mechanism respectively. The control and propulsion behavior is inherently encoded in the materials and the design. For the first time, autonomous locomotion is achieved using soft polymers fabricated entirely with the material jetting process.

Having demonstrated the potential of pairing shape memory polymers and bistable mechanisms, in the two subsequent chapters, different aspects of this technology is explored in the context of real world engineering challenges. Rational design approaches are needed to explore this much expanded design space.

Thus far I have shown the feasibility of fabricating a deployable structure. Chapter 6 proposes a generative algorithm that addresses the design of deployable multi-stable surfaces. In particular, it generates a flat surface that can deploy to multiple target shapes. The algorithm starts by discretizing the target surfaces using quadrilateral mesh elements with the same edge length. For doubly curved shapes, the four internal angles of the mesh elements have defects or excesses, where as for a flat square element, the angles are identically  $1/2\pi$ . Since the internal angles are directly correlated with the curvature, by changing these angles, the flat surface will assume its target shape(s). The angles are changed by changing the length of the diagonal members of each element. To ensure that the shape remains stable after the length change, bistable mechanisms are inserted in each of the diagonal members. The stroke length



of each mechanism is tuned to provide the desired angle change. An example consisting of 24 mesh elements is shown to assume two target shapes. This chapter demonstrates a solution to the inverse problem of designing a flat surface that can deploy to a target shape. Since the envelope dimension of each flat mesh element is identical, tiling them on a flat surface is trivial. Instead, the interior parametric of each mesh element is tuned to the target shape. Such a concept can be extended to the design of periodic meta-material in general where a target functionality is defined.

Chapter 7 shows a concrete example of an autonomously expanding solar panel. As it is prohibitively expensive to bring large structures into space, intricate stowage and deployment strategies involving actuators, power supply and electronics are designed for space bound solar panels. The solar panels themselves are merely passive structural carriers of individual PV cells. With such designs, significant portions of the allotted space is used by components that do not directly contribute to the generation of power. In fact, some actively require power to function. Through the use of a scissor mechanism with shape memory hinges and a “flasher” origami sheet serving as a substrate for PV cells, I demonstrate a self-deploying solar panel that is able to expand to ten times its original area when exposed to heat. In addition to being a credible engineering example of 4D printing, this work illustrates several design principles that are uniquely applicable to multi-material 3D printing of functional materials.

The goal of designing mechanical systems that exhibit autonomous functional transformation through a material-based approach is largely achieved. Through the design of the mechanical systems in this thesis, a number of common notions are challenged and several new design principles emerge. These are centered around using materials to achieve functionality.

- Moving beyond linear elastic materials and mechanics allow for much more interesting and powerful behaviors. In this case, both bistability and viscoelasticity are non-linear phenomena that are exploited. This requires much more sophisticated simulation tools as well as simulation abstraction at different complexities.
- Typically mechanical systems are actuated through a network of motors working in concert with sophisticated control algorithms. In a material-based approach, the “control” is rudimentary and potentially global, e.g. an increase of ambient temperature. Therefore, the sequencing and duration of actuation must be directly encoded into the design and materials.
- Complex mechanical systems typically consist of a network of rigid elements connected using various frictionless, dimensionless joints. In this work, mechanical systems are designed considering the materials as elastic bodies with varying stiffness and multi-physical properties such as the shape memory effect.
- Since many fabricated polymers from a photopolymerization process exhibit the shape memory effect, it is possible and beneficial to distribute the shape changing functionality across the entire design. This improves robustness and scalability of the system.
- Due to the glass transition in the fabricated polymers, one is able to encode multi-functionality within the material, e.g. temperature dependent deformation behavior.



This can be exploited to reduce mass and volume of a mechanical system, e.g. a chassis when heated also serves to deploy the payload, and when subsequently cooled, retains its rigidity.

- To effectively leverage these advances in material understanding, fabrication technologies, structures and design, more capable computational design tools are needed to assist practicing engineers. Software ranging from computer-aided design, numerical simulation, generative design and optimization must be developed to integrate these new advances.

## 8.2 OUTLOOK

There remains much to be done in a number of areas as technologies mature. Here I list several areas that if achieved, will advance the field. These can be categorized as 1) multi-functional smart polymers, 2) multi-scale additive manufacturing, and 3) multi-dimensional bistable mechanisms.

### 8.2.1 *Multi-Functional Smart Polymers*

Most shape changing functional polymers in literature provide either a large force  $F$  but small displacement  $d$  during transformation, or vice versa. For example, a shape memory polymer with  $T_g$  near room temperature is able to undergo a large deformation, but its force of recovery is small compare to a polymer with a higher  $T_g$ . A polymer that has a high specific work capacity ( $W = F \cdot d$ ) remains elusive.

With the existing functional polymers such as swelling hydrogels and shape memory polymers, the transformation is not autonomously reversible, i.e. manual reset is necessary prior to subsequent transformation. By contrast, a two-way shape memory alloy is an established technology that is already seeing industrial use in coronary stents, satellite antenna, as well as other devices. The availability of a polymeric equivalent is still lacking. Thus far, the only 3D printable polymer that demonstrates reversible shape change is a liquid crystal elastomer [6]. However, as its transformation is dictated by the in-plane print nozzle movement, it is impossible to “program” along any vectors with a out-of-plane component.

Surveying existing literature from the chemistry community, a reversible shape memory polymer that does not require an embedded nematic order exists [154, 155]. Such a polymer is reportedly cured with a similar wavelength as some commercial Stereolithography machines, opening up the possibility to fabricate active designs that are much more geometrically complex. With such a material, one is able to design true reversible machines that can react to environmental temperature cycles. Using the swimming robot as an example, with a reversible shape memory polymer muscle that contracts and extends depending on the temperature of the surrounding water, the robot will be able to theoretically achieve one stroke per day over many cycles.

### 8.2.2 Multi-Scale Additive Manufacturing

Hierarchical architecture is frequently exhibited in natural structures, where the smallest feature to the envelope dimension spans more than five-order of magnitudes [156]. Nature achieves this level of precision and detail through the additive process of growth. To create high performance meta-materials that can be as freely utilized as a natural material, fabrication processes must have a precision on a nanometer to micrometer scale, but yet can fabricate geometries that exceeds meters in a realistic time frame.

Different fabrication technologies have been proposed to separately covered parts of the length scale (Fig. 8.1). Recently, using a mix of different technologies, researchers fabricated a metallic lattice that spans seven magnitudes [157]. Part of this work covers the length spectrum between mm to m, whereas other additive manufacturing technologies are designed to construct large scale structures. The same design principles developed in this thesis can be applied to different length scales given an appropriate additive manufacturing process.

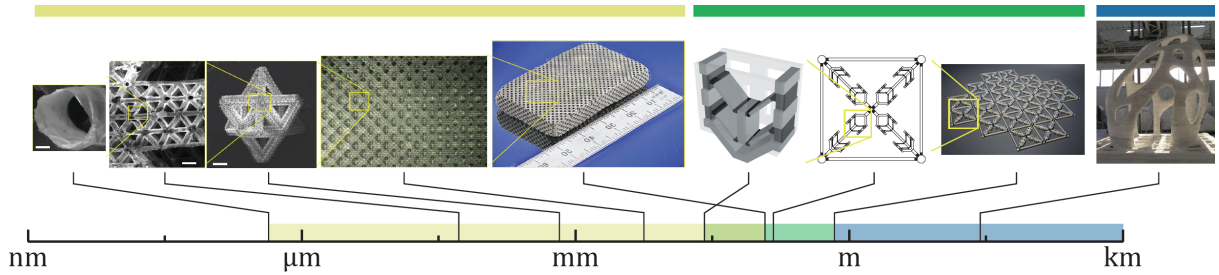


FIGURE 8.1: Additive manufacturing at different length scales. The first project demonstrates the fabrication of hierarchical lattices [157]. The second is from this thesis and uses commercial 3D printers to fabricate mechanical systems at the human scale. The last project demonstrates fabrication for the built environment using a mixture of granular material and binder agents with stiffness similar to that of cement.

### 8.2.3 Multi-Dimensional Bistable Mechanisms

Rigid mechanisms such as the ones proposed in this work consist of one dimensional elements such as beams or trusses. Two dimensional buckling mechanisms have been developed, however, they are fabricated using elastomers.

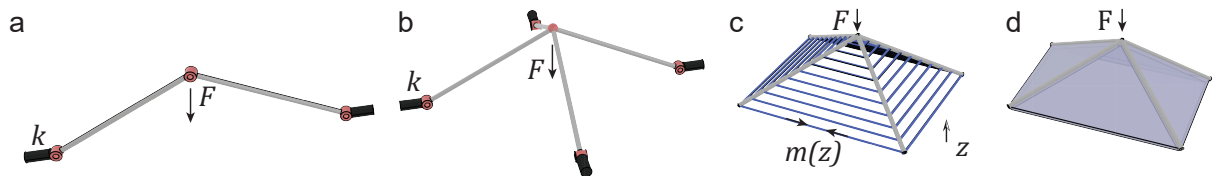


FIGURE 8.2: The evolution of bistable mechanisms from one dimensional trusses to a shallow shell structure.

The evolution from a one dimensional mechanism can be seen in Fig. 8.2. By rotating a truss mechanism by  $90^\circ$  one merely doubles its triggering force  $F$  (Fig. 8.2b). However, if one adds

material to connect these two trusses, the triggering force increases by orders of magnitude (Fig. 8.2c,d). At the same time, this mechanism becomes self-bistable, i.e. bistability does not depend on the stiffness of the supports (springs  $k$ ), but rather the hoop force  $m(z)$ . This type of bistability falls under shell buckling. Due to the hoop force inherent in double curved shells, bistable mechanisms such as the Venus Flytrap is magnitudes more energetic than the beam or truss based mechanisms. The analysis of shells are significantly more involved, and the fabrication is likewise more difficult. Recently [158], exploiting the fused deposition modeling technology, one is able to embed a pre-strain in the filament as it is heated and extruded. By changing the print path of the fabrication process, one is able to active shape change by post-heating of the printed design. This shape potentially exhibits bistability.

### 8.3 CONCLUSION

There has been a flurry of research activities at the intersection between functional materials, non-linear mechanics, computational design and advanced fabrication. This is driven partly in response to the ever more demanding mechanical engineering challenges such as exploration of space, targeted delivery of medicine and treatment, and environmental monitoring. With ever more capable simulation tools and fabrication technologies, engineers are increasingly able to utilize phenomena within materials and mechanics that are previously thought impossible.

This work demonstrates a materials based approach to the design of next generation mechanical systems. By combining mechanical bistability and shape memory polymers, this thesis demonstrates structural transformation by fabricating a flat sheet and enabling its out-of-plane deployment through thermal exposure. By exploiting the momentum generated when the bistable mechanism snaps to its second equilibrium state, autonomous propulsion of a swimming robot is demonstrated. In both cases, both the power necessary to achieve the desired functionality, and timing of these functionalities are entirely encoded within the polymeric materials and the design.

As a next step in tackling complex engineering challenges, these principles are investigated with respect to scalability and applicability. A solution is proposed for the inverse problem of the design of a flat sheet that deploys to assume the given target shapes. The flat sheet is parametrized through the tiling of square unit modules. The internal architecture of each module is defined in relation to the shape of the target surfaces. This generative design method is demonstrated by fabricating one flat structure that can deploy to two different states.

Lastly, I propose a self-deploying solar panel that is only feasible due to a material-based design approach as majority of the structure also serves as the source of actuation. Using a ring of 20 scissor mechanisms with each hinge fabricated using a shape memory polymer, the ring is able to expand radially outward. At the center of the ring, a thin shape memory polymer substrate is used to affix the PV cells. This substrate is folded following an origami pattern. At an elevated temperature, the robust self-deployment is completed in under 40 seconds. When

cooled, both the ring and the substrate serve as rigid structural element supporting the PV cells.

The demonstrated design principles are not limited to particular forms of instability or functional materials. With advances in material science and fabrication technologies, designs following these principles can be made smaller and more efficient. Returning to the potential applications, a meta-material based design with self-deploying mechanisms may apply to the installation of large-scale space structures, a temperature dependent release mechanism may allow for the precise delivery of medicine and multi-functional materials may contribute to environmental monitoring.

In conclusion, the work presents both a new direction in mechanical design and concrete demonstrations of mechanical systems that can achieve autonomous functional transformation through a materials-based approach. As such, it has the potential to inspire a new generation of innovative mechanical systems.



## BIBLIOGRAPHY

---

1. Bhattacharya, K. & James, R. D. The material is the machine. *Science* **307**, 53 (2005).
2. Wehner, M., Truby, R. L., Fitzgerald, D. J., Mosadegh, B., Whitesides, G. M., Lewis, J. A. & Wood, R. J. An integrated design and fabrication strategy for entirely soft, autonomous robots. *Nature* **536**, 451 (2016).
3. Chen, T., Mueller, J. & Shea, K. Integrated Design and Simulation of Tunable, Multi-State Structures Fabricated Monolithically with Multi-Material 3D Printing. *Scientific Reports* **7**, 45671 (2017).
4. Raviv, D., Zhao, W., McKnelly, C., Papadopoulou, A., Kadambi, A., Shi, B., Hirsch, S., Dikovsky, D., Zyracki, M., Olguin, C., Raskar, R. & Tibbits, S. Active printed materials for complex self-evolving deformations. *Scientific Reports* **4**, 7422 (2014).
5. Ge, Q., Qi, H. J. & Dunn, M. L. Active materials by four-dimension printing. *Applied Physics Letters* **103** (2013).
6. Kotikian, A., Truby, R. L., Boley, J. W., White, T. J. & Lewis, J. A. 3D Printing of Liquid Crystal Elastomeric Actuators with Spatially Programed Nematic Order. *Advanced Materials* **1706164**, 1706164 (2018).
7. Zhang, Q., Yan, D., Zhang, K. & Hu, G. Pattern transformation of heat-shrinkable polymer by three-dimensional (3D) printing technique. *Scientific reports* **5**, 8936 (2015).
8. Wang, Q., Jackson, J. A., Ge, Q., Hopkins, J. B., Spadaccini, C. M. & Fang, N. X. Lightweight Mechanical Metamaterials with Tunable Negative Thermal Expansion. *Physical Review Letters* **117**, 1 (2016).
9. Zhang, Q., Zhang, K. & Hu, G. Smart three-dimensional lightweight structure triggered from a thin composite sheet via 3D printing technique. *Scientific Reports* **6**, 1 (2016).
10. Meza, L. R., Zelhofer, A. J., Clarke, N., Mateos, A. J., Kochmann, D. M. & Greer, J. R. Resilient 3D hierarchical architected metamaterials. *Proceedings of the National Academy of Sciences of the United States of America* **112**, 11502 (2015).
11. Gaynor, A., Meisel, N. A., Williams, C. B. & Guest, J. K. Multiple-Material Topology Optimization of Compliant Mechanisms Created Via PolyJet 3D Printing. *Journal of Manufacturing Science and Engineering* **136**, 1 (2014).
12. Tibbits, S., McKnelly, C., Olguin, C., Dikovsky, D. & Hirsch, S. *4D Printing and Universal Transformation in Acadia 2014* (2014), 539.
13. Mao, Y., Yu, K., Isakov, M. S., Wu, J., Dunn, M. L. & Qi, H. J. Sequential Self-Folding Structures by 3D Printed Digital Shape Memory Polymers. *Scientific Reports* **5**, 13616 (2015).

14. Overvelde, J. T. B., Kloek, T., D'haen, J. J. A. & Bertoldi, K. Amplifying the response of soft actuators by harnessing snap-through instabilities. *Proceedings of the National Academy of Sciences of the United States of America* **112**, 10863 (2015).
15. Raney, J. R., Nadkarni, N., Daraio, C., Kochmann, D. M., Lewis, J. A. & Bertoldi, K. Stable propagation of mechanical signals in soft media using stored elastic energy. *Proceedings of the National Academy of Sciences* **113**, 9722 (2016).
16. Nadkarni, N., Arrieta, A. F., Chong, C., Kochmann, D. M. & Daraio, C. Unidirectional Transition Waves in Bistable Lattices. *Physical Review Letters* **116**, 1 (2016).
17. Shan, S., Kang, S. H., Raney, J. R., Wang, P., Fang, L., Candido, F., Lewis, J. A. & Bertoldi, K. Multistable Architected Materials for Trapping Elastic Strain Energy. *Advanced Materials* **27**, 4296 (2015).
18. Bertoldi, K., Reis, P. M., Willshaw, S. & Mullin, T. Negative poisson's ratio behavior induced by an elastic instability. *Advanced Materials* **22**, 361 (2010).
19. Shim, J., Perdigou, C., Chen, E. R., Bertoldi, K. & Reis, P. M. Buckling-induced encapsulation of structured elastic shells under pressure. *Proceedings of the National Academy of Sciences* **109**, 5978 (2012).
20. Henke, E.-F. M., Schlatter, S. & Anderson, I. A. A Soft Electronics-Free robot. *Science* **100** (2012).
21. Shepherd, R. F., Ilievski, F., Choi, W., Morin, S. a., Stokes, A. A., Mazzeo, A. D., Chen, X., Wang, M. & Whitesides, G. M. Multigait soft robot. *Proceedings of the National Academy of Sciences* **108**, 20400 (2011).
22. Miyashita, S., Guitron, S., Ludersdorfer, M., Sung, C. R. & Rus, D. An untethered miniature origami robot that self-folds, walks, swims, and degrades. *2015 IEEE International Conference on Robotics and Automation (ICRA)*, 1490 (2015).
23. Klein, Y., Efrati, E. & Sharon, E. Shaping of Elastic Sheets by Prescription of Non-Euclidean Metrics. *Science* **315**, 1116 (2007).
24. Maute, K., Tkachuk, A., Wu, J., Qi, H. J., Ding, Z. & Dunn, M. L. Level Set Topology Optimization of Printed Active Composites. *Journal of Mechanical Design* **137**, 111402 (2015).
25. Pikul, A. J. H., Li, S., Bai, H., Hanlon, R. T., Cohen, I. & Shepherd, R. F. Stretchable surfaces with programmable 3-D texture morphing for synthetic camouflaging skins. *Science*, 1 (2017).
26. Celli, P., McMahan, C., Ramirez, B., Bauhofer, A., Naify, C., Hofmann, D., Audoly, B. & Daraio, C. Shape-morphing architected sheets with non-periodic cut patterns. *arXiv* (2018).
27. Wingert, A., Lichter, M., Dubowsky, S. & Hafez, M. Hyper-redundant robot manipulators actuated by optimized binary-dielectric polymers. *Proceedings of SPIE* **4695**, 415 (2002).



28. Schioler, T. & Pellegrino, S. Space Frames with Multiple Stable Configurations. *AIAA Journal* **45**, 1740 (2007).
29. Restrepo, D., Mankame, N. D. & Zavattieri, P. D. Phase transforming cellular materials. *Extreme Mechanics Letters* **4**, 52 (2015).
30. Hu, N. & Burgueño, R. Buckling-induced smart applications: recent advances and trends. *Smart Materials and Structures* **24**, 063001 (2015).
31. Leelavanichkul, S., Cherkaev, A., Adams, D. O. & Solzbacher, F. Energy Absorption of a Helicoidal Bistable Structure. *Journal of Mechanics of Materials and Structures* **5**, 305 (2010).
32. Zhang, Z., Chen, D., Wu, H., Bao, Y. & Chai, G. Non-contact magnetic driving bioinspired Venus flytrap robot based on bistable anti-symmetric CFRP structure. *Composite Structures* **135**, 17 (2016).
33. Han, J. S., Mueller, C., Wallrabe, U. & Korvink, J. G. Design, Simulation, and Fabrication of a Quadstable Monolithic Mechanism With X- and Y-Directional Bistable Curved Beams. *Journal of Mechanical Design* **129**, 1198 (2007).
34. Oh, Y. S. & Kota, S. Synthesis of multistable equilibrium compliant mechanisms using combinations of bistable mechanisms. *Journal of Mechanical Design* **131**, 021002 (2009).
35. Choi, J., Kwon, O.-C., Jo, W., Lee, H. J. & Moon, M.-W. 4D Printing Technology: A Review. *3D Printing and Additive Manufacturing* **2**, 159 (2015).
36. Von Mises, R. Über die Stabilitätsprobleme der Elastizitätstheorie. *Zeitschrift für angewandte Mathematik und Mechanik* **3**, 406 (1923).
37. Stankovic, T., Mueller, J., Egan, P. & Shea, K. A Generalized Optimality Criteria Method for Optimization of Additively Manufactured Multimaterial Lattice Structures. *Journal of Mechanical Design* **137**, 111405 (2015).
38. Mueller, J., Shea, K. & Daraio, C. Mechanical properties of parts fabricated with inkjet 3D printing through efficient experimental design. *Materials & Design* **86**, 902 (2015).
39. Howell, L. L., Rao, S. S. & Midha, A. Reliability-Based Optimal Design of a Bistable Compliant Mechanism. *Journal of Mechanical Design* **116**, 1115 (1994).
40. Perelmuter, A. V. & Slivker, V. I. *Handbook of Mechanical Stability in Engineering* 1st, 357 (World Scientific Publishing Co. Pte. Ltd., Singapore, 2013).
41. Murray, G. J. & Gandhi, F. S. *The Use of Damping to Mitigate Violent Snap-Through of Bistable Systems in Proceedings of the ASME 2011 Conference on Smart Materials, Adaptive Structures and Intelligent Systems* (2011), 1.
42. Chen, G., Gou, Y. & Yang, L. *Research on Multistable Compliant Mechanisms: The State of the Art in Proceedings of the 9th International Conference on Frontiers of Design and Manufacturing* (2010), 1.
43. Cherry, B. B., Howell, L. L. & Jensen, B. D. Evaluating three-dimensional effects on the behavior of compliant bistable micromechanisms. *Journal of Micromechanics and Micro-engineering* **18**, 095001 (2008).

44. Barbarino, S., Gandhi, F. S. & Visdeloup, R. A Bi-Stable Von-Mises Truss for Morphing Applications Actuated Using Shape Memory Alloys. *Proceedings of the ASME 2013 Conference on Smart Materials, Adaptive Structures and Intelligent Systems* **1**, V001T01A004 (2013).
45. Haghpanah, B., Salari-sharif, L., Pourrajab, P., Hopkins, J. & Valdevit, L. Multistable Shape-Reconfigurable Architected Materials. *Advanced Materials* **28**, 7915 (2016).
46. Gerson, Y., Krylov, S., Ilic, B. & Schreiber, D. Large displacement low voltage multi-stable micro actuator. *2008 IEEE 21st International Conference on Micro Electro Mechanical Systems*, 463 (2008).
47. Chen, T. & Shea, K. *Design and Fabrication of Hierarchical Multi-Stable Structures through Multi-Material Additive Manufacturing in Proceedings of the ASME 2016 International Design Engineering Technical Conferences & Computers and Information in Engineering Conference* (Charlotte, NC, 2016), V02AT03A032.
48. Adriaenssens, S., Barnes, M., Harris, R. & Williams, C. in *Shell Structures for Architecture: Form Finding and Optimization* (eds Adriaenssens, S., Block, P., Veenendaal, D. & Williams, C.) 1st, 89 (Routledge, Abingdon, Oxon, 2014).
49. Zhang, J. Y. & Ohsaki, M. Adaptive force density method for form-finding problem of tensegrity structures. *International Journal of Solids and Structures* **43**, 5658 (2006).
50. Schek, H. J. The force density method for form finding and computation of general networks. *Computer Methods in Applied Mechanics and Engineering* **3**, 115 (1974).
51. Noemi, F. & Ibrahimbegovic, A. Overview of Highly Flexible, Deployable Lattice Structures Used in Architecture and Civil Engineering Undergoing Large Displacements. *YBL Journal of Built Environment* **1**, 85 (2013).
52. Tibbits, S. 4D Printing: Multi-Material Shape Change. *Architectural Design* **84**, 116 (2014).
53. Ge, Q., Luo, X., Rodriguez, E. D., Zhang, X., Mather, P. T., Dunn, M. L. & Qi, H. J. Thermomechanical behavior of shape memory elastomeric composites. *Journal of the Mechanics and Physics of Solids* **60**, 67 (2012).
54. Liu, Y., Du, H., Liu, L. & Leng, J. Shape memory polymers and their composites in aerospace applications: A review. *Smart Materials and Structures* **23** (2014).
55. Álvarez Elipe, J. C. & Díaz Lantada, A. Comparative study of auxetic geometries by means of computer-aided design and engineering. *Smart Materials and Structures* **21** (2012).
56. Wu, J., Yuan, C., Ding, Z., Isakov, M., Mao, Y., Wang, T., Dunn, M. L. & Qi, H. J. Multi-shape active composites by 3D printing of digital shape memory polymers. *Scientific Reports* **6**, 1 (2016).
57. Ge, Q., Sakhaei, A. H., Lee, H., Dunn, C. K., Fang, N. X. & Dunn, M. L. Multimaterial 4D Printing with Tailorable Shape Memory Polymers. *Scientific Reports* **6**, 31110 (2016).

58. Mao, Y., Ding, Z., Yuan, C., Ai, S., Isakov, M. S., Wu, J., Wang, T., Dunn, M. L. & Qi, H. J. 3D Printed Reversible Shape Changing Components with Stimuli Responsive Materials. *Scientific reports* **6**, 24761 (2016).
59. Sydney Gladman, A., Matsumoto, E. A., Nuzzo, R. G., Mahadevan, L. & Lewis, J. A. Biomimetic 4D printing. *Nature materials* **15**, 413 (2016).
60. Zhao, Q., Qi, H. J. & Xie, T. Recent progress in shape memory polymer: New behavior, enabling materials, and mechanistic understanding. *Progress in Polymer Science* **49-50**, 79 (2014).
61. Rossiter, J., Takashima, K., Scarpa, F., Walters, P. & Mukai, T. Shape memory polymer hexachiral auxetic structures with tunable stiffness. *Smart Materials and Structures* **23** (2014).
62. Ferry, J. D. *Viscoelastic Properties of Polymers* 3rd, 1 (John Wiley & Sons, Inc., Toronto, 1980).
63. Schwarzl, F. R. Numerical calculation of stress relaxation modulus from dynamic data for linear viscoelastic materials. *Rheologica Acta* **14**, 581 (1975).
64. Bodaghi, M., Damanpack, A. R. & Liao, W. H. Self-expanding/shrinking structures by 4D printing. *Smart Materials and Structures* **25**, 105034 (2016).
65. Lantada, A. D. *Handbook of active materials for medical devices : advances and applications* (Pan Stanford Publishing, Singapore, 2012).
66. Lan, X., Liu, Y., Lv, H., Wang, X., Leng, J. & Du, S. Fiber reinforced shape-memory polymer composite and its application in a deployable hinge. *Smart Materials and Structures* **18**, 024002 (2009).
67. Leong, T. G., Randall, C. L., Benson, B. R., Bassik, N., Stern, G. M. & Gracias, D. H. Tetherless thermobiochemically actuated microgrippers. *Proceedings of the National Academy of Sciences of the United States of America* **106**, 703 (2009).
68. Guo, X., Li, H., Ahn, B. Y., Duoss, E. B., Hsia, K. J., Lewis, J. A. & Nuzzo, R. G. Two- and three-dimensional folding of thin film single-crystalline silicon for photovoltaic power applications. *Proceedings of the National Academy of Sciences of the United States of America* **106**, 20149 (2009).
69. Wang, Q., Gossweiler, G. R., Craig, S. L. & Zhao, X. Cephalopod-inspired design of electro-mechano-chemically responsive elastomers for on-demand fluorescent patterning. *Nature communications* **5**, 4899 (2014).
70. Ryu, J., D'Amato, M., Cui, X., Long, K. N., Qi, H. J. & Dunn, M. L. Photo-origami-Bending and folding polymers with light. *Applied Physics Letters* **100** (2012).
71. Maccurdy, R., Katzschmann, R., Kim, Y. & Rus, D. Printable hydraulics: A method for fabricating robots by 3D co-printing solids and liquids. *Proceedings - IEEE International Conference on Robotics and Automation* **2016-June**, 3878 (2016).
72. Song, Y. S. & Sitti, M. Surface-tension-driven biologically inspired water strider robots: Theory and experiments. *IEEE Transactions on Robotics* **23**, 578 (2007).

73. Zolesi, V., Ganga, P., Scolamiero, L., Micheletti, A., Podio-Guidugli, P., Tibert, G., Donati, A. & Ghiozzi, M. On an innovative deployment concept for large space structures. *42nd International Conference on Environmental Systems*, 1 (2012).
74. Gärdback, M., Tibert, G. & Izzo, D. Design considerations and deployment simulations of spinning space webs. *48th AIAA/ASME/ASCE/AHS/ASC Structures, Structural Dynamics, and Materials Conference* 2, 1503 (2007).
75. Mitsugi, J. I. N., Ando, K., Senbokuya, Y. & Meguro, A. Deployment Analysis of Large Space Antenna Using Flexible Multibody Dynamics Simulation. *Acta Astronautica* 47, 19 (2000).
76. Miura, K. Method of packaging and deployment of large membranes in space. *The Institute of Space and Astronautical Science report* 618, 1 (1985).
77. Liu, K., Wu, J., Paulino, G. H. & Qi, H. J. Programmable Deployment of Tensegrity Structures by Stimulus-Responsive Polymers. *Scientific Reports* 7, 3511 (2017).
78. Clem, A., Smith, S. & Main, J. A pressurized deployment model for inflatable space structures. *41st Structures, Structural Dynamics, and Materials Conference and Exhibit* (2000).
79. Edwards, B. C. Design and deployment of a space elevator. *Acta Astronautica* 47, 735 (2000).
80. Ding, Z., Yuan, C., Peng, X., Wang, T., Qi, H. J. & Dunn, M. L. Direct 4D printing via active composite materials. *Science Advances* 3, e1602890 (2017).
81. Strauss, S., Krog, R. L. & Feiveson, A. H. Extravehicular mobility unit training and astronaut injuries. *Aviation Space and Environmental Medicine* 76, 469 (2005).
82. Wagner, M., Chen, T. & Shea, K. Large Shape Transforming 4D Auxetic Structures. *3D Printing and Additive Manufacturing* 4, 133 (2017).
83. Bazant, Z. P. & Cedolin, L. *Stability of Structures* 1st (ed Wei, T. K.) 1 (World Scientific Publishing Co. Pte. Ltd., Singapore, 2010).
84. Brinkmeyer, A., Pellegrino, S. & Weaver, P. M. Effects of Long-Term Stowage on the Deployment of Bistable Tape Springs. *Journal of Applied Mechanics* 83, 011008 (2015).
85. Ge, Q., Dunn, C. K., Qi, H. J. & Dunn, M. L. Active origami by 4D printing. *Smart Materials and Structures* 23, 1 (2014).
86. Kim, S., Laschi, C. & Trimmer, B. Soft robotics: A bioinspired evolution in robotics. *Trends in Biotechnology* 31, 287 (2013).
87. Rus, D. & Tolley, M. T. Design, fabrication and control of soft robots. *Nature* 521, 467 (2015).
88. Wang, L. & Iida, F. Deformation in Soft-Matter Robotics: A Categorization and Quantitative Characterization. *IEEE Robotics and Automation Magazine* 22, 125 (2015).
89. Mazzolai, B. & Mattoli, V. Robotics: Generation soft. *Nature* 536, 400 (2016).
90. McEvoy, M. A. & Correll, N. Materials that couple sensing, actuation, computation, and communication. *Science* 347, 1261689 (2015).

91. Goldstein, S. C., Campbell, J. D. & Mowry, T. C. Invisible computing: Programmable matter. *Computer* **38**, 99 (2005).
92. Bilal, O. R., Hoehr, A. & Daraio, C. Programmable phononic metamaterial plates. *Advanced Materials* (2017).
93. Zheludev, N. I. & Kivshar, Y. S. From metamaterials to metadevices. *Nature Materials* **11**, 917 (2012).
94. Reis, P. M., Jaeger, H. M. & van Hecke, M. Designer Matter: A perspective. *Extreme Mechanics Letters* **5**, 25 (2015).
95. Fernandes, P. G., Brierley, A. S., Simmonds, E. J., Millard, N. W., McPhail, S. D., Armstrong, F., Stevenson, P. & Squires, M. Fish do not avoid survey vessels. *Nature* **404**, 35 (2000).
96. Jaffe, J. S., Franks, P. J. S., Roberts, P. L. D., Mirza, D., Schurgers, C., Kastner, R. & Boch, A. A swarm of autonomous miniature underwater robot drifters for exploring submesoscale ocean dynamics. *Nature Communications* **14**189, 1 (2017).
97. Onal, C. D. & Rus, D. Autonomous undulatory serpentine locomotion utilizing body dynamics of a fluidic soft robot. *Bioinspiration & biomimetics* **8**, 026003 (2013).
98. Godaba, H., Li, J., Wang, Y. & Zhu, J. A Soft Jellyfish Robot Driven by a Dielectric Elastomer Actuator. *IEEE Robotics and Automation Letters* **1**, 624 (2016).
99. Song, C.-W., Lee, D.-J. & Lee, S.-Y. Bioinspired Segment Robot with Earthworm-like Plane Locomotion. *Journal of Bionic Engineering* **13**, 292 (2016).
100. Tottori, S., Zhang, L., Qiu, F., Krawczyk, K. K., Franco-Obregón, A. & Nelson, B. J. Magnetic helical micromachines: Fabrication, controlled swimming, and cargo transport. *Advanced Materials* **24**, 811 (2012).
101. Marchese, A. D., Onal, C. D. & Rus, D. Autonomous Soft Robotic Fish Capable of Escape Maneuvers Using Fluidic Elastomer Actuators. *Soft Robotics* **1**, 75 (2014).
102. Skotheim, J. M. & Mahadevan, L. Physical Limits and Design Principles for Plant and Fungal Movements. *Science* **308**, 1308 (2005).
103. Patek, S. N., Korff, W. L. & Caldwell, R. L. Biomechanics: Deadly strike mechanism of a mantis shrimp. *Nature* **428**, 819 (2004).
104. Bilal, O. R., Foehr, A. & Daraio, C. Bistable metamaterial for switching and cascading elastic vibrations. *Proceedings of the National Academy of Sciences* **114**, 4603 (2017).
105. Chen, T. & Shea, K. An Autonomous Programmable Actuator and Shape Reconfigurable Structures using Bistability and Shape Memory Polymers. *3D Printing and Additive Manufacturing* **5**, 91 (2018).
106. Song, S.-H., Kim, M.-S., Rodrigue, H., Lee, J.-Y., Shim, J.-E., Kim, M.-C., Chu, W.-S. & Ahn, S.-H. Turtle mimetic soft robot with two swimming gaits. *Bioinspiration & Biomimetics* **11**, 036010 (2016).
107. Dreyfus, R., Baudry, J., Roper, M. L., Fermigier, M., Stone, H. a. & Bibette, J. Microscopic artificial swimmers. *Nature* **437**, 862 (2005).

108. Behl, M., Kratz, K., Zotzmann, J., Nöchel, U. & Lendlein, A. Reversible bidirectional shape-memory polymers. *Advanced Materials* **25**, 4466 (2013).
109. Palagi, S., Mark, A. G., Reigh, S. Y., Melde, K., Qiu, T., Zeng, H., Parmeggiani, C., Martella, D., Sanchez-Castillo, A., Kapernaum, N., Giesselmann, F., Wiersma, D. S., Lauga, E. & Fischer, P. Structured light enables biomimetic swimming and versatile locomotion of photoresponsive soft microrobots. *Nature Materials* **15**, 1 (2016).
110. Lang, R. J. A computational algorithm for origami design. *Proceedings of the twelfth annual symposium on Computational geometry - SCG '96*, 98 (1996).
111. Tachi, T. 3D origami design based on tucking molecule. *Origami* **4**, 259 (2009).
112. Castle, T., Cho, Y., Gong, X., Jung, E., Sussman, D. M., Yang, S. & Kamien, R. D. Making the cut: Lattice kirigami rules. *Physical Review Letters* **113**, 2 (2014).
113. Sussman, D. M., Cho, Y., Castle, T., Gong, X., Jung, E., Yang, S. & Kamien, R. D. Algorithmic Lattice Kirigami: A Route to Pluripotent Materials. *Proceedings of the National Academy of Sciences* **112**, 7449 (2015).
114. Aharoni, H., Sharon, E. & Kupferman, R. Geometry of thin nematic elastomer sheets. *Physical Review Letters* **113**, 1 (2014).
115. Garg, A., Sageman-Furnas, A. O., Deng, B., Yue, Y., Grinspun, E., Pauly, M. & Wardetzky, M. *Wire Mesh Design in ACM Transactions on Graphics (Proceedings of Siggraph)* (2014), 24.
116. Konakovic, M., Crane, K., Deng, B., Bouaziz, S., Piker, D. & Pauly, M. Beyond Developable: Computational Design and Fabrication with Auxetic Materials. *ACM Transactions on Graphics* **35**, 1 (2016).
117. Konakovic, M., Panetta, J., Crane, K. & Pauly, M. Rapid Deployment of Curved Surfaces via Programmable Auxetics. *ACM Transactions on Graphics* **0**, 1 (2018).
118. Hazzidakis, J. N. Ueber einige Eigenschaften der Flächen mit constantem Krümmungsmaass. *Journal für die reine und angewandte Mathematik* (1880).
119. Popov, E. V. Geometric Approach to Chebyshev Net Generation Along an Arbitrary Surface Represented by NURBS. *Graphicon* (2002).
120. McSpadden, J. O. & Mankins, J. C. Space solar power programs and microwave wireless power transmission technology. *IEEE Microwave Magazine* **3**, 46 (2002).
121. McGuire, T., Hirsch, M., Parsons, M., Leake, S. & Straub, J. A CubeSat deployable solar panel system, 98650C (2016).
122. Sigel, D. A., Trease, B. P., Thomson, M. W., Webb, D. R., Willis, P. & Lisman, P. D. *Application of Origami in Starshade Spacecraft Blanket Design in Proceedings of the ASME 2014 International Design Engineering Technical Conferences & Computers and Information in Engineering Conference (IDETC/CIE 2014)* (Buffalo, New York, 2014), DETC2014.
123. Zhang, Y., Yang, D. & Li, S. An integrated control and structural design approach for mesh reflector deployable space antennas. *Mechatronics* **35**, 71 (2014).

124. Mori, O., Sawada, H., Funase, R., Morimoto, M., Endo, T., Yamamoto, T., Tsuda, Y., Kawakatsu, Y., Kawaguchi, J., Miyazaki, Y. & Shirasawa, Y. First Solar Power Sail Demonstration by IKAROS. *Transactions of the Japan Society for Aeronautical and Space Sciences, Aerospace Technology Japan* **8**, To\_4\_25 (2010).
125. Schenk, M., Kerr, S. G., Smyth, a. M. & Guest, S. D. Inflatable Cylinders for Deployable Space Structures. *Proceedings of the First Conference Transformables*, 1 (2013).
126. Block, J., Straubel, M. & Wiedemann, M. Ultralight deployable booms for solar sails and other large gossamer structures in space. *Acta Astronautica* **68**, 984 (2011).
127. Yang, G.-Z., Fischer, P. & Nelson, B. J. New materials for next-generation robots. *Science Robotics* **2**, eaap9294 (2017).
128. Hawkes, E., An, B., Benbernou, N. M., Tanaka, H., Kim, S., Demaine, E. D., Rus, D. & Wood, R. J. Programmable matter by folding. *Proceedings of the National Academy of Sciences* **107**, 12441 (2010).
129. White, T. J. & Broer, D. J. Programmable and adaptive mechanics with liquid crystal polymer networks and elastomers. *Nature Materials* **14**, 1087 (2015).
130. Bauhofer, A. A., Krödel, S., Rys, J., Bilal, O. R., Constantinescu, A. & Daraio, C. Harnessing Photochemical Shrinkage in Direct Laser Writing for Shape Morphing of Polymer Sheets. *Advanced Materials* **1703024**, 1703024 (2017).
131. Chen, Y., Li, T., Scarpa, F. & Wang, L. Lattice Metamaterials with Mechanically Tunable Poisson's Ratio for Vibration Control. *Physical Review Applied* **7**, 1 (2017).
132. Valentine, A. D., Busbee, T. A., Boley, J. W., Raney, J. R., Chortos, A., Kotikian, A., Berri-gan, J. D., Durstock, M. F. & Lewis, J. A. Hybrid 3D Printing of Soft Electronics. *Advanced Materials* **1703817**, 1 (2017).
133. Lind, J. U., Busbee, T. A., Valentine, A. D., Pasqualini, F. S., Yuan, H., Yadid, M., Park, S.-J., Kotikian, A., Nesmith, A. P., Campbell, P. H., Vlassak, J. J., Lewis, J. A. & Parker, K. K. Instrumented cardiac microphysiological devices via multimaterial three-dimensional printing. *Nature Materials* **16**, 303 (2016).
134. Chen, T., Bilal, O. R., Shea, K. & Daraio, C. Harnessing Bistability for Directional Propul-sion of Untethered, Soft Robots. *Proceedings of the National Academy of Sciences of the United States of America* **115**, 5698 (2018).
135. Truby, R. L. & Lewis, J. A. Printing soft matter in three dimensions. *Nature* **540**, 371 (2016).
136. Hoberman, C. *Reversibly Expandable Doubly-Curved Truss Structure* 1990.
137. Larson, C. L. *Scissor-Lift Mechanism* 1966.
138. You, Z. & Pellegrino, S. Foldable bar structures. *International Journal of Solids and Struc-tures* **34**, 1825 (1997).
139. Patel, J. & Ananthasuresh, G. K. A kinematic theory for radially foldable planar linkages. *International Journal of Solids and Structures* **44**, 6279 (2007).



140. Wei, Z. Y., Guo, Z. V., Dudte, L., Liang, H. Y. & Mahadevan, L. Geometric mechanics of periodic pleated origami. *Physical Review Letters* **110**, 1 (2013).
141. Yasuda, H. & Yang, J. Reentrant origami-based metamaterials with negative Poisson's ratio and bistability. *Physical Review Letters* **114**, 1 (2015).
142. Tachi, T. Simulation of Rigid Origami. *Origami 4 Fourth International Meeting of Origami Science Mathematics and Education*, 175 (2009).
143. Hoberman, C. *Folding Covering Panels for Expanding Structures* 2004.
144. Babaei, S., Overvelde, J. T. B., Chen, E. R., Tournat, V. & Bertoldi, K. Reconfigurable origami-inspired acoustic waveguides. *Science Advances* **2**, e1601019 (2016).
145. Overvelde, J. T. B., Weaver, J. C., Hoberman, C. & Bertoldi, K. Rational design of reconfigurable prismatic architected materials. *Nature* **541**, 347 (2017).
146. Boatti, E., Vasios, N. & Bertoldi, K. Origami Metamaterials for Tunable Thermal Expansion. *Advanced Materials* **29** (2017).
147. Shafer, J. *Origami to Astonish and Amuse* 1st, 1 (St. Martin's Griffin, 2001).
148. Czanderna, A. & Pern, F. Encapsulation of PV modules using ethylene vinyl acetate copolymer as a pottant : A critical review. *Solar Energy Materials and Solar Cells* **43**, 101 (1996).
149. Flex Solar Cells. *PowerFilm Wireless Electronics Series SP3-12* tech. rep. (), 1.
150. Zirbel, S. A., Lang, R. J., Thomson, M. W., Sigel, D. A., Walkemeyer, P. E., Trease, B. P., Magleby, S. P. & Howell, L. L. Accommodating Thickness in Origami-Based Deployable Arrays. *Journal of Mechanical Design* **135**, 111005 (2013).
151. Bertoldi, K., Vitelli, V., Christensen, J. & van Hecke, M. Flexible mechanical metamaterials. *Nature Reviews Materials* **2**, 17066 (2017).
152. Lanford, W. E. *Folding Apparatus* 1961.
153. Schenk, M. & Guest, S. D. Origami folding: A structural engineering approach. *Origami 5 Fifth International Meeting of Origami Science Mathematics and Education*, 1 (2011).
154. Li, Q., Zhou, J., Vatankehah-Varnoosfaderani, M., Nykypanchuk, D., Gang, O. & Sheiko, S. S. Advancing Reversible Shape Memory by Tuning the Polymer Network Architecture. *Macromolecules* **49**, 1383 (2016).
155. Wang, K., Jia, Y. G. & Zhu, X. X. Two-Way Reversible Shape Memory Polymers Made of Cross-Linked Cocrystallizable Random Copolymers with Tunable Actuation Temperatures. *Macromolecules* **50**, 8570 (2017).
156. Lakes, R. Materials with structure hierarchy. *Nature* **361**, 511 (1993).
157. Zheng, X., Smith, W., Jackson, J., Moran, B., Cui, H., Chen, D., Ye, J., Fang, N., Rodriguez, N., Weisgraber, T. & Spadaccini, C. M. Multiscale metallic metamaterials. *Nature Materials* **15**, 1100 (2016).
158. Van Manen, T., Janbaz, S. & Zadpoor, A. A. Programming 2D/3D shape-shifting with hobbyist 3D printers. *Mater. Horiz.* **4**, 1064 (2017).

## CURRICULUM VITAE

---

### PERSONAL DATA

Name	Tian (Tim) Chen
Date of Birth	December 31, 1987
Place of Birth	Shanghai, China
Citizen of	Canada

### EDUCATION

<b>Doctor of Science</b> , Mechanical Engineering ETH Zurich, Switzerland Advisor: Prof. Kristina Shea	Dec. 2018
<b>Master of Science</b> , Civil Engineering, <i>Cum Laude</i> Delft University of Technology, the Netherlands	June 2014
<b>Bachelor of Applied Science</b> , Engineering Science University of Toronto, Ontario, Canada	June 2010

### PROFESSIONAL EXPERIENCE

<b>Postdoctoral Researcher</b> Flexible Structures Laboratory & Computer Graphics and Geometry Laboratory, EPFL, Switzerland Advisor: Prof. Pedro Reis & Prof. Mark Pauly	Jan. 2019
<b>Doctoral Researcher</b> Engineering Design and Computing Laboratory, ETH Zurich, Switzerland Advisor: Prof. Kristina Shea	Sept. 2014 - Dec. 2018
<b>Visiting Researcher</b> Daraio Research Group, California Institute of Technology, USA Advisor: Prof. Chiara Daraio	June - Sept., 2017
<b>Structural Engineer</b> Arup, Amsterdam, the Netherlands	June 2013 - June 2014

## TEACHING

Engineering Design Optimization, D-MAVT, ETH Zurich	2015 - 2018
CAD and Technical Drawing, D-MAVT, ETH Zurich	2014 - 2016

## SUPERVISION

### Master Theses

- Koh, M., (2018), "Designing Activated Buckling Structures Using FDM 3D Printing"
- Du Pasquier, C., (2017), "Modular Pneumatic Toolkit: an Application of 4D-Printing"
- Wagner, M., (2016), "3D Printed Active Structures Using Shape Memory Polymers"
- Liu, J., (2016), "Mechanical Properties of Multi-Material Structures"
- Zimmermann, L., (2015), "Generative Design with Shape Grammar & Simulation"

### Semester Projects and Bachelor Theses

- Volk, C., (2018), "Magnetically Controlled Reversible Appendage".
- Ulrich, L., (2018), "Effect of Poisson's Ratio on Energy trapping Meta-material".
- Fritzsche, D., (2017), "Studying the Activation and Instability of FDM Sheets".
- Gustaf, W., (2017), "Biomimetic Buckling Mechanisms".
- Freitag, J., (2017), "3D Printing Resin with Reversible Shape Memory Effect".
- Sesseg, J., (2017), "Light-activated Synthetic Resin Using Azobenzene".
- Felber, R., (2017), "Design of 4D light Activated Joints".
- Koh, M., (2016), "Design and Analysis of 3D Printed Bistable Structures".

## SELECTED DISTINCTIONS AND AWARDS

**Global Young Scientists Summit** Recipient of nomination and attendee, 2019  
National Research Foundation, Prime Minister's Office, Singapore.

**Swiss National Science Foundation** Recipient of the Early Postdoc.Mobility fellowship, 2018  
Daraio Research Group, "Exploring Mechanical Instability for Assistive Exoskeletal Devices".

**International Design Engineering Technical Conferences**, Best Paper Nominee, 2015  
"Studying the Impact of Incorporating an Additive Manufacturing Based Design Exercise in a Large, First Year Technical Drawing and CAD Course".

## DESIGN PROJECTS

- |   |      |
|---|------|
| <b>On AG</b> Design and fabrication of 3D printed weaved fabric for athletic shoes. | 2018 |
| <b>World Economic Forum</b> A 3D printed brain used for Augmented Reality.          | 2017 |



## PUBLICATIONS

---

### Articles in peer-reviewed journals:

1. Chen, T. & Shea, K. Algorithmic Generation of Multi-Stable Surfaces. *In submission* (2019).
2. Chen, T., Bilal, O. R., Lang, R. J., Daraio, C. & Shea, K. Autonomous Deployment of a Solar Panel Using an Elastic Origami and Distributed Shape Memory Polymer Actuators. *In submission* (2019).
3. Chen, T., Bilal, O. R., Shea, K. & Daraio, C. Harnessing Bistability for Directional Propulsion of Untethered, Soft Robots. *Proceedings of the National Academy of Sciences of the United States of America* **115**, 5698 (2018).
4. Chen, T. & Shea, K. An Autonomous Programmable Actuator and Shape Reconfigurable Structures using Bistability and Shape Memory Polymers. *3D Printing and Additive Manufacturing* **5**, 91 (2018).
5. Chen, T., Mueller, J. & Shea, K. Integrated Design and Simulation of Tunable, Multi-State Structures Fabricated Monolithically with Multi-Material 3D Printing. *Scientific Reports* **7**, 45671 (2017).
6. Du Pasquier, C., Chen, T., Tibbits, S. & Shea, K. Design and Computational Modeling of a 3D Printed Pneumatic Toolkit for Soft Robotics. *In submission*.
7. Koh, M., Chen, T., Tibbits, S. & Shea, K. Shape Reconfiguring Bistable Surfaces Using Heat Activated Fibers. *In submission*.
8. Schwarz, J., Chen, T., Stankovic, T. & Shea, K. Efficient Size and Shape Optimization of Truss Structures Subject to Stress and Local Buckling Constraints using Sequential Linear Programming. *Structural and Multidisciplinary Optimization* **58**, 171 (2018).
9. Zimmermann, L., Chen, T. & Shea, K. A 3D, Performance-Driven Generative Design Framework: Automating the Link from a 3D Spatial Grammar Interpreter to Structural Finite Element Analysis and Stochastic Optimization. *Artificial Intelligence for Engineering Design, Analysis and Manufacturing: AIEDAM* **32**, 189 (2018).
10. Wagner, M., Chen, T. & Shea, K. Large Shape Transforming 4D Auxetic Structures. *3D Printing and Additive Manufacturing* **4**, 133 (2017).

### Conference contributions:

11. Chen, T. & Shea, K. *Design and Fabrication of Hierarchical Multi-Stable Structures through Multi-Material Additive Manufacturing* in *Proceedings of the ASME 2016 International Design Engineering Technical Conferences & Computers and Information in Engineering Conference* (Charlotte, NC, 2016), Vo2ATo3Ao32.

12. Chen, T., Mueller, J. & Shea, K. *Design and Fabrication of a Bistable Unit Actuator with Multi-Material Additive Manufacturing* in *Proceedings of the International Solid Freeform Fabrication Symposium 2016* (University of Texas, Austin, Texas, USA, 2016).
13. Chen, T. & Shea, K. *Computational Design-To-Fabrication Using Spatial Grammars : Automatically Generating Printable Car Wheel Design Variants* in *Proceedings of the 20th International Conference on Engineering Design (ICED 15)* (eds Weber, C., Husung, S., Cantamessa, M., Cascini, G., Marjanovic, D. & Venkataraman, S.) (Design Society, Glasgow, 2015), 1.
14. Chen, T., Stöckli, F. & Shea, K. *Design for Mass Customization Using Additive Manufacture : Case-Study of a Balloon-Powered Car* in *Proceedings of the 20th International Conference on Engineering Design (ICED 15)* (eds Weber, C., Husung, S., Cascini, G., Cantamessa, M., Marjanovic, D. & Rotini, F.) 4 (Design Society, Glasgow, 2015), 245.
15. Chen, T., Egan, P., Stöckli, F. & Shea, K. *Studying the Impact of Incorporating an Additive Manufacturing Based Design Exercise in a Large, First Year Technical Drawing and CAD Course* in *17th International Conference on Advanced Vehicle Technologies; 12th International Conference on Design Education; 8th Frontiers in Biomedical Devices* 3 (2015), V003To4A015.
16. Zimmermann, L., Chen, T. & Shea, K. *Generative Shape Design Using 3D Spatial Grammars, Simulation and Optimization* in *Design Computing and Cognition* (2016), 279.